La gloria di colui che tutto move
per l'universo penetra, e risplende
in una parte piú e meno altrove.

[Dante, Paradiso I]

Contents

Abstract

This thesis addresses the theoretical study of non–thermal phenomena in clusters of galaxies, particularly concerning the acceleration of relativistic particles and radio properties of cooling flow clusters in connection with the physical properties of the thermal intracluster medium (ICM).

We argue (**Chapter 4**) that the presence of diffuse synchrotron emission forming the so–called *radio mini–halos*, observed in some cooling flow clusters, can be explained by reacceleration of relativistic electrons, with the energetics necessary for the reacceleration supplied by the cooling flows themselves. In particular, the reacceleration due to MHD turbulence via Fermi–like processes has the correct radial dependence on the parameters to naturally balance the radiative losses in the cooling flow region. Since the presence of an observable radio mini–halo in a cooling flow region critically depends on the combination of several physical parameters, we suggest that the rarity of radio mini–halos is due to the fact that the physical conditions of the ICM are intermediate between those which lead to the formation of extended radio halos, hosted by clusters without cooling flows, and those holding in cooling flow clusters without radio halos. The basic results of our model remain unchanged even if the cooling flow is stopped somewhere in the innermost region of the cluster.

We present (**Chapter 5**) the application of this model to two observed mini–halos, the Perseus cluster and Abell 2626, showing that the main properties of the radio mini–halo (brightness profile, total radio spectrum and radial spectral steepening) can be accounted for by the model. In agreement with the basic idea of the model, i.e. that the necessary energy to power radio mini–halos is extracted by cooling flows, we find that the necessary energy rate for the reacceleration of the

electron population is a factor ~ 0.4 % of the total power supplied by the cooling flow.

We also discuss (**Chapter 6**) the observational properties of the population of radio mini–halos in relation with those of host clusters, and present a trend where the radio power of mini–halos increases with the cooling flow power. This trend is expected in the framework of the model and gives further support to the model itself. Possible effects of new *Chandra* and *XMM–Newton* estimates of $\dot{M}$ on this trend are considered: we conclude that even if earlier derived cooling rates were overestimated, cooling flow powers are still well above the radio powers of mini–halos.

In **Chapter 1** we discuss the observational properties of non–thermal and thermal phenomena in clusters of galaxies, while in **Chapter 3** we review the topic of cooling flows. In **Chapter 2** we critically discuss the acceleration mechanisms of electrons and the modeling of non–thermal phenomena in clusters.

$H_0 = 50$ km s^{-1} Mpc^{-1} and q_0=0.5 are assumed throughout and, where not specified, all the formulae are in cgs system.

Chapter 1

Clusters of Galaxies: Main Properties of the ICM

1.1 Introduction

The galaxy distribution on the sky is not homogeneus: in fact, galaxies tend to clump together in *clusters*, which represent the largest bound structures in the Universe. Clusters of galaxies are still largely defined by their optical properties. Historically, a great advance in the systematic study of the properties of clusters occurred when Abell compiled an extensive, statistically complete catalog of rich clusters of galaxies in the northern areas of the sky, with declination greater than $-27°$ (Abell 1958); this catalog is by far the most widely used. Like some of the other cluster catalogs that are available (e.g. Zwicky et al. 1968; Gunn, Hoessel & Oke 1986), the Abell catalog was constructed entirely by visual inspection of photographic plates: clusters are identified as enhancements in the surface number density of galaxies.

Clusters of galaxies typically contain hundreds of galaxies, spread over a region extended for some Mpc. The population of galaxies in clusters is substantially different from that in the field (e.g. Dressler 1980): with respect to the field distribution, clusters are richer in ellipticals and spheroidals, and poorer in spirals. Rich clusters are often dominated by a single, central cD galaxy. A number of different cluster properties have been used to construct morphological classification systems for clusters. These different systems are empirically found to be highly correlated, and clusters can be represented as a sequence running from *regular* to *irregular* clusters. Regular clusters are highly symmetric in shape, and have a core with a high concentration of galaxies towards the center. Subclustering is weak or absent in regular cluster. In contrast, irregular cluster have little simmetry or central concentration, and often show significat subclustering. This suggests that regular clusters are dynamically more evolved and relaxed than irregular clusters.

The first X–ray observations of clusters obtained by the *UHURU* satellite (e.g. Giacconi et al. 1972) and then by the *Einstein* satellite cleary indicated that the space between the galaxies is filled with hot X–ray emitting gas (e.g. Jones & Forman 1984). The simplest model for this intra–cluster medium (ICM) is that of an ideal gas evolving in the gravitational potential of the dark matter, which contributes to most of the total mass of clusters. Historically, measurements of the masses of clusters were made from optical studies of their galaxy populations, which give the virial masses. In particular, the discovery that cluster masses greatly exceed those which would be expected by summing the masses of all the cluster galaxies was first made by Zwicky (1933) by applying this method. Currently, the two most promising techniques for obtaining accurate measurements of cluster masses are via X–ray observations (by deprojection of X–ray surface brightness, e.g. Fabian et al. 1981) and observations of gravitational lensing by clusters (e.g. Fort & Mellier 1994). Typically, clusters of galaxies have total masses which exceed 5×10^{14} $M_{\odot}$, contributed for $\sim 75\%$ by dark matter, $\sim 20\%$ by ICM and $\sim 5\%$ by galaxies (e.g. Allen 1998, Arnaud 2001).

Besides the thermal plasma, there is a compelling evidence for relativistic particles and magnetic fields diffused in the ICM, whose existence in some clusters is directly demonstrated by the presence of diffuse extended radio emission (synchrotron radiation).

In this Chapter we will focus on the ICM, the main baryonic cluster component, devoting particular attention to its thermal (Sect. 1.2) and non–thermal (Sect. 1.3) properties.

1.2 Thermal ICM

Clusters of galaxies are luminous X–ray sources, with typical luminosities ranging from a few$\times 10^{43}$ - 10^{46} erg s^{-1}. As first suggested by Felten et al. (1966), the X–rays from clusters are primarily thermal bremsstrahlung emission from the diffuse ICM, at a temperature of $T \sim 10^8$ K [1] and an atomic density of $n \sim 10^{-3}$ cm^{-3}, that fills the deep gravitational potentials. Among several emission mechanisms that were proposed, that of thermal emission from hot gas is most consistent with the X–ray spectra of clusters: indeed, the detection of strong X–ray line emission from clusters (as for example the strong 7 keV Fe line) can not be reconciled with any non–thermal model for the origin of the X–ray emission (e.g. Bahcall & Sarazin 1977). This emission occurs naturally in the ICM model if the abundances of heavy elements are roughly solar, while non–thermal processes would not directly produce any significant line emission.

After a brief mention of the basic properties of a hot diffuse plasma such as the ICM (Sect. 1.2.1), in this Section we will discuss the physical processes responsible for the X–ray emission from the ICM (Sect. 1.2.2) and summarize the hydrostatic models for ICM distribution (Sect. 1.2.3).

1.2.1 Physical Properties of Hot Diffuse Plasma

Several simple assumptions are generally made in the study of the ionization state and X–ray line and continuum emission from a low density, hot plasma (e.g. Sarazin 1988).

1. The time scale for elastic Coulomb collisions between particles in the plasma is much shorter than the age or cooling time of the plasma, therefore the free particles are assumed to have a Maxwell–Boltzmann distribution at the temperatute T. This follows from considerations on the mean free paths of particles in a plasma without a magnetic field. The mean free path $\lambda_{\rm e}$ for an electron to suffer an energy exchange with another electron via Coulomb collisions is given by (Spitzer 1956):

$$\lambda_{\rm e} = \frac{3^{3/2}(kT)^2}{4\pi^{1/2} n_{\rm e} {\rm e}^4 \ln\Delta} \tag{1.1}$$

[1] T in degrees can also be written in terms of the corresponding energy kT, commonly used to characterize the X–ray spectrum of the ICM: $T(\mathrm{K}) \sim 1.16 \times 10^7 T(\mathrm{keV})$

where $T_{\rm e}$ is the electron temperature, $n_{\rm e}$ is the electron number density and Δ is the ratio of largest to smallest impact parameters for the collisions ($\ln\Delta \approx 38$). Eq. 1.1 assumes that the electrons have a Maxwellian velocity distribution at the electron temperature $T_{\rm e}$. However, it can be demonstrated that if a homogeneous plasma is created in a state in which the particle distribution is non–Maxwellian, elastic collisions will cause it to relax to a Maxwellian distribution on a time scale determined by the mean free paths (Spitzer 1956, 1978). Electrons will achieve this equilibrium on a time scale given roughly by $t_{\rm eq}(e,e) \equiv \lambda_{\rm e}/\langle v_{\rm e}\rangle_{\rm rms}$, where $\langle v_{\rm e}\rangle_{\rm rms}$ is the rms electron velocity $= (3kT_{\rm e}/m_{\rm e})^{1/2}$:

$$t_{\rm eq}(e,e) \approx 3.3\times10^5\ {\rm yr}\left(\frac{T_{\rm e}}{10^8\ {\rm K}}\right)^{3/2}\left(\frac{n_{\rm e}}{10^{-3}\ {\rm cm}^{-3}}\right)^{-1} \tag{1.2}$$

The time scale for Coulomb collisions between protons to bring them into kinetic equilibrium is about $t_{\rm eq}(p,p) \approx (m_{\rm p}/m_{\rm e})^{1/2} t_{\rm eq}(e,e)$, roughly 43 times longer than that for electrons. After this time, the electrons and ions (generally assumed to be protons) would each have Maxwellian distribution, but generally at different temperatures, respectively $T_{\rm e}$ and $T_{\rm i}$. The time scale for the electrons and ions to reach equipartition $T_{\rm e} = T_{\rm i}$ is $t_{\rm eq}(p,e) \approx (m_{\rm p}/m_{\rm e}) t_{\rm eq}(e,e)$, and for typical values of the ICM temperature and density is $t_{\rm eq}(p,e) \lesssim 6\times10^8$ yr. Since this is shorter than the age of the clusters or their cooling time, the intra–cluster plasma can generally be characterized by a single kinetic temperature $T = T_{\rm e} = T_{\rm i}$, which determines the rates of all excitation and ionization processes. It is worth noticing that the mean free paths, i.e.:

$$\lambda_{\rm e} = \lambda_{\rm i} \approx 23\ {\rm kpc}\left(\frac{T_{\rm e}}{10^8\ {\rm K}}\right)^{2}\left(\frac{n_{\rm e}}{10^{-3}\ {\rm cm}^{-3}}\right)^{-1} \tag{1.3}$$

are generally much shorter than the length scales of interest in clusters (≈ 1 Mpc), and therefore the ICM can be treated as a collisional fluid, satisfying the hydrodynamic equations.

2. At these low densities, collisional excitation and de–excitation processes are much slower than radiative decays, therefore any ionization or excitation process is assumed to be initiated from the ground state of an ion. Three (or more) body collisional processes are ignored because of the low density.

3. Stimulated radiative transitions are not important, since the radiation field in a cluster is sufficiently dilute.

4. At these low densities, the gas is optically thin and the transport of the radiation field can therefore be ignored.

Under these conditions, ionization and emission result primarily from collisions of ions with electrons, and collisions with other ions can be ignored. The time scales for ionization and recombination are generally considerably shorter than the age of the cluster or any relevant hydrodynamic time scale, therefore the plasma is assumed to be in ionization equilibrium. The equilibrium ionization state of a diffuse plasma depends only on the electron temperature: since in nearly all astrophysical plasmas most of the electrons originate in hydrogen and helium atoms, and these are fully ionized under the conditions considered here, the ICM is generally treated as a fully ionized plasma.

Relations in a Fully Ionized Plasma

By indicating with $\mathcal{X}, \mathcal{Y}, \mathcal{Z}$ the mass fraction of hydrogen, helium, and heavier elements, respectively, the corresponding atom number densities can be written in the form:

$$n_{\rm H} = n_{\rm p} \equiv \rho \frac{\mathcal{X}}{m_{\rm p}} \tag{1.4}$$

$$n_{\rm He} = \frac{n_{\rm p}}{4} \frac{\mathcal{Y}}{\mathcal{X}} \tag{1.5}$$

$$n_{\rm z} = \frac{n_{\rm p}}{2Z} \frac{\mathcal{Z}}{\mathcal{X}} \tag{1.6}$$

where ρ is the gas density, $m_{\rm p}$ the proton mass and Z the atomic number. Assuming that the gas pressure $P = n_{\rm T} kT$ is contributed only by electrons and protons

($n_{\rm T} = n_{\rm e} + n_{\rm p}$), it is possible to derive the electron density $n_{\rm e}$ in terms of the proton density $n_{\rm p}$: from $n_{\rm T} = 2n_{\rm H} + 2n_{\rm He} + Zn_{\rm z}$ and Eqs. 1.4 - 1.6 one obtains:

$$n_{\rm T} = \left(2 + \frac{1}{2}\frac{\mathcal{Y}}{\mathcal{X}} + \frac{1}{2}\frac{\mathcal{Z}}{\mathcal{X}}\right) n_{\rm p} \tag{1.7}$$

which for solar abundances ($\mathcal{X} = 0.71$, $\mathcal{Y} = 0.265$, $\mathcal{Z} = 0.025$) leads to $n_{\rm e} \sim 1.2n_{\rm p}$. It is also possible to calculate the mean molecular weight in *amu*, μ, such that the total number density of particles (electrons, protons and ions) is $\overline{n} = \rho/\mu m_{\rm p}$: from $\overline{n} = 2n_{\rm H} + 3n_{\rm He} + (Z+1)n_{\rm z}$ and Eqs. 1.4 - 1.6, in the approximation $Z \gg 1$, one obtains:

$$\mu = \left(2\mathcal{X} + \frac{3}{4}\mathcal{Y} + \frac{1}{2}\mathcal{Z}\right)^{-1} \tag{1.8}$$

which for solar abundances leads to $\mu \sim 0.6$.

1.2.2 X–ray Emission from the ICM

The X–ray continuum emission from a hot diffuse plasma, such as the ICM, is due primarily to two processes: thermal bremsstrahlung (free–free emission) and recombination (free–bound) emission. Processes that contribute to X–ray line emission (bound–bound radiation) from a diffuse plasma include collisional excitation of valence or inner shell electrons, radiative and dielectric recombination, inner shell collisional ionization and radiative cascades following any of these processes.

Thermal Bremsstrahlung

At the high temperatures typical of clusters (in particular at $T \gtrsim 2.5$ keV), thermal bremsstrahlung is the predominant X–ray emission process. The bremsstrahlung emissivity at a frequency ν (defined as the emitted energy per unit time, frequency and volume) of a plasma with temperatute T, electron density n_e and ion density n_i is given by (e.g. Rybicki & Lightman 1979):

$$J_{\rm br}(\nu,T) = 6.8 \times 10^{-38} Z^2 n_{\rm e} n_{\rm i} T^{-1/2} {\rm e}^{-h\nu/kT} \overline{g}(\nu,T) \tag{1.9}$$

where the Gaunt factor $\overline{g}(T)$, which corrects for quantum mechanical effects and for the effect of distant collisions, is a slowly varying function of the parameters (Karzas & Latter 1961; Kellogg, Baldwin & Koch 1975). If the ICM is mainly at a single temperature, then Eq. 1.9 indicates that the X–ray spectrum should be close to an exponential of the frequency, as is generally observed.

The total power per unit volume emitted by thermal bremsstrahlung is obtained by integrating Eq. 1.9 over frequency, obtaining:

$$J_{br}(T) = 1.4 \times 10^{-27} n_{\rm e} n_{\rm i} T^{1/2} Z^2 \overline{g}(T) \tag{1.10}$$

where $\overline{g}(T)$ is a frequency average of $\overline{g}(\nu,T)$ and is in the range 1.1 to 1.5 (choosing a value of 1.2 will give an accuracy in the estimate of $J_{br}(T)$ to within about 20%, Rybicki & Lightman 1979). For solar abundances, the emission is primarily from hydrogen and helium.

Resulting X–ray Spectra

Compilations of the different emissivities for X–ray lines and continua can be found in the literature (e.g. Raymond & Smith 1977 and Mewe & Gronenschild 1981). The emissivities at the frequency ν increase in proportion to the ion and electron densities, and depend otherwise on the temperature only, so that:

$$J_{\rm X}(\nu,T) = \sum_{K,i} \Lambda_\nu(K^i,T) n(K^i) n_{\rm e} \tag{1.11}$$

where Λ_ν is the emission per ion at unit electron density at the frequency ν. If $n(K)$ is the total density of the element K, then in equilibrium the ionization fractions $f(K^i) \equiv n(K^i)/n(K)$ depend only on the temperature, and Eq. 1.11 becomes:

$$J_{\mathrm{X}}(\nu, T) = n_{\mathrm{p}} n_{\mathrm{e}} \sum_{K,i} \frac{n(K)}{n(H)} [f(K^i, T) \Lambda_\nu(K^i, T)] \tag{1.12}$$

Then the shape of the spectrum depends only on the abundances of the elements, $n(K)/n(H)$, and on the distribution of temperatures.

Detailed calculations of the X–ray spectra predicted by different models of the ICM have been given by Sarazin & Bahcall (1977) and Bahcall and Sarazin (1977, 1978). In these models most of the X–ray emission is thermal bremsstrahlung continuum, and the strongest lines (highest equivalent width) are in the 7 keV iron line complex.

The frequency–integrated emissivity at a temperature T can be written as:

$$J_{\mathrm{X}}(T) = \Lambda(T) n_{\mathrm{e}} n_{\mathrm{p}} \quad \mathrm{erg\ s^{-1}\ cm^{-3}} \tag{1.13}$$

where $\Lambda(T)$ is the *cooling function*, which depends upon the mechanism of the emission and can be represented as:

$$\Lambda(T) = l\, T^{\alpha} \tag{1.14}$$

where $-0.6 \lesssim \alpha \lesssim 0.55$; for thermal bremsstrahlung it is $l \sim 2.5 \times 10^{-27}$ and $\alpha = 1/2$ (McKee & Cowie 1977).

The projection on the sky of the plasma emissivity gives the X–ray surface brightness: in order to constrain the physical parameters of the ICM, the observed surface brightness can be either geometrically deprojected or, more simply, fitted with a model obtained from an assumed distribution of the gas density.

1.2.3 Hydrostatic Models for ICM Distribution

From the expression for the sound speed $c_{\mathrm{s}}{}^2 = \gamma kT/\mu m_{\mathrm{p}}$, where $\gamma = 5/3$ for a monoatomic gas, one finds that the time required for a sound wave in the ICM to cross a cluster is given by:

$$t_{\rm s} \approx 6.6 \times 10^8 \left(\frac{T}{10^8\ {\rm K}}\right)^{-\frac{1}{2}} \left(\frac{D}{1\ {\rm Mpc}}\right) \qquad {\rm yr} \tag{1.15}$$

where D is the cluster diameter. Since this time is short compared to the likely age of a cluster ($\sim 10^{10}$ yr), the gas is generally thought to be in hydrostatic equilibrium in the gravitational potential of the cluster:

$$\nabla P = -\rho \nabla \phi \tag{1.16}$$

where $P = \rho kT/\mu m_{\rm p}$ is the gas pressure, ρ is the gas density and ϕ is the gravitational potential of the cluster. Under the assumptions that the ICM is locally homogeneous and the cluster is spherically symmetric, Eq. 1.16 reduces to:

$$\frac{1}{\rho}\frac{dP}{dr} = -\frac{d\phi}{dr} = -\frac{GM(r)}{r^2} \tag{1.17}$$

where r is the radius from the cluster center and $M(r)$ is the total cluster mass within r. If the self gravity, that is the contribution of the ICM to the gravitational potential, is ignored, then the distribution of the ICM is determined by the cluster potential $\phi(r)$ and the temperature distribution of the gas $T(r)$, and Eq. 1.17 is a linear equation for the logarithm of the gas density: once the central density is specified, one can determine the general density profile. In most models, the cluster potential is assumed to be that derived from the spatial distribution of galaxies: indeed, given the hydrostatic equilibrium within the cluster, the gravitational potential supports both the gas and the galaxies distribution.

Spatial Distribution of Galaxies

The most regular clusters show a smooth galaxy distribution which concentrates towards the central region (*core*). In general, models for the galaxy distribution in these clusters depend on some parameters, which can be taken to be the central projected density of galaxies per unit area on the sky Σ_0, and two distance scales,

r_{core} and R_h. The core radius, r_{core}, is a measure of the size of the central core, and is usually defined such that the projected galaxy density at a distance $r_{\rm core}$ from the cluster center is one half of the central density Σ_0. The halo radius $R_{\rm h}$ measures the maximum radial extent of the cluster. For spherically symmetric galaxy distributions, one can write the spatial volume density of galaxies at a distance r from the cluster center in the form:

$$n_{\rm gal}(r) = n_{\rm gal,0}\ {\rm f}\left(\frac{r}{r_{\rm core}}, \frac{r}{R_{\rm h}}\right) \tag{1.18}$$

where $n_{\rm gal,0}$ is the central number density and f an adimensional function. The projected surface density at a projected distance b from the center is:

$$\Sigma(b) = 2\int_b^{R_h} \frac{n_{\rm gal}(r)\, r\, dr}{\sqrt{r^2 - b^2}}, \tag{1.19}$$

and may be written in the form:

$$\Sigma(b) = \Sigma_0\ {\rm F}\left(\frac{b}{r_{\rm core}}, \frac{b}{R_{\rm h}}\right) \tag{1.20}$$

where F is an adimensional function related to f. A number of different models have been proposed to fit the distribution of galaxies and isothermal models are among the simplest. Isothermal models assume:

- a Gaussian radial velocity distribution for galaxies:

$$p(v_{\rm r})dv_{\rm r} = \frac{1}{\sigma_r\sqrt{2\pi}}\, {\rm e}^{-\frac{(v_{\rm r}-\langle v_{\rm r}\rangle)^2}{2{\sigma_{\rm r}}^2}}\, dv_{\rm r} \tag{1.21}$$

  where $v_{\rm r}$ is the component of the galaxy velocity along the line–of–sight, $p(v_{\rm r})dv_{\rm r}$ is the probability that an individual cluster galaxy has a radial velocity in the range $v_{\rm r}$ to $v_{\rm r} + dv_{\rm r}$ and $\sigma_{\rm r}$ is the dispersion of velocities along the line of sight about the mean:

$$\sigma_{\rm r} = \left\langle (v_{\rm r} - \langle v_{\rm r} \rangle)^2 \right\rangle_{\rm OSS}^{\frac{1}{2}}; \tag{1.22}$$

- that the velocity distribution is isotropic and independent of position;
- that the galaxy distribution is stationary;
- that galaxy positions are not correlated;
- that the galaxies can be considered to be a collisionless gas, as derived from the consideration that the time–scale for two–body gravitational interactions in a cluster is much longer than the time for a galaxy to cross the cluster.

Under these assumptions, the galaxy spatial distribution is:

$$n_{\rm gal}(r) = n_{\rm gal,0}\, e^{-\frac{\phi(r)}{\sigma_r{}^2}} \tag{1.23}$$

If the mass in the cluster is distributed in the same way as the galaxies, then Poisson's equation for the gravitational potential $\nabla^2 \phi = 4\pi G \rho$ becomes:

$$\frac{1}{r^2}\frac{d}{dr}\left(r^2 \frac{d\phi}{dr}\right) = 4\pi\, G\, n_{\rm gal,0}\, m\, e^{-\frac{\phi}{\sigma_{\rm r}{}^2}} \tag{1.24}$$

where m is the mass per galaxy, assumed for simplicity to be the same for all the galaxies in the cluster (Chandrasekhar 1942). Introducing the variables $\psi \equiv \phi/\sigma_{\rm r}{}^2$ and $\xi \equiv r/\chi$, where $\chi \equiv \sigma_{\rm r}\,(4\pi\, G\, n_{\rm gal,0}\, m)^{-1/2}$, Eq. 1.24 can be written in the form:

$$\frac{1}{\xi^2}\frac{d}{d\xi}\left(\xi^2 \frac{d\psi}{d\xi}\right) = e^{-\psi} \tag{1.25}$$

subject to the boundary conditions (assuming that the density is regular at the cluster center) $\psi = 0, d\psi/d\xi = 0$ at $\xi = 0$.

Eq. 1.25 is seen to be identical with the equation of hydrostatic equilibrium of an isothermal gas sphere (Chandrasekhar 1939), and its solution is exactly the function needed to model the galaxy distribution (Eq. 1.23): in terms of this function ψ, and hence of the gravitational potential $\phi = \psi {\sigma_{\rm r}}^2$ needed to also model the ICM distribution, the structure of the configuration is uniquely determined. The solution $\psi(\xi)$ of Eq. 1.25 can not be represented by a simple analytic function, but must be calculated by numerical approximations (e.g. Zwicky 1957; Flannery & Krook 1978). Unfortunately, it is not possible to use the isothermal approximation for a complete description of a cluster of galaxies, because the distribution 1.23 predicts an infinite mass for the cluster when integrated to $r \to \infty$. Indeed, it is known that every solution of the isothermal equation 1.25 tends asymptotically to the special solution $e^{-\psi} = 2/\xi^2$, so that $n_{\rm gal}(\xi) \to 2n_{\rm gal,0}/\xi^2$ and therefore the total number of galaxies and total mass diverge in proportion to r. Consequently, the isothermal sphere is seen to be inadequate for describing the outer regions of a finite cluster.

King Approximation to the Isothermal Sphere Model for Galaxy Distribution

A number of methods to truncate the isothermal distribution have been used (e.g. Zwicky 1957; King 1966). King (1962) showed that the following analytic functions are a reasonable approximation to the inner portions of an isothermal function:

$$n_{\rm gal}(r) = n_{\rm gal,0} \left[1 + \left(\frac{r}{r_{\rm core}}\right)^2\right]^{-\frac{3}{2}} \tag{1.26}$$

$$\Sigma(b) = \Sigma_0 \left[1 + \left(\frac{b}{r_{\rm core}}\right)^2\right]^{-1} \tag{1.27}$$

where $\Sigma_0 = 2\, n_{\rm gal,0}\, r_{\rm core}$.

At large radii $r \gg r_{\rm core}$, $n_{\rm gal}(r) \approx n_{\rm gal,0}\, (r_{\rm core}/r)^3$, thus the cluster mass and galaxy number diverge as $\ln(r/r_{\rm core})$. Although this is a slower divergence than the unbounded isothermal model, King's analytic model also must be truncated at some finite radius $R_{\rm h}$.

Isothermal Sphere Model for ICM Distribution

In most models for ICM distribution, the cluster potential is assumed to be that of a self–gravitating isothermal sphere, as derived from the galaxy distribution. For convenience, the analytic King approximation to the isothermal sphere is often assumed (Eq. 1.26), so that the cluster total density, mass and potential are given by:

$$\rho(r) = \rho_0 \left[1 + \left(\frac{r}{r_{\rm core}}\right)^2\right]^{-\frac{3}{2}} \tag{1.28}$$

$$M(r) = 4\pi\rho_0 r_{\rm core}^3 \left\{ \ln\left[\left(\frac{r}{r_{\rm core}}\right) + \left(1 + \left(\frac{r}{r_{\rm core}}\right)^2\right)^{\frac{1}{2}}\right] - \frac{\left(\frac{r}{r_{\rm core}}\right)}{\left(1 + \left(\frac{r}{r_{\rm core}}\right)^2\right)^{\frac{1}{2}}} \right\} \tag{1.29}$$

$$\phi(r) = -4\pi G\rho_0 r_{\rm core}^2 \frac{\ln\left[\left(\frac{r}{r_{\rm core}}\right) + \left(1 + \left(\frac{r}{r_{\rm core}}\right)^2\right)^{\frac{1}{2}}\right]}{\left(\frac{r}{r_{\rm core}}\right)} \tag{1.30}$$

The central density $\rho_{\rm g,0}$ and core radius $r_{\rm core}$ are related to the line–of–sight velocity dispersion $\sigma_{\rm r}$ of an isothermal cluster by (e.g. Binney & Tremaine 1987):

$$\sigma_{\rm r}{}^2 = \frac{4\pi\, G\, \rho_0\, r_{\rm core}^2}{9} \tag{1.31}$$

thus the central value of the cluster gravitational potential is $\phi_0 = -9\sigma_{\rm r}{}^2$.

It is worth noticing that $\rho(r)$ in Eq. 1.28 is obtained by integrating Eq. 1.17 for hydrostatic equilibrium with the gravitational potential derived by the distribution of galaxies, assuming that both the gas and the galaxies are distributed in the same way being in equilibrium in the same potential. However, galaxies have been treated as a collisionless isothermal gas, while the ICM is a collisionally dominated fluid. We have thus a mixture of two different gases separately in hydrostatic equilibrium in the same gravitational potential and a better investigation of this problem is needed.

The β–Model for ICM Distribution

More consistent isothermal models can be derived by taking into account the hydrostatic equilibrium equation for both the galaxies and the ICM (Cavaliere & Fusco-Femiano 1976). With the aim to explain the observed X–ray emission from clusters of galaxies, Cavaliere & Fusco-Femiano (1976) studied the bremsstrahlung emission by a static hot plasma in the potential well set up by a cluster. In their model, a relevant parameter governing the motion of the gas through the cluster potential and the clumping towards the cluster center is the ratio of specific kinetic energies of galaxies and gas:

$$\beta = \frac{{\sigma_\mathrm{r}}^2}{kT/\mu m_\mathrm{p}} \tag{1.32}$$

In case the gravitational behaviours of the gas and galaxies were identical (as assumed in the isothermal sphere model), one would expect $\beta = 1$. However, since the galaxies can be considered as a collisionless system while the gas is a collisional fluid, these two components will be partially separated during the cluster formation. For example, the infalling gas will typically be stopped by the passage of a shock while the galaxies continue to fall inwards: this causes the gas to be less tightly bound than the galaxies, resulting in a decreasing β (Fabian, Nulsen & Canizares 1984). Therefore, one could expect $\beta \lesssim 1$, as observed (e.g. Jones & Forman 1984; Bahcall 1994).

As the gas potential energy per unit mass is measured by σ_r^2, the β parameter also represents the ratio of specific potential and kinetic energies of the gas: this means that not much plasma at temperatures larger than a few 10^8 K could remain clumped within a cluster with a typical velocity dispersion $\sigma_\mathrm{r} \approx 1000$ km sec^{-1}, while the ICM at $T \leq 10^8$ K must instead conform to the gravitational potential of the cluster.

Since both gas and galaxy distributions conform to the same gravitational potential, the former can be directly related to the latter and the space distribution of galaxies may be considered as a tracer of the depth and shape of the average potential well. Therefore, a direct relationship must exist between the galaxy counts

$n_{\rm gal}$ and the gas density ρ averaged over sizes larger than galactic. This goes into a relationship between the mass density in galaxies $\rho_{\rm gal}$ and the gas density ρ. This relationship may be derived by eliminating the gravitational term between the equation for the gas equilibrium (Eq. 1.17):

$$\frac{d\ln\rho}{dr} = -\frac{\mu m_{\rm p}}{kT}\frac{d\phi(r)}{dr} \tag{1.33}$$

and the equivalent equation for the galaxies in case the velocities are isotropic:

$$\frac{d\ln\rho_{\rm gal}}{dr} = -\frac{1}{{\sigma_{\rm r}}^2}\frac{d\phi(r)}{dr} \tag{1.34}$$

From the definition of the parameter β (Eq. 1.32), one obtains:

$$\rho \propto \rho_{\rm gal}^{\beta} \tag{1.35}$$

which, by assuming that the galaxy distribution is well described by King's approximation to the isothermal sphere (1.26), leads to the following expression for the ICM distribution (Cavaliere & Fusco-Femiano 1976):

$$\rho(r) = \rho_0\left[1+\left(\frac{r}{r_{\rm core}}\right)^2\right]^{-\frac{3}{2}\beta} \tag{1.36}$$

The surface brightness profile observed at a projected radius b, $I(b)$, is obtained by integrating along the line–of–sight the plasma emissivity $J_{\rm X}(r)$ (Eq. 1.13). Assuming Eq. 1.36 for the gas density, the functional form of the surface brightness profile is (Cavaliere & Fusco-Femiano 1976):

$$I(b) = I_0\left[1+\left(\frac{b}{r_{\rm core}}\right)^2\right]^{\frac{1}{2}-3\beta} \tag{1.37}$$

This self–consistent isothermal model, called the *β–model*, is widely used in the X–

ray astronomy to parametrise the gas density profile in clusters of galaxies by fitting their surface brightness profile.

Eq. 1.36 states that the gas density rises towards the cluster center. Since the bremsstrahlung and line emission depend on the square of the gas density (Eq. 1.13), in the central regions of clusters the loss of energy by X–ray emission represents an important process for the thermal particles in the ICM. In particular, if the gas density reaches high enough values, large amounts of gas cool and flow into the centers of clusters, forming the so–called *cooling flows*. Since the cooling flow represents an essential ingredient of this PhD work, the current status of our understanding of this phenomenon will be extensively presented and discussed from both a theoretical and observational point of view in Chapter 3.

1.3 Non–thermal Phenomena in the ICM

As seen in Sect. 1.2, the X–ray emission observed from clusters of galaxies is well explained as bremsstrahlung radiation from the very hot ($T \sim 10^8$ K), low density ($n_{\rm e} \sim 10^{-3}$ cm^{-3}) and highly ionized intra–cluster gas. Besides the thermal plasma, there is a compelling evidence for the existence of relativistic particles and magnetic fields diffused in the ICM. The existence of these non–thermal components in some clusters is directly demonstrated by the presence of diffuse extended radio sources, the so called *radio halos, relics* and *mini–halos* (see Feretti et al. 2000 for a recent review). It has been suggested that the relativistic particles might be as well responsible for hard X–ray (HXR) and extreme–ultraviolet (EUV) excesses detected in a few clusters (see e.g. Fusco-Femiano et al. 1999; Lieu et al. 1996a).

In this Section we will discuss the properties of non–thermal emission observed in clusters and the measurements of cluster magnetic fields. In particular, we will summarize the observational properties of diffuse radio sources together with the properties of their parent clusters (Sect. 1.3.1), while a discussion of the different models proposed for their origin will be presented in Chapter 2.

1.3.1 Diffuse Radio Emission

It is well known that the radio emission from clusters of galaxies generally originates from individual radio emitting galaxies. In addition, some clusters of galaxies exhibit synchrotron emission not directly associated with a particular galaxy but rather diffused into the ICM. These diffuse radio sources, which have been classified as radio halos, relics and mini-halos (Feretti & Giovannini 1996), are the most spectacular probe of the existence on non–thermal emission from the ICM.

Halos and Relics

According to definitions given in the literature, diffuse cluster–wide radio sources with no optical identification permeating the cluster centers are classified as radio halos. Sources with similar properties, located in peripheral regions, are referred to as relic sources. Large–scale *radio halos* show a generally regular shape, low surface brightness and a typical size of the order of $\sim$ 1 Mpc. They have a steep radio spectrum and show low or negligible polarized emission ($< 10\%$). *Relics* are similar to halos in the low surface brightness, large size and steep spectrum, but are generally elongated in shape and can be highly polarized (up to 30%).

The diffuse source Coma C in the Coma cluster, discovered 30 years ago (Willson 1970), is the prototypical and best studied example of a cluster radio halo (see Giovannini et al. 1993; Feretti & Giovannini 1998). It is located at the cluster center and shows a rather regular shape and a low surface brightness. The integrated radio spectrum in the frequency range $\leq$ 1.4 GHz is steep ($\alpha \sim 1.16$, $S_\nu \propto \nu^{-\alpha}$). The radio halo scale size is a monotonically decreasing function of the frequency (Deiss et al. 1997). This supports the suggestion by Giovannini et al. (1993) of a spectral steepening in the peripherical regions. Indeed, the spectral index distribution between 327 and 1.4 GHz shows a central plateau with $\alpha \sim 0.8$ and an outer region with a steeper spectrum, up to $\alpha \sim 1.8$. No polarization is detected down to a level of $\sim 10\%$ at 1.4 GHz.

The Coma cluster is characterized by the presence of another diffuse extended source, named 1253+275, located at $\sim$ 2.7 Mpc from the cluster center. This source, which has size, brightness and spectrum similar to those of Coma C, shows an elongated shape and 30% polarization level at 1.4 GHz and is considered the prototype of the relic source class.

Diffuse extended radio sources are difficult to detect because of their low surface brightness ($\sim \mu$Jy/arcsec^2 at 1.4 GHz) and large size: their detection is limited by the surface brightness sensitivity coupled with the high resolution needed to separate such sources from the embedded discrete sources. Because of their steep spectrum, they are better detected at lower frequencies. Despite the observational difficulties, several surveys were undertaken to detect radio halos and determine how common they are (e.g. Jaffe & Rudnick 1979; Cane et al. 1981; Hanish 1982). The general conclusion in the past was that such sources are very rare (e.g. Feretti & Giovannini 1996). However, Giovannini, Tordi & Feretti (1999) undertook a search for new halo and relic candidates using the NRAO VLA Sky Survey (NVSS, Condon et al. 1998) and found a list of 29 candidates for 18 of which the existence of this type of source was indicated for the first time. Other 18 candidates (7 new) were found by Kempner & Sarazin (2001) among all the Abell clusters present in the Westerbork Northern Sky Survey (WENSS, Rengelink et al. 1997) at 327 MHz. Thanks to the improved sensitivity of radio telescopes and the existence of deep surveys, the number of known diffuse sources has increased recently to about 40 objects (Giovannini & Feretti 2002). Remarkably, in some clusters both a radio halo and a relic have been detected. A search for new halo and relic sources is also in progress with the data from the Sidney University Molonglo Sky Survey (Hunstead et al. 1999).

Statistical Properties and Correlations with Cluster Properties

Unlike the thermal X–ray emission, the diffuse radio sources are not a common feature in clusters of galaxies. However, thanks to the increased number of known halos and relics, it has been possible to derive some statistical considerations on the properties of these sources and on their host clusters.

Typical radio powers for halo sources are of the order of 10^{24} - 10^{25} W Hz^{-1} at 1.4 GHz. Halos with a higher radio power are more extended, but no strong correlation is known between the radio size and the radio power (Giovannini & Feretti 2002).

Giovannini, Tordi & Feretti (1999) found that $\sim$5% of clusters in the complete X–

ray flux limited sample extracted from Ebeling et al. (1996) have a radio halo source and ∼6% a relic source. The detection rate increases with the X–ray luminosity, being ∼30 - 35% in clusters with X–ray luminosity > 10^{45} erg s^{-1}. Clusters hosting a radio halo have X–ray luminosities significantly higher than clusters without a diffuse source (Owen, Morrison & Vogues 1999; Giovannini, Feretti & Govoni 2000), implying that these clusters also have higher ICM temperatures ($kT \gtrsim 7$ keV) and larger masses (values larger than 1.5×10^{14} $M_\odot$ are found for the total gravitating mass within 0.5 Mpc, with gas fraction ranging from 10% to 20%).

In many cases, radio structures of halos show close similarities to the X–ray structures, suggesting a causal connection between the hot and relativistic plasma (Deiss et al. 1997; Feretti 1999; Liang et al. 2000). This similarity was quantitatively confirmed by Govoni et al. (2001a) by comparing the point–to–point surface brightness of the radio and X–ray emission in four clusters of galaxies (Coma, Abell 2255, Abell 2319, Abell 2744). This study leads to a correlation between the radio and the X–ray brightness in all the analyzed clusters: a higher X–ray brightness is associated with a higher radio brightness.

Colafrancesco (1999) and Liang et al. (2000) found a correlation between radio power and cluster temperature (see Fig. 1.1). This is consistent with the fact that the monochromatic radio power at 1.4 GHz of halos increases with the bolometric X–ray luminosity of the parent cluster (Feretti 2001) . Since in clusters the X–ray luminosity and the mass are correlated, as well as the temperature and the mass (Neumann & Arnaud 1999, 2001), it follows that the radio halo power correlates with the cluster mass. By analyzing 6 halo clusters, Govoni et al. (2001b) found $P_{1.4} \propto M^{2.2}$.

An important property noted in the first studies of clusters of galaxies containing a halo source is that these clusters are characterized by the presence of a merger process. This is indicated by the existence of substructures and distortions in the brightness distribution and by temperature gradients, which can be interpreted as the result of sub–clump interaction, and is also confirmed by statistical studies (Feretti 2001). At present, there is no knowledge of any radio halo source in a cluster where the presence of a merger was clearly excluded (Giovannini & Feretti

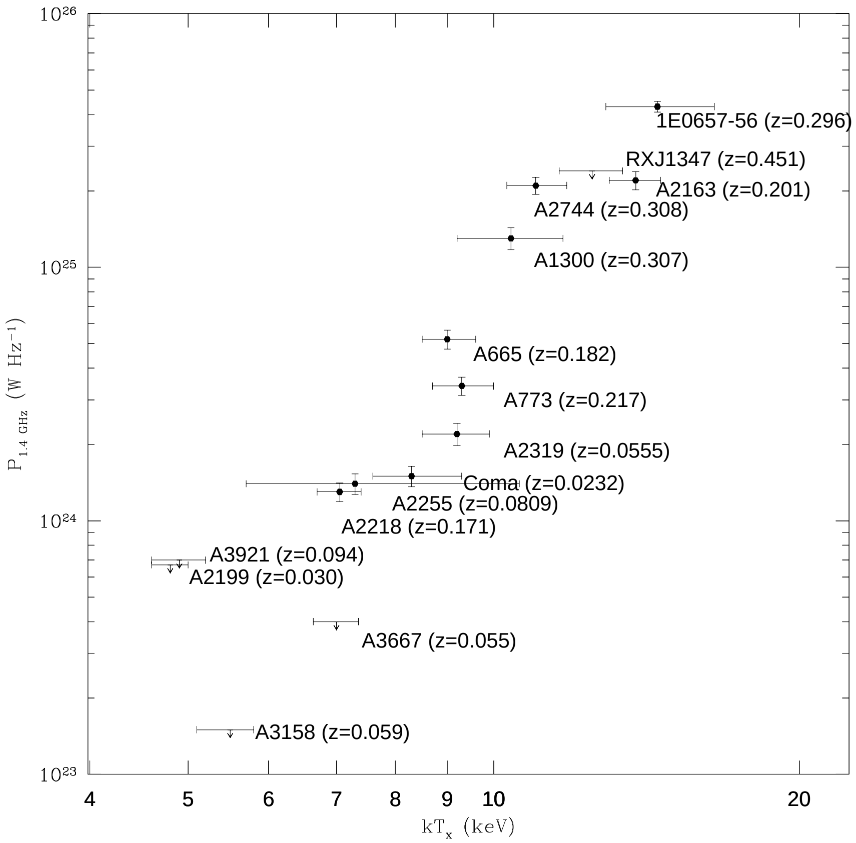

Figure 1.1: Radio power $P_{1.4}$ at 1.4 GHz (rest frame) versus the cluster X–ray temperature kT_x for all the confirmed radio halo sources. From Liang et al. (2000).

2002).

Another important point is the observed anti–correlation between the presence of a cooling flow (see Chapter 3) and that of an extended radio halo (e.g. Edge, Stewart & Fabian 1992; Giovannini, Tordi & Feretti 1999). Since a strong merger process is expected to disrupt a cooling flow (e.g. Sarazin 2002 and references therein), this is a further indication that the cluster containing an extended radio halo has undergone a recent merger. However, it has been argued (e.g. Giovannini & Feretti 2000; Liang et al. 2000; Feretti 2001) that merging can not be solely responsible for the formation of radio halos, because at least 50% of clusters show evidence for X–ray substructures (Jones & Forman 1999) whereas only $\sim 10\%$ possess radio halos.

By studying the dynamical states of clusters possessing radio halos, Buote (2001) found that the strongest radio halos appear only in those clusters which show the largest departures from a virialized state and concludes that radio halos form preferentially in massive ($L_{\rm X} \gtrsim 0.5 \times 10^{45}\,{\rm erg\,s^{-1}}$) clusters experiencing violent mergers that have seriously disrupted the cluster core.

Most of the peripherical relics have been found in clusters with properties similar to clusters with a halo source, and relic source correlate with cluster properties as the halo sources do (e.g. Buote 2001). However, a few relic sources have been found in the peripheral regions of cooling flow clusters (e.g. Abell 85).

Therefore, there seems to be convincing evidence that diffuse radio sources are preferentially associated with high X–ray luminosity clusters with mergers. It was proposed that recent cluster mergers may provide the energy to these extended sources, playing an important role in the reacceleration of the radio emitting relativistic particles and in the amplification of the magnetic field (e.g. Schlickeiser, Sievers & Thiemann 1987; Tribble 1993; Brunetti et al. 2001b). This and other different models proposed for the formation of diffuse radio sources will be discussed in Chapter 2.

Mini–Halos

A third class of diffuse cluster sources is represented by the *mini–halos*. Mini–halos are diffuse radio sources, extended on a small scale (up to ~ 500 kpc), surrounding a dominant radio galaxy at the cluster center. The prototype of this class is the diffuse emission detected in the Perseus cluster (Burns et al. 1992). In the literature, mini–halos are believed to be possibly related to a parent radio galaxy and thus considered different from halos and relics (Feretti & Giovannini 1996; Feretti 1999). However, it is worth noticing that these sources do not appear as extended lobes maintained by an Active Galactic Nucleus (AGN), as in classical radio galaxies, therefore their radio emission is indicative of the presence of diffuse relativistic particles and magnetic fields in the ICM.

Radio mini–halos, which are only observed in clusters with a cooling flow and are found to be not connected to ongoing cluster merger activity (Giovannini & Feretti 2002), remain a poorly understood phenomenon. These radio sources are the main topic of this PhD thesis, and the study of their nature and origin will be extensively illustrated in Chapters 4, 5 and 6.

1.3.2 Cluster Magnetic Fields

Magnetic fields in clusters of galaxies have been measured using a variety of techniques: overall, the data are consistent with cluster atmospheres substantially magnetized, with typical field strengths of the order of 1 μG. In some locations, such as the cores of cooling flow clusters, the magnetic fields reach levels of 10 - 40 μG and may be dynamically important (see Sect. 3.3). Even though in most clusters magnetic fields are not dynamically important, with magnetic pressures one to two orders of magnitude below thermal gas pressures, in all clusters the magnetic fields have a significant effect on energy transport in the ICM (Sarazin 1986; Tribble 1989) and significant implications for the lifetimes of relativistic particles in the ICM. Moreover, the magnetic suppression of thermal conductivity in the ICM, verified by the recent discovery of 'cold fronts' in clusters of galaxies (Markevitch et al. 2000; Vikhlinin, Markevitch & Murray 2001), may play an important role in understanding the common occurrence of cooling flows (see Chapter 3).

The origin and evolution of the magnetic field in the ICM is still an unresolved problem. Some current theories state that the magnetic field could be primordial (Olinto 1997), the result of a cluster dynamo effect (Ruzmaikin, Sokolov & Shukurov 1989), injected into the ICM by galactic winds (Kronberg, Lesch & Hopp 1999; Völk & Atoyan 1999), or by radio galaxies (Daly & Loeb 1990; Okoye & Onuora 1996), or amplified in shock waves of the large scale structure formation (Kang, Rachen, & Biermann 1997; Roettiger, Stone & Burns 1999; Dolag, Bartelmann & Lesch 1999). An additional possibility is that magnetic fields are amplified by turbulence excited by galactic motions (Jaffe 1980; Roland 1981; Ruzmaikin, Sokolov & Shukurov 1989; Sánchez-Salcedo, Brandenburg & Shukurov 1998). However, it has been shown that this kind of amplification is insufficient to create magnetic fields of the appropriate strength (De Young 1992; Goldsmith & Rephaeli 1993).

In this Section the main methods used for measuring cluster magnetic fields will be summarized. They consist on the analysis of:

- Synchrotron relic and halo sources within clusters;
- Faraday rotation measures of sources both embedded and behind the clusters;
- Hard X–ray emission in clusters containing radio relics and halos.

Synchrotron Radiation

As discussed in Sect. 1.3.1, a number of clusters of galaxies are known to contain large–scale diffuse radio sources which have no obvious connection with individual galaxies in the cluster (radio halos and relics). The observed synchrotron radiation (see e.g. Ginzburg & Syrovatskii 1965 and Pacholczyk 1970 for a treatment of the theory of synchrotron radiation) directly demonstrates the presence of cluster magnetic fields in the ICM.

Magnetic fields in cluster radio halos can be derived assuming a minimum energy configuration for the summed energy in relativistic particles and magnetic fields (Burbidge 1959), corresponding roughly to energy equipartition between fields and particles. The equations for deriving minimum energy fields from radio observations are given in Miley (1980). It is worth noticing that these calculations typically assume $k = 1$, $\eta = 1$, $\nu_{\rm low} = 10$ MHz, and $\nu_{\rm high} = 10$ GHz, where k is the ratio of energy densities in relativistic protons to that in electrons, η is the volume filling factor, $\nu_{\rm low}$ is the low frequency cut–off for the integral, and $\nu_{\rm high}$ is the high frequency cut–off. However, all of these parameters are poorly constrained, thus the derived equipartition magnetic fields are very uncertain and should be considered only as reference values. Estimates for minimum energy magnetic field strengths in cluster halos range from 0.1 to 1 μG (Feretti 1999). One of the best studied halos is that in Coma, for which Giovannini et al. (1993) report a minimum energy magnetic field of 0.4 μG.

Faraday Rotation

The presence of a magnetic field in an ionized plasma sets a preferential direction for the gyration of electrons, leading to a difference in the index of refraction for left versus right circularly polarized radiation. Linearly polarized light propagating through a magnetized plasma experiences a phase shift of the left versus right circularly polarized components of the wavefront, leading to a rotation of the plane of polarization, $\Delta\chi = \mathrm{RM}\cdot\lambda^2$, where $\Delta\chi$ is the change in the position angle of polarization, λ is the wavelength of the radiation, and RM is the Faraday rotation measure. The RM is related to the electron density, n_e, and the magnetic field, $\mathbf{B}$, as:

$$\mathrm{RM} = 812 \int_0^L n_\mathrm{e} \mathbf{B} \times d\mathbf{l} \;\; \mathrm{rad\ m}^{-2} \,, \tag{1.38}$$

where $\mathbf{B}$ is measured in μG, n_e in cm^{-3} and L is the depth of the screen in kpc. Synchrotron radiation from cosmic radio sources is well known to be linearly polarized, with fractional polarizations up to 70% in some cases (Pacholczyk 1970). Rotation measures can be derived from multifrequency polarimetric observations of these sources by measuring the position angle of the polarized radiation as a function of frequency. The RM values can then be combined with measurements of n_e to estimate the magnetic fields. Due to the vector product in Eq. 1.38, only the magnetic field component along the line–of–sight, $B_{||}$, is measured, so the results depend on the assumed magnetic field topology. A common assumption is $B = \sqrt{3}B_{||}$.

Dreher, Carilli & Perley (1987) first discovered that the large RMs observed in Cygnus A must arise in an external screen of magnetized, ionized plasma. They considered a number of options for the Faraday screen towards this source and concluded that the most likely site was the X–ray emitting ICM enveloping the radio source.

Since then, RM studies of cluster center radio sources have become a standard tool for measuring cluster fields. RM studies of radio galaxies in clusters can be divided into studies of cooling flow and non cooling flow clusters. Strong magnetic fields ($\simeq$ 5 - 30 μG) have been found in cooling flow clusters (see Sect. 3.3) where extremely large Faraday rotations have been revealed in radio galaxies, suggesting that the generation of very strong intra–cluster magnetic fields may be connected with the cooling flow process (Soker & Sarazin 1990; Godon, Soker & White 1998). On the other hand, the presence of significant magnetic fields ($\simeq$ 2 - 7 μG) has also been suggested in clusters without a cooling flow. For example, in the Coma cluster the measurements of Faraday rotation of polarized radiation through the hot ICM leads to a magnetic field of 2 μG (Kim et al. 1990) and 6 μG (Feretti et al. 1995).

In agreement with previous results obtained by studying individual clusters, Kim, Tribble & Kronberg (1991) analyzed the RM of radio sources in a sample of Abell clusters and found that μG–level fields are widespread in the ICM, regardless whether they do or do not have a strong radio halo. Moreover, by studying several clusters without cooling flow, Clarke, Kronberg & Böhringer (2001) obtained magnetic fields of 4 - 8 μG. By analyzing the spatial distribution of the RMs it is also possible to estimate the coherence length of the magnetic field: magnetic fields are not regularly ordered on cluster (Mpc) scales, but have coherence scales between 5 and 10 kpc (e.g. Carilli & Taylor 2002).

The observations are often interpreted in terms of the simplest possible model considering a constant field throughout the whole cluster. However, both theoretical models and numerical simulations suggest that the magnetic field distribution depends on the thermal gas density and therefore would decline with increasing the distance from the cluster center (e.g. Jaffe 1980; Dolag, Bartelmann & Lesh 1999; Dolag et al. 2001). In addition, it should be pointed out that recent studies on the physical uncertainties associated with this method for the measurements of magnetic fields (Newman, Newman & Rephaeli 2002) and studies on the RM contribution local to the source (Rudnick & Blundell 2003) have provided some critiques and demonstated serious problems with how RM limits or values are translated into estimates of cluster–wide field strengths.

Inverse Compton X–Ray Emission

It is well known that the strength of the magnetic fields can be derived by comparing inverse Compton X–ray emission and radio synchrotron radiation. From a quantum mechanical perspective, synchrotron radiation is directly analogous to IC emission, with synchrotron radiation being the up–scattering of the virtual photons that constitute the static magnetic field. Given a relativistic electron population, the IC emissivity is directly proportional to the energy density in the photon field, $U_{\rm ph}$, while the synchrotron emissivity is proportional to the energy density in the magnetic field, $U_{\rm B}$, leading to a simple proportionality between synchrotron and IC luminosity:

$$\frac{L_{\rm syn}}{L_{\rm IC}} \propto \frac{U_{\rm B}}{U_{\rm ph}} \tag{1.39}$$

Given that they originate from the same (assumed power–law) relativistic electron population, IC X–rays and synchrotron radio emission share the same spectral index, α. In most astrophysical circumstances $U_{\rm ph}$ is dominated by the cosmic microwave background (CMB); the Planck function at T = 2.73 K peaks near a frequency of $\nu_{\rm ph} \sim 1.6 \times 10^{11}$ Hz, hence IC X–rays observed at 20 keV ($\nu_{\rm IC} = 4.8 \times 10^{18}$ Hz), are emitted predominantly by electrons with $\gamma \sim 5000$, independent of redshift. The corresponding radio synchrotron emission from $\gamma = 5000$ electrons peaks at a (rest frame) frequency of $\nu_{\rm syn} \sim 4.2(B/1\mu{\rm G})\gamma^2$ Hz $= 100(B/1\mu{\rm G})$ MHz. Note that, unlike Faraday rotation measurements, the geometry of the field does not play a critical role in this calculation, except in the context of the electron pitch–angle distribution.

By comparing the non–thermal hard X–ray emission (see Sect. 1.3.3) detected in the Coma cluster with the diffuse radio emission (the halo Coma C), Fusco-Femiano et al. (1999) obtained a magnetic field of 0.15 μG. While this value is quite consistent whit those suggested by the equipartition magnetic field, the existing models were not able to reconcile an IC origin of the hard X–ray flux with the estimates of magnetic field intensities derived from RM observations, which are an order of magnitude higher. Goldshmidt & Rephaeli (1993) suggested that this discrepancy could be alleviated by taking into account the expected spatial profiles of the magnetic field and relativistic electrons. More recently, Brunetti et al. (2001b) and Petrosian (2001) showed that IC models including the effect of more realistic electron spectra combined with the expected spatial profiles of the magnetic field and anisotropies in the pitch–angle distribution of the electrons allow higher values of the intra–cluster magnetic field , in better agreement with the Faraday rotation measures. In particular Brunetti et al. (2001b), by considering the observed radio and X–ray spectra, the electron inverse Compton and synchrotron radiative lifetimes, and reasonable mechanisms for particle reacceleration, concluded that the magnetic field in the Coma cluster varies smoothly from 2$\pm$1 μG in the cluster center, to 0.3$\pm$0.1 μG at 1 Mpc radius.

Alternatively, different interpretation to the IC model for the hard X–ray excess detected in the Coma cluster have been proposed (see Sect. 1.3.3).

1.3.3 Extreme Ultraviolet and Hard X–Ray Emission

Recent researches on clusters of galaxies have unveiled new spectral components in the ICM of some clusters, namely a extreme–ultraviolet (EUV) and soft X–ray excess discovered by *EUVE* (Lieu et al. 1996a) and *ROSAT* (e.g. Bonamente et al. 2002), and a hard X–ray (HXR) excess detected by *BeppoSAX* (Fusco-Femiano et al. 1999) and *RXTE* (Rephaeli, Gruber & Blanco 1999). Several explanations have been proposed for the origin of this radiation; however, at present, not only there is no conclusive evidence in favor or against any of these models, but also there is still no consensus on the data.

EUV/Soft X–Ray Emission

Clusters of galaxies are strong emitters of X–rays, which originate from a diffuse and hot phase of the ICM (see Sect. 1.2.2). At the typical temperatures of $T \sim$ (1 - 10) $\times 10^7$ K, the bulk of the hot ICM radiation is detected near energies of 1 keV and above; intervining Galactic absorption is responsible for a substantial reduction of flux below $\sim$ 1 keV. The soft X–ray band around 0.25 keV and the EUV band offer a unique windows to investigate the presence of other emitting/absorbing phases of the ICM.

Recently, observations of clusters of galaxies with the *Extreme Ultraviolet Explorer* (*EUVE*) have revealed EUV emission ($\sim$ 70 - 200 eV energy range) in excess of that expected from the previously observed X–ray emitting ICM. EUV observations suggest that rich clusters generally have EUV luminosities of $\sim 10^{44}\,\mathrm{erg\,s^{-1}}$, and have spectra which decline rapidly in going from the EUV to the X–ray band. The problem of the physical origin of the EUV emission was immediately raised: the excess EUV emission relative to the extrapolation of the X–ray emission to the *EUVE* energy range, detected in several clusters, suggests that thermal bremsstrahlung from the hot ($\sim 10^8$ K) gas could not be entirely responsible for the EUV emission. Although there has been some controversy on the reality of this EUV emission, it now seems well established at least for Coma (Lieu et al. 1996a) and Virgo (Lieu et al. 1996b; Berghöfer, Bowyer & Korpela 2000; Bonamente, Lieu & Mittaz 2001), while there is no consensus on Abell 1795 (Mittaz, Lieu & Lockman 1998; Bonamente, Lieu & Mittaz 2001), Abell 2199 (Bowyer, Lieu & Mittaz 1998; Kaastra et al. 1999; Lieu, Bonamente & Mittaz 1999) and Abell 4038 (Bowyer, Lieu & Mittaz 1998). In all of the cases, except A2199, there is an associated soft X–ray excess seen in the *ROSAT* PSPC spectra of the clusters. The ratio of *EUVE* to PSPC fluxes and the correction for Galactic absorption indicate that the emitted spectrum drops rapidly with photon energy across the *EUVE* band. A recent study of 38 X–ray selected clusters observed by *ROSAT* PSPC show soft X–ray excess (0.2 - 0.4 keV) in a large fraction of the sources, thus possibly proving that the thermal radiation from the hot ICM may be not solely responsible for the majority of clusters soft X–ray spectra (Bonamente et al. 2002).

The excess EUV emission can be interpreted as due to two different mechanisms: thermal radiation from a warm (10^5 - 10^6K) gas, as first suggested by Lieu et al. (1996a), or IC emission of relativistic electrons either on the CMB or on stellar light originating in galaxies (Hwang 1997; Bowyer & Berghöfer 1998; Enßlin & Biermann 1998; Sarazin & Lieu 1998; Enßlin, Lieu & Biermann 1999). Note that although it is natural to suggest a thermal emission model, given that the X–ray emission from clusters is produced by thermal emission from diffuse gas with a higher temperature, there are several concerns with this hypothesis. Apart the difficulty in understanding how different components of gas at grossly different temperatures could retain their separate identity, the most serious one is that gas at these temperatures is near the peak of the radiative cooling curve and hence cools rapidly, requiring a substantial energy input to sustain the gas at these temperatures. Only one model has been proposed to account for this gas heating (Fabian 1997). Besides, in this thermal model the bulk of the radiation would be line emission, but a search for the O VI line did not detect the line in clusters which show EUV emission (Dixon, Hurwitz, & Ferguson 1996).

On the other hand, non–thermal models (Sarazin & Lieu 1998; Bowyer & Berghöfer 1998; Lieu, Bonamente & Mittaz 1999; Enßlin, Lieu & Biermann 1999; Atoyan & Völk 2000; Brunetti et al. 2001a) seem able to account for the excess EUV emission.

Hwang (1997) first examined the hypothesis that the source of the diffuse EUV flux is IC scattering by electrons that are a low energy extrapolation of electrons producing the observed synchrotron emission (such as radio halos); these electrons are scattered against the CMB radiation.

Sarazin & Lieu (1998) first explored the possibility that EUV radiation in clusters of galaxies could be produced by IC scattering of CMB radiation by a population of very low energy cosmic ray electrons in the ICM. The cosmic ray electrons, which might have been produced by supernovae in galaxies, by radio galaxies, or by particle acceleration in intra–cluster shocks, would have Lorentz factors of $\gamma \sim 300$, and would lose energy primarily by emitting EUV radiation. These particles have long lifetimes (of the order of few Gyr), thus these electrons might represent a relic population of cosmic rays produced by non–thermal activity over a substantial fraction of the history of the cluster. The required energy in cosmic ray electrons is typically 1 - 10% of the thermal energy content of the ICM (Sarazin & Lieu 1998).

This mechanism was also considered by Bowyer & Berghöfer (1998). Their model shows that the EUV emission can not be produced by IC radiation from electrons which are an extrapolation of the distribution which produces the observed radio emission, but that an additional component of low energy cosmic rays in required, in agreement with Sarazin & Lieu (1998).

Hard X–Ray Emission

Non–thermal hard X–ray radiation (HXR) was predicted in 1970's in clusters of galaxies showing extended radio emission, because of IC scattering of CMB photons by the same radio synchrotron electrons (e.g. Willson 1970; Rephaeli 1979). The severe energy losses associated with the relativistic electrons with $\gamma \sim 10^4$ make the non–thermal phenomena due to synchrotron and IC of relativistic electrons transient phenomena. However, if the acceleration processes occur during some violent phenomenon such as cluster mergers, some level of reacceleration may be expected due to the presence of turbulence in the ICM, thus maintaining these electrons for longer times (Brunetti et al. 2001a,b). These non–thermal emissions should then only be present in clusters with evidence for a recent or ongoing merger (see also Chapter 2).

Hard X–ray emission in excess of the thermal emission and detected as a non–thermal tail at energies $\gtrsim$20 keV has been seen in at least three clusters. The Coma cluster, which is undergoing at least one merger and which has a radio halo, was detected with both *BeppoSAX* and *Rossi X–ray Timing Explorer* (RXTE) (Fusco-Femiano et al. 1999; Rephaeli, Gruber & Blanco 1999; Rephaeli & Gruber 2002). The luminosity of Coma in the 20 - 80 keV range is $L_{\rm HXR} \sim 4 \times 10^{43}\,{\rm erg\,s^{-1}}$. *BeppoSAX* has also detected Abell 2256 (Fusco-Femiano et al. 2000) and Abell 754 (Fusco-Femiano et al. 2003), two other merger clusters with strong diffuse radio emission, and possibly Abell 2199 (Kaastra et al. 1999), although the evidence is less compelling for this case. Note that a non–thermal hard X–ray detection of Abell 2199 would be surprising, as this cluster is very relaxed and has no radio halo or relic (Kempner & Sarazin 2000).

As already stated in Sect. 1.3.2, when applied to the Coma cluster, the interpretation of the HXR based on the IC model requires values of the volume averaged magnetic field $B < 0.2\mu$G, which is much smaller than B values of several μG deduced from Faraday rotation (e.g. Eilek 1999; Giovannini et al. 1993; Kim et al. 1990; Clarke, Kronberg & Böhringer 2001). However, detailed IC models have reduced this discrepancy (Sect. 1.3.2) and, in addition, it should be pointed out that RM measurements are quite difficult (e.g. Newman, Newman & Rephaeli 2002; Rudnick & Blundell 2003), thus this discrepancy needs to be considered critically.

Alternative explanations of the HXR excess have also been proposed, based on acceleration of electrons from the thermal bath and bremsstrahlung radiation from these particles (Enßlin, Lieu & Biermann 1999; Blasi 2000; Dogiel 2000; Sarazin & Kempner 2000). However, as stressed by Petrosian (2001), because of the extreme inefficiency of the bremsstrahlung process this will require input of 10^5 times more energy than observed into the ICM, which will approximately double its temperature every 3×10^7 yr. To avoid rapid excessive heating of the ICM the HXR emission must be short lived ($< 3 \times 10^7$ yr) or the non–thermal electron spectrum is cutoff rapidly at low energies.

The issue of non–thermal radiation is clearly related to the problem of acceleration of particles: although the common wisdom is that the acceleration occurs during mergers of subclusters, there are several arguments which complicate this simple picture. We will discuss this important issue in Chapter 2.

Chapter 2

Modeling the Non–thermal Emission from the ICM

2.1 Introduction

As discussed in Sect. 1.3, the diffuse radio emission from halos and relics, produced by synchrotron radiation, and hard X–ray radiation demonstrate that the ICM consists not only of the hot gas emitting thermal X–rays, but also of non–thermal components, i.e. magnetic fields and relativistic particles. In particular, the radiation from diffuse radio sources is due to synchrotron emission by relativistic electrons of Lorentz factor $\gamma \sim 10^4$ in a magnetic field of strength $B \sim \mu$G. The presence of this diffuse emission has important theoretical implications for the non–thermal content of the ICM and the origin of the emitting electrons is still a matter of debate. In particular, the difficulty in explaining the extended radio halos arises from the combination of their Mpc size and the short radiative lifetime of the radio emitting electrons. Indeed, the diffusion time necessary to the radio electrons to cover such distances is orders of magnitude greater than their radiative lifetime. To solve this problem, two alternative scenarios have been historically proposed: the primary and the secondary electron models.

In this Chapter we will discuss the relevant processes for the relativistic electrons in the ICM and the possible mechanisms responsible for the production of the radio–emitting electrons. In particular, we will focus on radio halos and summarize some of the observational diagnostics which may help in discriminating among the different models proposed so far for their origin.

2.2 Physics of the Relativistic Plasma

Before discussing the origin of the radio–emitting electrons in clusters of galaxies, it is convenient to review the basic processes which modify the energy and spectrum of the relativistic electrons, with particular attention to the basic concepts of acceleration mechanisms (Sect. 2.2.3).

The relativistic electrons in extragalactic radio sources are subject to several processes that change their energy with time. More specifically, the time evolution of the energy of relativistic electrons in the ICM (Sect. 2.2.1) is determined by the competing processes of losses (Sect. 2.2.2) and accelerations (Sect. 2.2.3).

2.2.1 The Basic Equations of Particle Evolution

In order to consider the general evolution of the particle spectrum, a kinetic theory approach is suitable (e.g., Melrose 1980; Livshitz & Pitaevskii 1981; Blandford 1986; Blandford & Eichler 1987; Eilek & Hughes 1991, and reference therein). Let $f(\mathbf{p})$ be the distribution function of the particles (with implicit time dependence): $f(\mathbf{p})d\mathbf{p}$ is the number of particles in the element $d\mathbf{p}$ of momentum space. The description of the behaviour of this distribution function is given by the Boltzmann equation:

$$\frac{\mathrm{d}f(\mathbf{p})}{\mathrm{d}t} = \left(\frac{\partial f}{\partial t}\right)_{\mathrm{coll}} + \left(\frac{\partial f}{\partial t}\right)_{\mathrm{diff}} \tag{2.1}$$

Since f may be a function of momentum $\mathbf{p}$, position $\mathbf{r}$ and time t, the total time derivative is to be interpreted according to:

$$\frac{\mathrm{d}}{\mathrm{d}t} \to \frac{\partial}{\partial t} + \mathbf{v}\cdot\frac{\partial}{\partial \mathbf{r}} + \mathbf{F}\cdot\frac{\partial}{\partial \mathbf{p}} \tag{2.2}$$

where $\mathbf{v} = \mathrm{d}\mathbf{r}/\mathrm{d}t$ is the particle velocity, and $\mathbf{F} = \mathrm{d}\mathbf{p}/\mathrm{d}t$ the force acting on the particles.

The *diffusion* term in Eq.(2.1) describes spatial diffusion, while the *collision* term accounts for all the physics of collisions and scattering (e.g. charged particles interact with one another directly via Coulomb collisions and collectively via the generation and damping of plasma waves). In particular, in case of no spatial diffusion, from Eq. 2.1 the evolution of the particle distribution in a given field of plasma waves (both the distributions of waves and of electrons are supposed to be isotropic, so that $f(\mathbf{p})\mathrm{d}\mathbf{p} = 4\pi p^2 f(p)dp$) can be written in terms of spherical coordinates as:

$$\frac{\partial f(p)}{\partial t} = \frac{1}{p^2}\frac{\partial}{\partial p}\left(p^2 D_{pp}(p)\frac{\partial f(p)}{\partial p}\right) \tag{2.3}$$

which is called the momentum–diffusion equation.
This equation describes the time evolution of an isotropic, spatially homogeneous phase–space density $f(p)$ when the electrons of distribution f are undergoing multiple weak scatterings. The statistical properties of the scattering are described by the momentum–diffusion coefficient $D_{pp}(p)$.

Eq. 2.3 can be transformed from a diffusion equation that describes the evolution of the particle phase–space density to one that describes the evolution of the particle number density. For an isotropic distribution of particles, the number density $N(p)$ is related to the phase–space density by:

$$N(p) = 4\pi p^2 f(p) \tag{2.4}$$

With the use of this relation, the momentum–diffusion equation 2.3 is transformed into the equation:

$$\frac{\partial N(p)}{\partial t} = \frac{\partial}{\partial p}\left[D_{pp}(p)\frac{\partial N(p)}{\partial p} - \frac{2}{p}D_{pp}(p)N(p)\right] \tag{2.5}$$

Adding a loss term:

$$\frac{\mathrm{d}p}{\mathrm{d}t} = -b(p) \tag{2.6}$$

where $b(p)$ is a generic loss coefficient, one can calculate the particle spectrum that results from a combination of acceleration (which may be thought of as a diffusion in momentum space, characterized by a diffusion coefficient D_{pp}) and loss processes. One has that the time evolution of a distribution of highly relativistic particles can be described by:

$$\frac{\partial N(p)}{\partial t} = \frac{\partial}{\partial p}\left[D_{pp}(p)\frac{\partial N(p)}{\partial p} - \frac{2}{p}D_{pp}(p)N(p) + b(p)\,N(p)\right] \tag{2.7}$$

This equation is also commonly written in terms of the energy distribution (still assuming isotropy):

$$N(E) = 4\pi p^2 f(p)\frac{\mathrm{d}p}{\mathrm{d}E} = N(p)\,\frac{\mathrm{d}p}{\mathrm{d}E} \tag{2.8}$$

For relativistic particles, $E = cp = \gamma mc^2$, and in terms of the Lorentz factor γ Eq. 2.7 can be written as:

$$\frac{\partial N(\gamma)}{\partial t} = \frac{\partial}{\partial \gamma}\left[\left(\frac{D_{pp}(p)}{p^2}\right)\gamma^2\frac{\partial N(\gamma)}{\partial \gamma} - 2\gamma\left(\frac{D_{pp}(p)}{p^2}\right)N(\gamma) + \left(\frac{b(p)}{p}\right)\gamma N(\gamma)\right] \tag{2.9}$$

This basic equation describes the evolution of the particle spectrum, subject to particular acceleration processes (described in $D_{pp}(p)$) and loss processes (described in $b(p)$). The nature of the solutions is sensitive to initial and boundary conditions, as well as any assumed injection or leakage terms and the forms of $D_{pp}(p)$ and $b(p)$. By explicitating the time dependence it is possible to rewrite Eq. 2.9 as:

$$\frac{\partial N(\gamma,t)}{\partial t} = \alpha(t)\,\frac{\partial}{\partial \gamma}\left[\gamma^2\frac{\partial N(\gamma,t)}{\partial \gamma}\right] + \frac{\partial}{\partial \gamma}\left\{\left[-2\alpha(t)\gamma + \beta(t)\gamma^2\right]N(\gamma,t)\right\} \tag{2.10}$$

where the terms containing $\alpha(t)$ take into account acceleration processes while the term containing $\beta(t)$ takes into account radiative loss processes. For a general treatment of the solution of Eq.(2.10) we refer the reader to Kardashev (1962). Some additional more recent applications can be found in a number of papers (e.g., Borovsky & Eilek 1986; Sarazin 1999; Brunetti et al. 2001a; Petrosian 2001 and references therein).

In the next Sections we will briefly summarize the leading mechanisms at work and derive the expressions for the loss term and the diffusion coefficient in different cases.

2.2.2 Particle Losses

Relativistic electrons with energy $\gamma\, m_{\mathrm{e}} c^2$ lose energy via different processes:

- Relativistic electrons mixed with a thermal plasma lose energy via *ionization losses* and *Coulomb collisions*:

$$\left(\frac{d\gamma}{dt}\right)^{-}_{\mathrm{ion}} = -1.2\times 10^{-12} n_{\mathrm{e}} \left[1+\frac{\ln(\gamma/n_{\mathrm{e}})}{75}\right] \tag{2.11}$$

  where n_{e} is the number density of the thermal electrons in the ICM.

- If the relativistic electrons are confined into an expanding region, they lose energy via *adiabatic expansion*:

$$\left(\frac{d\gamma}{dt}\right)^{-}_{\mathrm{ex}} = -\frac{1}{R}\frac{dR}{dt}\gamma \sim 10^{-11}\gamma\frac{v_{\mathrm{ex}}(t)}{c}\frac{1}{R(t)_{\mathrm{kpc}}} \tag{2.12}$$

  where v_{ex} and R are the expansion velocity and dimension of the region, respectively.

- Relativistic electrons in a magnetic field B lose energy via *synchrotron radiation*:

$$\left(\frac{d\gamma}{dt}\right)^{-}_{\mathrm{syn}} = -1.9\times 10^{-9}\gamma^2 B^2 \sin^2\vartheta \tag{2.13}$$

  where ϑ is the pitch angle of the emitting electrons (for an isotropic distribution of velocities, by averaging over angles one obtains: $\langle B^2 \sin^2 \vartheta \rangle = 2/3B^2$), and via *inverse Compton* scattering with photons of energy density $\omega_{\rm ph}$:

$$\left(\frac{d\gamma}{dt}\right)^{-}_{\rm IC} = -3.2 \times 10^{-8} \gamma^2 \omega_{\rm ph} \tag{2.14}$$

where $\omega_{\rm ph}$ in our applications will be that of the cosmic microwave background (CMB). By taking into account that $\omega_{\rm ph} = B^2_{\rm CMB}/8\pi$, with $B_{\rm CMB} = 3.18\,(1+z)^2\ \mu$G, it is possible to write a single formula for the synchrotron and IC losses:

$$\left(\frac{d\gamma}{dt}\right)^{-}_{\rm syn+IC} \approx -1.3 \times 10^{-21} \gamma^2 \left[\left(\frac{B}{1\mu{\rm G}}\right)^2 + 10 \times (1+z)^4\right] \tag{2.15}$$

2.2.3 Particle Acceleration

Charged particles undergo a net energy gain in the presence of electric fields. In particular, a proper *acceleration* of charged particles occurs when there is some process which selects some small fraction of the entire particle population and transfers all of the injected energy to this population. Relevant acceleration processes in clusters of galaxies are Fermi–type acceleration, acceleration of charged particles by interaction with turbulent plasma waves and acceleration by shocks. These common acceleration mechanisms in diffuse astrophysical plasmas appear to be much more effective at accelerating electrons if the particles are already somewhat relativistic (e.g. Eilek & Hughes 1991). Thus these processes might better be called *reacceleration*, and some other mechanism must be acting to inject the electrons at mildly relativistic energies. In general, a test–particle approach is adopted, in which the influence of the accelerated particles on the wave field or subshock is neglected.

The simplest type of acceleration would be *systematic acceleration* in an electrostatic field parallel to the magnetic field; however, there are some arguments against simple electrostatic acceleration (e.g. Melrose 1980) and one is led to the concept of *stochastic acceleration*. The essential requirements of a stochastic acceleration mechanism are (a) elementary interactions which cause the energy of the particles to change, and (b) a random process, e.g. scattering, which may or may not be independent of the elementary energy changes. Note that it is not necessarily obvious that average energy gains, rather that energy losses, will result. However, if one thinks in thermodynamic terms, then the energy of the particles should tend towards the mean energy or effective temperature of the turbulent motions. For example, if one ascribes an effective temperature to MHD turbulence it turns out to be exceedingly large and, consequently, any energy exchange mechanism with particles should result in a transfer of energy from the turbulence to the particles.

A general, stochastic acceleration may be thought of as a diffusion in momentum space, characterized by a diffusion coefficient D_{pp}, as seen in Sect. 2.2.1. However, the momentum–diffusion equation 2.3 is not always a convenient way of describing the effects of the acceleration. For semi–quantitative purposes it is convenient to have an estimate of the typical rate at which the energy of an individual particle increases. It is useful to introduce a coefficient $\langle \mathrm{d}E/\mathrm{d}t\rangle$ for systematic acceleration, which can be considered as a measure of the rate at which the average energy $\langle E\rangle$ per particle increases (in this contest the term systematic is referred to the average energy increase resulting from stochastic acceleration, and must not be confused with the systematic acceleration previously mentioned). Specifically, with $N(E)$ given by Eq. 2.8, Eq. 2.3 can be written in the form of a Fokker–Planck equation:

$$\frac{\partial N(E)}{\partial t} = -\frac{\partial}{\partial E}\left(\left\langle \frac{\mathrm{d}E}{\mathrm{d}t}\right\rangle N(E)\right) + \frac{1}{2}\frac{\partial^2}{\partial E^2}\left(\left\langle \frac{\mathrm{d}E^2}{\mathrm{d}t}\right\rangle N(E)\right) \tag{2.16}$$

The other Fokker–Planck coefficient $\langle \mathrm{d}E^2/\mathrm{d}t\rangle$ may be called the coefficient for diffusion in energy. Due to the effects of the acceleration, initially monoenergetic distribution of particles becomes spread out in energy. Specifically, the variance in the energy increases at a rate $\langle \mathrm{d}E^2/\mathrm{d}t\rangle$: this increase in the spread in energy is in addition to the systematic increase in energy $\langle \mathrm{d}E/\mathrm{d}t\rangle$.

Stochastic Acceleration: Fermi Mechanisms

As discussed above, the basic idea of stochastic acceleration mechanisms is that, although particles both gain and lose energy in elementary interactions, they gain energy on average. The first stochastic mechanism explored in detail was Fermi's (1949) mechanism involving collisions of cosmic rays with magnetized interstellar clouds (where magnetic fields and density enhancements act as magnetic mirrors).

The classic theory of Fermi contains three essential ingredients. The first is that when a particle (of velocity $v = \beta c$ and Lorentz factor γ) is reflected by a cloud (which has a random velocity V and an average separation L with other clouds), its energy changes: the energy increases if it hits the cloud head–on and decreases if it has an overtaking collision. The second ingredient is that, under the assumption of isotropic distribution of the clouds, the particles remain isotropic. The third ingredient is that the rate of head–on collisions is a bit greater than the rate of overtaking collisions, and hence in this process the energy of a particle increases on average.

By considering that in the rest frame of the cloud the energy of the particle does not change, it is possible to calculate Fokker–Planck coefficients, which result (Melrose 1980):

$$\left\langle \frac{\mathrm{d}E}{\mathrm{d}t} \right\rangle = \frac{4V^2}{3Lc}\left(\frac{v}{c}\right) E \tag{2.17}$$

$$\left\langle \frac{\mathrm{d}E^2}{\mathrm{d}t} \right\rangle = \frac{2V^2}{3Lc}\left(\frac{v}{c}\right)^3 E^2 \tag{2.18}$$

where the numerical factors are model–dependent.

Thus Fermi acceleration may be described by a Fokker–Planck equation 2.16 with coefficients where the net rate of change in energy is second–order in V/c. Note that the Fokker–Planck equation for Fermi acceleration is equivalent to Eq. 2.10 (with no losses), where in the latter the term for systematic acceleration (the second term in the right hand side) is a factor of 2 that of random acceleration (the first term in the right hand side).

It is relevant to note that Fermi acceleration may also be described by an isotropic diffusion equation in momentum space (Eq. 2.3), with the diffusion coefficient given by:

$$D_{pp}(p) = \frac{V^2}{3Lv}p^2 \tag{2.19}$$

Processes such that $D_{pp}(p) \propto p^2$ lead to an acceleration rate which has the functional form $dE/dt \approx E/\tau_F$, where τ_F is some characteristic acceleration rate independent of the energy. Any process which yelds this form is referred to as a *'Fermi process'*.

In the literature "Fermi acceleration" is used either in the specific sense of Fermi's original paper, or in a generic sense for any stochastic acceleration.

Generalization of Fermi Mechanisms

Three among the many suggested variations and generalizations of Fermi mechanisms are worth discussing. One is to consider situations in which only head–on encounters (and no overtaking encounters) occur (e.g. Wentzel 1964). In this case, one finds that the rate of change in energy is first–order in V/c. The main application of this idea is acceleration by shocks (see below).

The second generalization of Fermi–type acceleration is based on invoking an alternative mechanism for changing the energy of the particles: as well as being due to reflections from moving magnetized blobs, energy changes can occur due to a varying magnetic field. The so–called *betatron effect* (Swann 1933) involves acceleration by the electric field associated with a time–varying magnetic field, where the electron energy changes due to longitudinal field variations are given by the adiabatic invariance of their magnetic moments. In its simplest form, in order to accelerate particles the betatron effect requires a systematic increase in the magnetic field strength, and the particles are assumed to escape after magnetic compression. However, if some scattering process operates, random changes in magnetic field strength will cause a stochastic acceleration, called *magnetic pumping* (Berger et al. 1958)

The third type of generalization is particularly important and is based on the

the fact that the rate of acceleration increases as the characteristic frequency of the turbulent motions increases. This is because the electric field associated with turbulent fluctuations captures an ever increasing fraction of the total oscillation energy as the frequencies increase (Tsytovich 1977). Consequently, the idea is that the energy changes associated with a particle subjected to MHD turbulence (in the form of small or moderate amplitude waves) might lead to effective acceleration. As shown e.g. by Kulsrud & Ferrari (1971) and Melrose (1980), acceleration by MHD turbulence can be particularly effective when combined with an efficient scattering mechanism such as resonant scattering.

In particular, for MHD turbulence involving changes of order δB in the magnitude of B with a typical frequency ω, the coefficient for systematic acceleration is:

$$\left\langle \frac{\mathrm{d}E}{\mathrm{d}t} \right\rangle = \pi\omega \frac{v_{\mathrm{A}}}{c} \left(\frac{\delta B}{B}\right)^2 \left(\frac{v}{c}\right) E \tag{2.20}$$

where v_{A} is the Alfvén velocity.

MHD Waves

Long wavelength MHD waves are likely to be responsible for the acceleration of relativistic particles, because they are the ones that are likely to be externally generated by fluid–like instabilities, and they are the ones that can resonate with the particles thus allowing energy and momentum transfer. In the treatment of particle interaction with waves, it is generally assumed that the astrophysical plasmas are constitute by a mixed plasma consisting of some relativistic electrons and ions, and some cool, inertial plasma. In this picture the waves are carried by the mixed plasma, and can interact selectively with the relativistic particles, thus accelerating or maintaining a significant high energy tail on the electron distribution.

A magnetized plasma can support two types of long wavelength waves: Alfvén and magnetosonic.

- *Alfvén waves* are circularly polarized, transverse waves which propagate along the magnetic field. In the low–amplitude limit they are not compressive. These waves look like transverse oscillations of the field lines and the restoring force can be thought of as the tension in the field lines. Their dispersion relation is (e.g. Krall & Trivelpiece 1973):

$$\omega^2 = \frac{k^2 v_A^2 \cos^2\theta}{1 + v_A^2/c^2} \tag{2.21}$$

where $v_A = (B^2/4\pi\rho)^{1/2}$ is the Alfvén speed, and θ is the angle between $\mathbf{k}$ and $\mathbf{B}$. Alfvén waves exist for frequencies $\omega < \Omega_p = eB/m_pc$, the ion gyrofrequency. For frequencies $\Omega_p < \omega < \Omega_e$ (where Ω_e is the electron gyrofrequency), these waves turn into *whistlers* and approach *electron–cyclotron waves* as $\omega \to \Omega_e$.

- *Magnetosonic waves* are compressive waves which propagate across or at an angle to the magnetic field. In the limit of $\theta \to \pi/2$ (propagation across the field) they become mostly longitudinal waves, the restoring forces are plasma pressure and magnetic pressure. In a warm plasma with sound speed c_s, the dispersion relation has two branches, the fast (+ solution) and slow (− solution) modes (e.g. Krall & Trivelpiece 1973):

$$\omega_\pm^2 = \frac{1}{2}\frac{k^2}{1 + v_A^2/c^2}\left[v_A^2 + c_s^2 \pm \sqrt{\left(v_A^2 + c_s^2\right)^2 - 4v_A^2 c_s^2 \cos^2\theta}\right] \tag{2.22}$$

Both these waves affect the relativistic particles through their fluctuating electring fields, and this interaction is strongest when the wave and particle are in resonance (the wave and particle speeds are well matched), so that energy and momentum transfer are the most effective.

The fundamental resonance in a magnetized plasma, and the relevant one for Alfvén waves, is the *cyclotron resonance* (also called the *Doppler resonance*), given by:

$$\omega - k_{\|} v_{\|} - n^* \Omega_\gamma = 0 \tag{2.23}$$

where $k_{\|}$ and $v_{\|}$ are the components of the wavenumber and velocity parallel to the magnetic field, and $\Omega_\gamma = \Omega/\gamma$ is the relativistic gyrofrequency. In this resonance, the resonant particles see the wave Doppler–shifted to a multiple of their gyrofrequency. The most important resonance for electron interaction with Alfvén waves is the $n^* = -1$ resonance, while for protons is the $n^* = +1$ resonance (Melrose 1968). It is possible to demonstrate that for relativistic particles there is a correspondence between the particle energy and the wavelength with which it can resonate: the particle does not 'see' all turbulent wavenumbers, but only those above $k_{\rm res}(p) = \Omega m/p$.

The $n^* = 0$ limit of the cyclotron resonance is:

$$w = k_{||} v_{||} \tag{2.24}$$

which is the Landau (or Cerenkov) resonance. This describes a wave which the resonant particles see Doppler shifted to zero frequency. The particle energy gain can be understood as arising from the force of interaction between the magnetic momentum of the particle and the gradient of the wave field, as the particle 'rides' the wave. This is the important resonance for acceleration by long wavelength magnetosonic waves. The resonance depends only on pitch–angle, so that all wavenumbers can interact with a given particle energy.

An interesting detail of this acceleration mechanism is that it is effective only when cyclotron–resonant scattering maintains a pitch–angle isotropy. Thus, without pitch–angle scattering to redistribute the energy gained, the acceleration rate will be much slower and will not necessarily be Fermi–like. Results quoted in the literature generally assume isotropy. In summary, MHD turbulence can accelerate relativistic electrons, if the necessary cyclotron–resonant Alfvén waves exist in the plasma.

The rate of particle acceleration, by either resonance, depends on the energy spectrum of the waves. The energy spectrum of the waves is defined by $\Delta B^2 = 8\pi \int W(k)dk$, so that $W(k)$ is the wave energy density per unit wavenumber. The wave dissipation, $dW(k)/dt = -\Gamma(k)W(k)$, can be calculated explicitly for Alfvén and magnetosonic waves in the linear limit (e.g. Lacombe 1977; Eilek 1979). If the waves are driven externally, the resultant wave spectrum depends on the nature of the driving and damping processes, so that it is not possible to predict a unique, 'universal' spectrum. A great range of turbulent spectra is possible, depending on conditions in the system.

Once the wave spectrum is known, it is possible to evaluate the momentum–diffusion coefficient $D_{pp}(p)$. In particular, acceleration by long–wavelength magnetosonic waves is related to the previously discussed mechanism of magnetic pumping, in which rapid pitch–angle scattering allows adiabatic compression to work, and in which the acceleration rate is Fermi–like ($D_{pp}(p) \propto p^2$). On the contrary, acceleration by Alfvén waves, through the cyclotron resonance, leads to a diffusion coefficient (Lacombe 1977; Eilek 1979) that is quite different to that for Fermi acceleration.

Acceleration by Shocks

Shock acceleration is a well known astrophysical process (see Drury 1983 and Blandford & Eichler 1987 for a review). Energetic charged particles can be efficiently accelerated in shock waves either by drifts in the electric fields at the shock (e.g. Webb, Axford & Terasawa 1983 and references therein), or by scattering back and forth across the shock in the magnetic turbulence present in the background plasma (e.g. Bell 1978a,b; Blandford 1979; Drury 1983). The latter mechanism is a variant of the first–order Fermi process, previously mentioned, and hence referred to as the *shock–Fermi process.*

The transition thickness of a collisionless shock wave is a few thermal–ion gyroradii. Particles of sufficient energy (e.g. those in the suprathermal tail of the energy distribution) will have gyroradii much larger than this scale and thus they can propagate across the transition without 'seeing' it. Therefore such particles can be scattered back and forth between upstream and downstream flows, and the only energy change that they will suffer will be that associated with the change of reference frame (defined by the upstream and downstream scattering centers). Alternatively, one can say that these particles are scattered back and forth by approaching (converging) magnetic mirrors.

In the simplest case, i.e. that of a steady state shock without losses and with a seed monoenergetic particle distribution, the accelerated spectrum which arises from this mechanism is a simple power law energy (or momentum) distribution (e.g., Bell 1978a,b; Blandford & Ostriker, 1978). In particular, a shock with compression factor r and Mach number $\mathcal{M}$ can accelerate particles to a power law in momentum $f(p) \propto p^{-\delta}$, with slope δ related to the Mach number and compression factor by the following expressions:

$$\delta = \frac{r+2}{r-1} = 2\frac{\mathcal{M}^2+1}{\mathcal{M}^2-1}. \tag{2.25}$$

The acceleration occurs diffusively, in the sense that particles scatter back and forth across the shock, gaining at each crossing and recrossing an amount of energy proportional to the energy of the particle itself, $\Delta E/E \sim V/c$, where V is the speed of the shock.

The Injection Problem

As seen in previous discussion, all stochasic acceleration processes share the requirement that waves can interact with the particles via the cyclotron resonance, so that the particles are scattered in pitch–angle. This requirement sets limits on the energy of particles that can be accelerated by waves.

Alfvén waves satisfy the cyclotron resonance 2.23, where higher particle energies resonate with longer wavelength waves. However, Alfvén waves exist only for frequencies $\omega < \Omega_p = eB/m_p c$, so there is a minimum particle energy which 'sees' the Alfvén waves. For protons, this minimum energy is:

$$\gamma_{\mathrm{min,p}} = 1 + 2\frac{v_{\mathrm{A}}^2}{c^2\mu^2} \tag{2.26}$$

where μ is the cosine of the pitch–angle ($v_{||} = v\mu$). Thus all protons with $v_{||} > 2v_{\mathrm{A}}$ can see the waves. For electrons the limiting energies are higher and one can distinguish two cases:

- high density plasma ($c^2\mu^2/v_{\mathrm{A}}^2 \gg m_{\mathrm{p}}^2/m_{\mathrm{e}}^2$): the minimum energy is:

$$\gamma_{\rm min,e} = 1 + \frac{m_{\rm p}}{m_{\rm e}} \frac{v_{\rm A}^2}{c^2\mu^2} \tag{2.27}$$

and the corresponding minimun kinetic energy for an electron is $m_{\rm p} v_{\rm A}^2/2\mu^2$. Therefore the resonance occurs only if $v_{\|} > (m_{\rm p}/(m_{\rm e}\mu))^{1/2}\, v_{\rm A}$.

- low density plasma ($c^2\mu^2/v_{\rm A}^2 \ll m_{\rm p}^2/m_{\rm e}^2$): the minimum energy is:

$$\gamma_{\rm min,e} = \frac{m_{\rm p}}{m_{\rm e}} \frac{v_{\rm A}}{c\mu} \tag{2.28}$$

Thus, while a significant number of low energy (thermal) protons can resonate with Alfvén waves and can in principle be accelerated, thermal electrons have less chance of acceleration: $\gamma_{\rm min,e}$ is indeed already mildly relativistic and thermal electrons are unaffected by the waves.

This is similar to the existence of a threshold energy for the shock–Fermi process: in order to be Fermi–accelerated, an electron must be able to scatter between the upstream and downstream flows, i.e. must have a gyroradius larger than the transition thickness of the shock. This implies a minimum energy for the electrons that can be accelerated. An estimate of this has been made by Peacock (1981), who showed that the electrons must already possess highly relativistic energy.

This is the so–called *injection problem*: no acceleration mechanism that depends on Alfvén waves resonance or shocks can accelerate electrons significantly from a subrelativistic, thermal population. The usual shock and turbulent acceleration models are truly reacceleration models: they start with already relativistic electrons and either accelerate these further or maintain them against losses. Therefore, if the plasma is created subrelativistic, the initial acceleration must be a two–stage process, with a first (injection) stage moving the electrons up in energy above the minimum (Eq. 2.27 or 2.28), and a second stage, either turbulent or shock–Fermi acceleration, moving the electrons up to the observed highly relativistic energies (Eilek & Hughes 1991).

2.3 Models for Radio Halo Formation

The problem for the origin of extended radio halos is related to the fact that the radiative lifetime of radio–emitting electrons is much shorter than any reasonable transport time over cluster scale.

Indeed, the radiative lifetime of relativistic electrons losing energy via synchrotron emission and IC scattering off the CMB photons (CMB) is given by (see Eq. 2.15):

$$\tau_{\rm sin+IC} \approx 2.46 \times 10^{9} \left[\left(\frac{B}{1\mu{\rm G}}\right)^{2} + \left(\frac{B_{\rm CMB}}{1\mu{\rm G}}\right)^{2} \right]^{-1} \left(\frac{\gamma}{10^{4}}\right)^{-1} \quad {\rm yr} \tag{2.29}$$

and for typical values for radio–emitting electrons in the ICM is of the order of $\sim 10^8$ yr. On the other hand, under reasonable assumptions for the diffusion coefficient, the average time scale to diffuse out to a radius of R is about (Berezinsky, Blasi & Ptuskin 1997; Colafrancesco & Blasi 1998):

$$\tau_{\rm diff} \approx 1 \times 10^{12} \left(\frac{R}{2\,{\rm Mpc}}\right)^{2} \left(\frac{E}{1\,{\rm GeV}}\right)^{-1/3} \left(\frac{B}{1\,\mu{\rm G}}\right)^{1/3} {\rm yr}\,. \tag{2.30}$$

and thus radio–emitting electrons (with energies $\gamma \sim 10^4$ or $E \sim 5$ GeV) have diffusion times over $\sim$ Mpc scale which are longer than the Hubble time. This means that the relativistic electrons producing the extended diffuse radio emission from halos need be continuously re–energized (*primary* electrons), or freshly injected on a cluster–wide scale (e.g. as result from the decay of charged pions produced in hadronic interaction, *secondary* electrons).

Primary and secondary electron models still constitute the basis of the more recent theoretical works developed on this argument.

2.3.1 Primary Electron Models

To solve the problem of the origin of extended radio halos, Jaffe (1977) first proposed continuous in situ reacceleration of the relativistic electrons. The in situ reacceleration scenario was quantitatively reconsidered by Schlickeiser, Sievers &

Thiemann (1987) who successfully reproduced the integrated radio spectrum of the Coma halo.

Harris, Kapahi & Ekers (1980) first suggested that cluster mergers may provide the energetics necessary to reaccelerate the relativistic particles. The role of mergers in particle acceleration and in the amplification of the magnetic fields was than investigated in more detail by De Young (1992) and Tribble (1993).

In the contest of primary models, one can distinguish two processes for the injection of relativistic electron populations in the ICM:

Acceleration by Shocks (Pop. A) :

Radio observations of supernovae indicate that strong shocks convert at least a few percent of their energy into the acceleration of relativistic particles. Thus, merger shocks may represent a natural acceleration mechanism for the relativistic electrons in galaxy clusters (e.g. Sarazin 1999). Particle acceleration by merger shocks has been studied in detail (e.g. Takizawa & Naito 2000; Miniati et al. 2001; Fujita & Sarazin 2001) and it might explain the apparent correlation between the non–thermal phenomena and the presence of merger activity in clusters of galaxies (e.g. Buote 2001 and references therein).

Re–accelerated Electrons (Pop. B) :

There is a number of sources of relativistic electrons in galaxy clusters. In particular active galaxies (e.g. radio galaxies), merger shocks, supernova and galactic winds can efficiently inject relativistic protons and electrons in the cluster volume over cosmological time (e.g. Sarazin 2002 and references therein). High energy electrons have very short radiative lifetimes and hence lose energy rapidly due to IC and synchrotron emission. However, when they reach energies of $\gamma \sim 100$ - 300 they have long lifetimes of ~ 3 - 5 Gyr, which are a relevant fraction of the ages of clusters, and thus they can be accumulated in the cluster volume. Cluster mergers may produce a significant level of turbulence in the ICM, in this case Alfvén waves and/or other Fermi–like processes diffuse in the cluster volume could reaccelerate $\gamma \sim 100$ - 300 relativistic electrons to the higher energies required to explain radio halos (e.g.

Brunetti et al. 2001b).

2.3.2 Secondary Electron Models

To avoid the energy loss problem of the radio–emitting electrons during their diffusion through the cluster, Dennison (1980) first pointed out that a possible source of the relativistic electrons in radio halos is the continuous injection due to the decay of charged mesons produced in hadronic interaction of energetic cosmic ray protons distributed throughout the cluster volume. The protons diffuse on large scales still surviving because their energy losses are negligible and they can inject in situ electrons.

This idea has recently been reconsidered in detail by Blasi & Colafrancesco (1999), and then by Dolag & Enßlin (2000), who assumed a radial profile of the cluster magnetic field taken from numerical simulations. In order to explain the connection between cluster mergers and radio halos, Enßlin (1999) proposed that relativistic protons are released from radio ghosts into the ICM during a cluster merger event. More recently, Miniati et al. (2001) have developed numerical simulations of cluster formation and calculated the injection of primary relativistic protons by strong shocks. These authors find that, under some assumptions, the resulting secondary electrons might produce diffuse synchrotron emission in agreement with some of the observed properties of radio halos.

2.3.3 Possible Diagnostics

From a theoretical point of view the above electron populations are very reasonable, thus it may be that all of them contribute to the origin of the relativistic electrons in the ICM. In addition it should be noticed that the final electron population may be due to a complicated mix of all the above reported processes. For example, shocks may accelerate relic electrons contributing to the Pop. B, but they can also (re)accelerate relativistic protons increasing the rate of injection of secondary electrons. In addition to the acceleration of relic electrons (Pop. B), cluster turbulence could (re)accelerate protons increasing the rate of injection of secondary electrons. Finally, secondary electrons can be (re)accelerated by shocks and/or cluster turbulence powered by a merger event (Pop. A, B).

A possibility to break the degeneracy on the origin of the emitting electrons might be provided by some observational diagnostics.

Diffusion Lengths

The $\sim$ Mpc size of most radio halos suggests that a population of electrons accelerated by shocks in the clusters (Pop. A) can not significantly contribute to the observed diffuse radio emission, as after the acceleration by a shock, the synchrotron emitting electrons have short ($\sim 10^8$ yrs, see Eq. 2.29) radiative lifetimes and they can not diffuse over the cluster volume.

In order to better quantify the typical diffusion length $R_{\rm d}$ of the radio electrons, one should derive the diffusion time $\tau_{\rm diff} \sim R_{\rm d}^2/(4\mathcal{K}(\gamma))$, where $\mathcal{K}(\gamma)$ is the spatial diffusion coefficient. By assuming a Kolmogorov spectrum of the magnetic field one obtains (Brunetti 2002):

$$\mathcal{K}(\gamma) \simeq 1.8 \times 10^{28} \left(\frac{L}{20\,\mathrm{kpc}}\right)^{2/3} \left(\frac{B}{1\mu\mathrm{G}}\right)^{-1/3} \gamma^{1/3} \tag{2.31}$$

where L is the largest coherence scale of the field. The diffusion length $R_{\rm d}$ is obtained when the diffusion time equals the radiative lifetime (Eq. 2.29). In the most interesting regime, when IC losses dominate (i.e., for $\gamma >> 10^3$ and $B < 3\mu$G), one obtains:

$$R_{\rm d}(\mathrm{kpc}) \sim 36 \left(\frac{\gamma}{10^4}\right)^{-1/3} \left(\frac{L}{1\,\mathrm{kpc}}\right)^{1/3} \left(\frac{B}{1\mu G}\right)^{-1/6} \tag{2.32}$$

More general results show that the maximum diffusion length (which depend on both the magnetic field and the gas density $n_{\rm th}$, resulting of the order of $\sim$ 70 - 100 kpc for $B \sim 1\mu$G and $n_{\rm th} \sim 10^{-3}$ - $10^{-4}\mathrm{cm}^{-3}$) is obtained for electrons with $\gamma \sim 10^2$ - 10^3, while radio–emitting electrons can not diffuse for more than about 30 kpc (Brunetti 2002).

Another possibility is given by a scenario in which a fast shock crosses the cluster center and accelerates the relativistic electrons across the cluster volume. In this case the diffusion time of the electrons is replaced by the crossing time of the shock, that should be shorther than the radiative lifetime of the radio emitting electrons. For a typical total extension of ~ 2 Mpc this would require an unreasonaby high Mack number of the shock $\mathcal{M} > 5$.

A detailed calculation of the electron population accelerated by merger shocks has been recently developed by Miniati et al.(2001). These authors calculate the resulting synchrotron radiation and they find indeed that the morphology of the resulting emission is similar to that of radio relics rather than to radio halos. Furthermore, due to the field compression in the shock, the emitted synchrotron radiation is highly polarized (as in the case of radio relic) in contrast with the very low polarization found in the radio halos.

Additional evidence against a direct link between merger shock acceleration and non–thermal emission has been obtained by Gabici & Blasi (2003) and Berrington & Dermer (2002), who have shown that the low Mach number expected in the merger shocks would accelerate a very steep spectrum of protons and electrons which can not account for the observed synchrotron spectrum of radio halos (also in the case of secondary models).

Radio brightness profiles

The timescale of the p–p collision, which is the process responsible for the injection of secondary electrons, is $\propto n_{\rm th}^{-1}$. Consequently, for a given number density of the relativistic protons, secondary electrons are expected to be injected in the denser regions and the radio emission would be stronger in the cluster core. In particular, in the framework of secondary electron models it is possible to predict the ratio between synchrotron and thermal bremsstrahlung X–ray brightness profiles.

Starting from an assumed power low energy distribution of the injected relativistic protons:

$$N_{\rm p}(E,r) = N_{\rm p}(r)E^{-s} \tag{2.33}$$

where $N_{\rm p}(r)$ gives the spatial distribution of the protons, it is possible to calculate the resulting energy distribution of the secondary electrons produced in inelastic interactions between cosmic ray nuclei and thermal protons in the ICM. In particular, following standard recipes for the calculation of proton–proton decay (e.g. Mannheim & Schlickeiser 1994) and assuming time independent conditions (e.g. Dolag & Enßlin 2000), it can be shown that the energy distribution of the relativistic electrons is also a power law :

$$N_{\rm e}(E,r) = C_{\rm e}\frac{n_{\rm th}(r)N_{\rm p}(r)}{B^2(r)+B^2_{\rm CMB}}\,E^{-\delta} \tag{2.34}$$

where $C_{\rm e}$ is a constant, and the slope of the electron spectrum is $\delta = \frac{4}{3}s + \frac{1}{3}$. In order to calculate the number density of the secondary electrons it is convenient to parameterize the number density of the relativistic protons in terms of that of the thermal plasma:

$$N_{\rm p}(r) = C_{\rm p}\,\mathcal{F}(r)\,n_{\rm th}(r)kT \tag{2.35}$$

where $C_{\rm p}$ is a constant, and $\mathcal{F}(r)$ gives the ratio between relativistic and thermal protons energy densities. The synchrotron brightness profile is thus given by:

$$b_{\rm syn}(y) = C_{\rm e}C_{\rm p}C_{\rm syn}\,\nu^{-(\delta-1)/2}\,kT \times \int_y n^2_{\rm th}(r)\,\mathcal{F}(r)\frac{B(r)^{(\delta+1)/2}}{B^2(r)+B^2_{\rm CMB}}\frac{r\,dr}{\sqrt{r^2-y^2}} \tag{2.36}$$

On the other hand, the thermal brightness emission from a cluster is given by :

$$b_{\rm th}(y) \propto \int_y n^2_{\rm th}(r)\,\Lambda(T)\frac{r\,dr}{\sqrt{r^2-y^2}} \tag{2.37}$$

and thus the ratio between synchrotron and thermal brightness depends on the quantity $\Phi(r) = \mathcal{F}(r)\,B(r)^{(\delta+1)/2}/(B^2(r)+B^2_{\rm CMB})$, which is $\propto \mathcal{F}(r)\,B(r)^{(\delta+1)/2}$ for a magnetic field strength $< 3\mu$G. More specifically, if $\Phi(r)$ is a decreasing function of r, the hadronic secondary model predicts a super–linear power law $b_{\rm syn}$-$b_{\rm th}$ relation.

So far, a quantitative comparison of the observed radio and thermal bremsstrahlung X–ray profiles was obtained for 5 extended radio halos (Govoni et al. 2001a; Feretti et al. 2001). In two cases a linear correlation exists between the radio and X–ray brightness (i.e. $b_{\rm r} \propto b_{\rm x}^{b}$, with $b \sim 1$) whereas in the remaining three cases a sub–linear trend is found (Coma: b=0.64, A2319: b=0.82, A2163: b=0.64), in contradiction with secondary model predictions.

In particular, a comparison between the synchrotron brightness profile expected from secondary models and the observed one for the Coma cluster shows that the theoretical profiles are considerably steeper than observed. This happens in the case of both flux freezing approximation ($B \propto n_{\rm th}^{2/3}$) and of a radial dependence of the field as that from numerical MHD simulations (Dolag, Bartelmann & Lesch 2002). These simulations suggest a rapid decrease of the field in the regions out of the cluster core ($B \propto n_{\rm th}$). In order to reproduce the observed brightness profile with secondary models, $\mathcal{F}(r)$ is then forced to rapidly increase with r. As a net result, one finds that secondary models can reproduce the profile of the Coma halo only by unreasonably forcing the energy density of the relativistic protons to be considerably larger than that of the thermal ICM out of the cluster radius (e.g. Brunetti 2002).

Integrated and radial spectral steepenings

Radio observations of the best studied radio halo, Coma C, have discovered a cut–off around 1 GHz in the integrated synchrotron spectrum (e.g. Deiss et al. 1997) and a strong steepening of the spectrum with increasing the distance from the center (Giovannini et al. 1993). The presence of a similar radial spectral steepening has been also found in the well studied radio mini–halo of the Perseus cluster (Sijbring 1993; see Chapter 5). The presence of spectral steepening has been found in a few other radio halos and mini–halos. However, the lack of statistics does not allow to understand if the synchrotron spectral properties of Coma and Perseus are common among radio halos and mini–halos.

Brunetti et al. (1999, 2001b) pointed out that synchrotron radial spectral steepenings are expected in the case of extended radio halos if the synchrotron radiation is emitted by reaccelerated electrons (Pop B). In these models, the maximum energy of the reaccelerated electrons is expected at $\gamma_{\rm c} \sim 2.5 \times 10^4(\tau_{\rm acc}/10^8\,{\rm yrs})^{-1}$, where $\tau_{\rm acc}$ is the reacceleration time. Since the Fermi II–like processes in the ICM give typical acceleration time scales $\tau_{\rm acc} > 10^7$ yr (e.g. Eilek & Weatherall 1999), it is $\gamma_{\rm c} < 10^5$. Consequently, a cut–off in the synchroyron spectrum might be present in the radio band. Another consequence of these models is that if the field strength in clusters decreases with distance from the center (e.g. Dolag, Bartelmann & Lesch 2002), the corresponding frequency of the cut–off in the synchrotron spectrum should decrease with the distance from the center yielding a possible radial steepening of the spectrum between two fixed frequencies.

On the other hand, as already discussed, if the spectrum of the primary protons is a power law, the secondary electron-positron pairs from $\pi^{\pm}$ decay have also a power low spectrum. This is still true ($\gamma > 10^3$), if the complete proton–proton cross section is taken into account in the calculations (e.g. Blasi 2001) and the spectrum ($\nu > 10$ MHz) of the synchrotron emission predicted by secondary models should be a straight power law without a cut–off. One possibility to obtain a cut–off in the spectrum of the secondary electrons, and thus in the emitted synchrotron spectrum, is to assume a cut–off in the energy distribution of the primary relativistic protons. This should be at $E_{\rm p} \leq 50$ GeV to have the cut–off of the spectrum from the secondary electrons at the $\sim$GHz. Although, at present, such a cut–off cannot be ruled out by direct observations, it should be stressed that it is very unlikely as it is in contrast with the observations of the spectrum of (galactic) cosmic rays and with the theoretical expectations from the most accepted acceleration mechanisms. Cosmic ray protons in the Galaxy are detected up to $E_{\rm p} \geq 10^{11}$ GeV and independently on their origin, no cut–off is observed at least up to $E_{\rm p} \sim 4 \times 10^6$ GeV. So far, all the mechanisms invoked to inject the primary population of relativistic protons in galaxy clusters do not predict a cut–off in the spectrum of the protons at low energies.

The discussed diagnostics seem to suggest that radio halos are powered by the synchrotron emission from electrons reaccelerated (Pop.B) in the cluster volume during merger events. However, this conclusion is based on detailed studies of only few radio halos. As a consequence, detailed observations are still required to better understand the origin of radio halos.

2.4 Models for Radio Relics Formation

Relic radio sources were originally considered as remnants of galaxies active in the past, and therefore of different and established origin with respect to radio halos. However, there are several difficulties with this interpretation, as for example the identification of a parent galaxy and the discovery of large relics. In particular, the latter led to the problem, already mentioned for the halos, that the radiative lifetime of the electron population is too short to allow the diffusion of relativistic electrons over very large distances.

In recent years, there is increasing evidence that relics are related to ongoing merger events: two current compelling scenarios are that relics are the result of first–order Fermi acceleration of relativistic particles in shocks produced during cluster mergers (Enßlin et al. 1998; Roettiger, Burns & Stone 1999) or are fossil radio sources revived by compression associated with cluster mergers (Enßlin & Gopal-Krishna 2001).

Concerning the latter one, Enßlin (1999) proposed that active radio galaxies fill large volume in the ICM with radio plasma which becomes rapidly invisible in the radio band because of radiative losses of the relativistic electrons. These fossil radio plasma, called "radio ghosts", are revived by adiabatic compression in shock waves produced in the ICM during cluster mergers (Enßlin & Gopal-Krishna 2001). In this contest, Enßlin & Brüggen (2002) have recently presented 3-D MHD simulations of a hot, magnetized bubble that traverses a shock wave in a much colder environment. The derived simulated maps reproduce very well the filamentary structure and polarization seen in a few relic sources with high resolution radio observations (Slee et al. 2001).

Chapter 3

Cooling Flows

3.1 Introduction

The X–rays emitted from clusters of galaxies represent a loss of energy of the ICM. Thermal bremsstrahlung and line emission depend on the square of the gas density (Eq. 1.13), which rises towards the cluster center (Eq. 1.36). As the density rises, the loss rate increases and the resultant cooling time–scale decreases. In the central region, the cooling rate of the ICM is sufficiently high that the particles lose their energy via radiation, as inferred from X–ray images of the cores of many clusters which show strongly peaked surface brightness distributions. The density of the gas then rises to maintain the pressure required to support the weight of the overlying gas in the rest of the cluster, causing a slow subsonic inflow of material towards the cluster center. This simple picture describes the physics of the process known as a *cooling flow*, which will be presented in Sect. 3.2 (see Fabian 1994 for a review).

The compression of the gas in cooling flows is expected to produce an amplification of the frozen–in cluster magnetic field, as discussed in Sect. 3.3.

High resolution X–ray studies with *XMM–Newton* have recently shown that the soft X–ray spectra of several cooling flow clusters of galaxies are inconsistent with standard cooling flow models, as the gas cools down to about 2 - 3 KeV but not to lower temperatures (e.g. Peterson et al. 2002b). This problem, which is still largely debated, will be discussed in Sect. 3.4.

3.2 The Standard Picture

The basic physics of the cooling flow mechanism is very simple, although the details are not. In the idealized hypothesis of homogeneous ICM, in which the gas has a unique temperature and density at each radius, it is possible to derive the expression for the radiative *cooling time*, $t_{\rm c}$, defined as the ratio of the specific thermal energy of the plasma and that radiated in X–rays (Eq. 1.13), as a function of the distance r from the cluster center:

$$t_{\rm c}(r) \propto \frac{T(r)^{1-\alpha}}{n_{\rm e}(r)} \tag{3.1}$$

where $n_{\rm e} = \rho/(1.83\mu m_{\rm p})$ (see Sect. 1.2.1). In the cases considered here, $t_{\rm c}$ exceeds the gravitational free–fall time, $t_{\rm grav}$, within the cluster, so the gas can be considered to be in quasi–hydrostatic equilibrium. In the hypothesis that thermal conduction is neglibible (conduction is probably inhibited in the ICM by tangled magnetic fields, e.g. Jafelice 1992) and in the absence of heating, a hydrostatic atmosphere will inevitably begin to cool substantially after about one radiative cooling time. Since the gas density ρ is assumed to follow a β–model distribution (Eq. 1.36), the ICM is densest in the core of a cluster and therefore the cooling time is shortest there. Cooling will start in the center of the cluster and work outward. As the gas begins to cool, it is compressed by the surrounding atmosphere and increases in X–ray luminosity. The cluster luminosity thus rises, peaking at about the time when the core gas cools, almost simultaneously, to very low temperatures. Once the gas has cooled, a steady flow is established quite rapidly at the cluster center. The rate at which gas cools subsequently, measured in terms of the amount of matter $\dot{M}$ which is cooling in the unit time, is simply determined by the initial conditions (Fabian, Nulsen & Canizares 1984):

$$\dot{M}(t) \simeq \left.\frac{4\pi r^2 \rho}{dt_{\rm c}/dr}\right|_{t_{\rm c}(r)=t} \tag{3.2}$$

This equation simply states that the gas cools after approximately one cooling time;

it applies because most of the gas remains largely undisturbed until it is about to cool. The steady cooling flow is confined within the region in which t_c is less than the age of the system (taken to be the Hubble time): $t_c < t_a \sim H_0^{-1}$. This *cooling region* is delimited by the so–called *cooling radius* r_c, the radius at which $t_c = t_a$. To understand why the flow takes place, consider the gaseous atmosphere trapped in the gravitational potential well of a cluster to be divided into two parts at the radius r_c. The gas pressure at r_c is determined by the weight of the overlying gas, in which cooling is not important. Within r_c, cooling reduces the gas temperature and the gas density must rise in order to maintain the pressure at r_c. The only way for the density to rise, excluding matter sources within r_c, is for the gas to flow inwards: this is the cooling flow, which is essentially a pressure–driven process. The net result is that the gas within r_c radiates its thermal energy plus the pdV work done on it as it enters the cooling region.

This is the behaviour of an idealized, spherically symmetric, homogeneous cooling flow. In practice, X–ray observations of real cooling flows indicate that they are inhomogeneous and must consist of a mixture of temperatures and densities at each radius (see below). Inhomogeneities in the gas are expected to cause cooled matter to drop out and form cold clouds at different temperatures throughout the flow: the result is that cold matter continues to be slowly deposited over a large volume in the core of the cluster. However, many of the key properties of cooling flows are adequately modelled by a smooth flow, which gives results in fair agreement with a more comprehensive treatment (Thomas, Fabian & Nulsen 1987).

3.2.1 Theory of Smooth Flows

One can consider the central region of a cooling flow as steady and hydrostatic (this assumption is justified as the flow velocities are typically subsonic, see Eq. 3.18 below) and study its structure in more detail. Assuming spherical symmetry, the flow equations are (Fabian, Nulsen & Canizares 1984):

$$\dot{M} = 4\pi \, \rho \, v \, r^2 = cost \tag{3.3}$$

$$\frac{dp}{dr} = -\rho \, \frac{d\phi}{dr} \tag{3.4}$$

$$\rho\, v \frac{d}{dr}\,(H+\phi) = n_{\rm e}^2\,\Lambda\,(T) \tag{3.5}$$

where v, $n_{\rm e}$, p and T are respectively the inward radial velocity, the electron number density, pressure and temperature; Λ is the cooling function (Eq. 1.14), ϕ the gravitational potential and

$$H = \frac{5}{2}\frac{kT}{\mu m_{\rm p}} \tag{3.6}$$

the specific enthalpy.

- If gravity is negligible,

$$\frac{kT}{\mu m_{\rm p}} \gg \frac{GM}{r} = r\,\frac{d\phi}{dr} \tag{3.7}$$

  the pressure is constant (from Eq. 3.4, by excluding the gravitational potential). Eqs. 3.3 and 3.4 then give:

$$\left\{ \begin{array}{lll} 3.3 & \Longrightarrow & \rho\, v \propto r^{-2} \\ 3.4 & \Longrightarrow & n_{\rm e} \propto T^{-1} \end{array} \right.$$

  while Eq. 3.5 can be written in the form:

$$\rho\, v\,\frac{d}{dr}\,(H) = n_{\rm e}^2\,\Lambda\,(T) \tag{3.8}$$

  From Eqs. 3.6 and 3.8 it results:

$$\rho\, v\,\frac{5}{2}\frac{k}{\mu m_{\rm p}}\frac{dT}{dr} = n_{\rm e}^2\,\Lambda(T) \tag{3.9}$$

  Given the behaviour of ρv and $n_{\rm e}$ with r, and Eq. 1.14, one has:

$$r^{-2}\,\frac{dT}{dr} \propto T^{-2}\,T^{\alpha}$$

which integrated gives the solution of hydrodinamic equations:

$$T(r) \propto r^{\frac{3}{3-\alpha}} \tag{3.10}$$

The density varies as:

$$\rho(r) \propto r^{-\frac{3}{3-\alpha}} \tag{3.11}$$

that is $\rho(r) \propto r^{-1.2}$ for thermal bremsstrahlung ($\alpha = 1/2$).

- When gravity is significant,

$$\frac{kT}{\mu m_{\rm p}} \simeq \frac{GM(r)}{r}$$

  the solution of hydrodinamic equations is more complicated. It has been shown (Fabian & Nulsen 1977; Fabian, Nulsen & Canizares 1984) that the temperature solution always approaches a critical solution on which

$$\frac{kT}{\mu m_{\rm p}} = \mathcal{A}\,\frac{GM(r)}{r} \tag{3.12}$$

  where $\mathcal{A}$ is a constant of order unity (see Table 3.1). This behaviour is illustrated in Fig. 3.1. It is worth noticing that, although radiative cooling drives the inflow, the temperature may fall, remain constant or rise depending largely on ϕ. In a steady smooth flow, the flatness of the potential for $r < r_{\rm core}$ results in a constant pressure solution for $r \ll r_{\rm core}$, thus at very small radii the temperature must eventually fall following Eq. 3.10.

This model of a hydrostatic gas contracting due to radiative cooling is very simple and, as a consequence, the crossing time (r/v) is always roughly equal to radiative cooling time throughout a flow, that is:

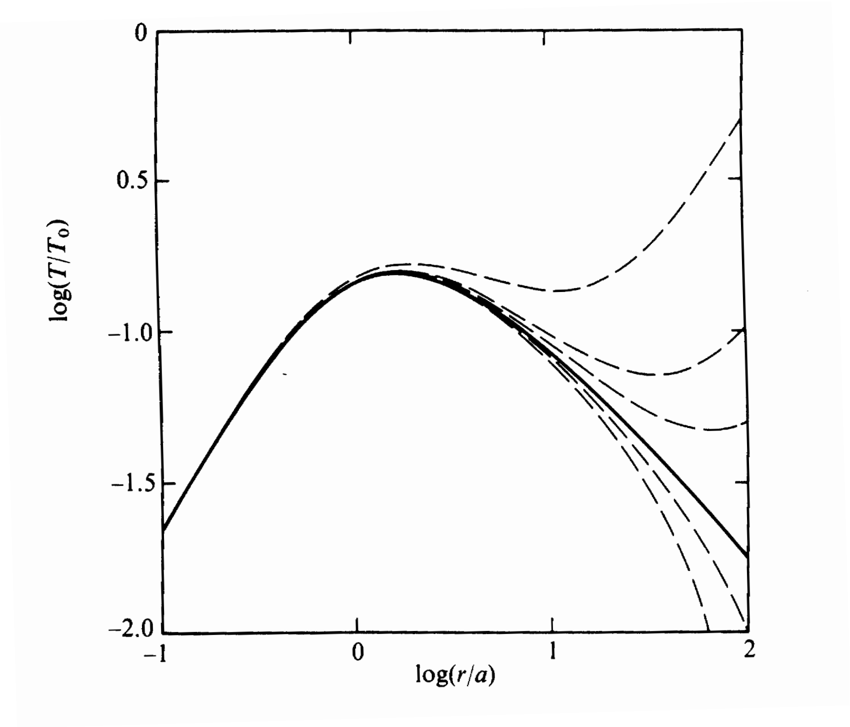

Figure 3.1: Temperature versus radius for a steady cooling flow. The solutions shown are for flows in a gravitational potential $\phi = -\phi_0 \, \frac{a}{r} \, ln \left(\frac{r}{a} + \sqrt{1 + \frac{r^2}{a^2}} \right)$, where a is the core radius (Eq. 1.30). T_0 is defined by $kT_0 = \mu m_p \, \phi_0$. Note that all solutions converge towards the critical solution (solid line) as r decreases. From Fabian, Nulsen & Canizares (1984).

$$\frac{r}{v} = \mathcal{B} \, t_{\rm c} \tag{3.13}$$

where $\mathcal{B} \sim 1$ (see Table 3.1). Given the temperature solutions, and in particular by assuming costant pressure solutions, some other quantities relevant for cooling flows can be calculated directly. From Eqs. 3.8 and 3.6 one has:

$$n_{\rm e}^2 = \frac{\rho \, v}{\Lambda(T)} \frac{dH}{dr} = \frac{\rho v}{\Lambda(T)} \frac{5}{2} \frac{k}{\mu m_{\rm p}} \frac{dT}{dr} \tag{3.14}$$

which can be written in the form:

	$\mathcal{A}$	$\mathcal{B}$
Costant pressure solution	-	$5/(3-\alpha)$
Isothermal potential $M(r) \propto r$	$2/3$	1
Point mass potential $M(r)$ =const	$2/(6-\alpha)$	$(1-\alpha)/3$

Table 3.1: Examples of exact values for $\mathcal{A} = [kT/\mu m_{\rm p}]/[GM(r)/r]$ and $\mathcal{B}$ = flow time/cooling time for some particular cases of cooling flows (Fabian, Nulsen & Canizares 1984).

$$n_e^2 = \frac{\dot{M}}{4\pi\, r^2\, \Lambda(T)} \frac{5}{2} \frac{k}{\mu m_p} \frac{dT}{dr} \tag{3.15}$$

once replaced $\rho\, v = \dot{M}/4\pi r^2$ from Eq. 3.3.

By substituting in Eq. 3.15 the derivative $dT/dr = 3T/(3-\alpha)r$ of Eq. 3.10, one can estimate the electron number density $n_{\rm e}$. In the case of thermal bremsstrahlung ($\alpha = 1/2$), it is:

$$n_{\rm e} \simeq \sqrt{\frac{\dot{M}\, k\, T}{\mu m_{\rm p}} \frac{3}{4\,\pi\, r^3\, \Lambda(T)}} \tag{3.16}$$

From this expression, it is possible to estimate the mean flow velocity. Indeed, from Eq. 3.3 one has $v = \dot{M}/4\pi\, r^2\, \rho$ where $\rho \sim 2n_{\rm e}\, \mu m_{\rm p}$, and thus it results:

$$v \simeq \frac{1}{4} \sqrt{\frac{\dot{M}\, \Lambda(T)}{3\mu m_{\rm p}\, k\, T\, \pi\, r}} \tag{3.17}$$

The isothermal Mach number is:

$$\mathcal{M} = \frac{v}{\sqrt{kT/\mu m_{\rm p}}} \simeq \frac{1}{4kT} \sqrt{\frac{\dot{M}\, \Lambda(T)}{3\pi\, r}} \tag{3.18}$$

which is typically $\ll 1$ (Fabian, Nulsen & Canizares 1984).

3.2.2 X–ray Imaging Evidence for Cooling Flows

The primary evidence for cooling flows comes from X–ray observations. A sharply peaked X–ray surface brightness distribution is indicative of the presence of a cooling flow (Fig. 3.2), because it shows that the gas density is rising steeply towards the center of the cluster. Since the observed surface brightness depends upon the square of the gas density and only weakly on the temperature, the high central density indicates a short cooling time.

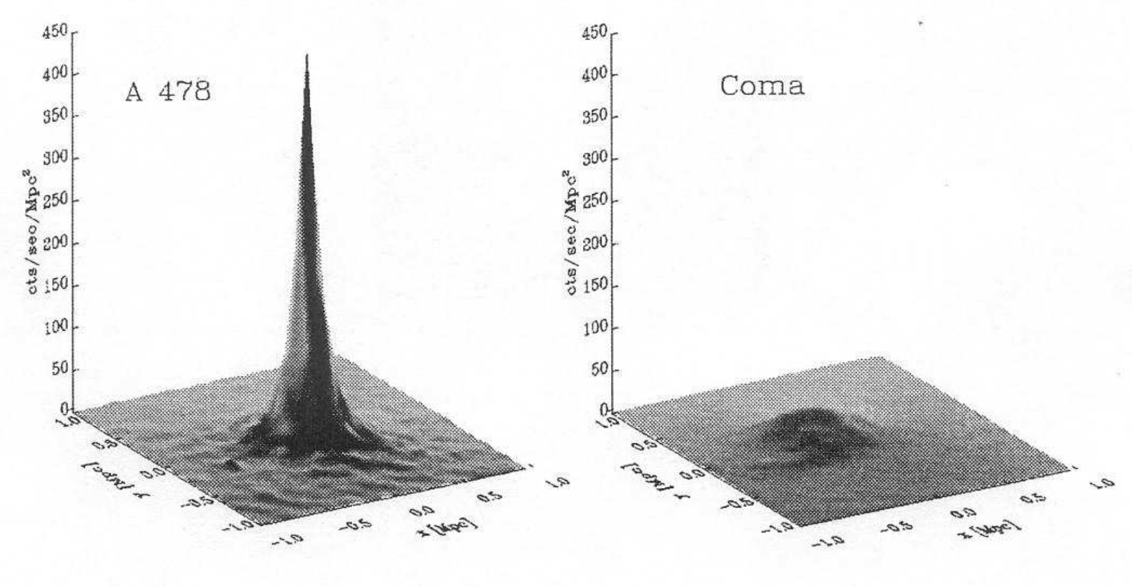

Figure 3.2: A comparison of the X–ray surface brightness profile of a cooling flow cluster, Abell 478 (Allen et al. 1993) and a non–cooling flow cluster, Coma. The clusters have comparable total X–ray luminosities, but the central surface brightness peak in Abell 478 is more than an order of magnitude higher than that in the Coma cluster (the figures have been scaled to simulate the appearance of the systems when viewed at the same redshift). From Allen & Fabian (1997a).

The fraction of clusters with high central surface is large, which means that cooling flows must be both common and long–lived. More than 30% to 50% of the cluster well–detected with the *Einstein Observatory* (Stewart et al. 1984, Arnaud 1988) have surface brightnesses that imply $t_c < H_0^{-1}$ within the central 100 kpc or so; since the $\sim 1'$ angular resolution of the images dilutes the central surface brightness this fraction is certainly an understimate. In particular, Edge, Stewart & Fabian (1992) stress that the characterization of a cluster as a cooling flow depends heavily on the spatial resolution and sensitivity of the instruments used to image the cluster. Additional data from *EXOSAT* (Edge & Stewart 1991a,b; Edge, Stewart & Fabian 1992) and *ROSAT* (Peres et al. 1998) show that more than the 70% of the 55 X–ray brightest clusters in the sky have cooling flows. One of the largest catalogue of clusters with cooling flows is that of White, Jones & Forman (1997), who have analyzed the images of 207 clusters observed with the *Einstein Observatory*. Note that in hierarchical scenarios for the formation of structures in the Universe clusters are assembled from smaller subunits through mergers: this complicates the estimation of the age of a cluster and therefore whether H_0^{-1} should be used for $t_{\rm a}$ is debatable. Hovewer, inspection of the results shows that reducing $t_{\rm a}$ by for example a factor 2 does not much change the fraction of clusters containing cooling flows. The overall picture is that the prime criterion for a cooling flow, $t_{\rm c} < 10^{10}$ yr, is satisfied in a large fraction ($\sim$ 70 - 80%) of clusters (e.g. Fabian 1994).

The "magnitude" of a cooling flow is measured from the amount of matter which cross $r_{\rm c}$ and flows towards the center, that is $\dot{M}$, the *mass inflow rate* or *mass deposition* or *accretion rate* (although this is a poor term since most of the gas does not flow in far from $r_{\rm c}$, see below). The mass deposition rate, due to cooling, can be estimated from the X–ray images by using the luminosity $L_{\rm cool}$ associated with the cooling region and assuming that it is all due to the radiation of the total thermal energy of the gas plus the pdV work done on the gas as it enters $r_{\rm c}$:

$$L = \frac{dE}{dt} \qquad \text{with} \qquad dE = dE_{\rm th} + pdV$$

where

$$\begin{aligned} E_{\rm th} &= \frac{3}{2} N_{\rm tot} kT \quad \Longrightarrow \quad dE_{\rm th} = \frac{3}{2} \frac{dM}{\mu m_{\rm p}} kT \\ pdV &= \frac{\rho\, kT}{\mu m_{\rm p}} dV \quad \Longrightarrow \quad pdV = \frac{dM}{\mu m_{\rm p}} kT \end{aligned}$$

By substituting one obtains the expression for L_{cool}:

$$L_{\mathrm{cool}} = \frac{5}{2}\frac{\dot{M}}{\mu m_{\mathrm{p}}} kT \tag{3.19}$$

where T is the temperature of the gas at r_{c}. L_{cool} ranges from $\sim 10^{42}$ to $> 10^{44}\,\mathrm{erg\,s^{-1}}$ and generally represents $\sim$ 10% of the total cluster luminosity (Fabian 1994). Value of $\dot{M} \sim 100\,\mathrm{M_{\odot}\,yr^{-1}}$ are fairly typical for cluster cooling flows. The main uncertainties in the determination of $\dot{M}$ lie in the gravitational contribution to L_{cool} and the appropriate choice for t_{a}. Assuming $t_{\mathrm{a}} \sim 10^{10}$ yr, the estimates of $\dot{M}$ are probably accurate to within a factor of 2 (Arnaud 1988).

Multi–phase nature of the ICM

From measures of X–ray surface brightness profile of the cluster core (where the X–ray emission is well–resolved) it is possible to derive $L_{\mathrm{cool}}(r)$ which can be turned into $\dot{M}(r)$, the integrated mass deposition rate within radius r. Generally, the surface brightness profiles are less peaked than they would be if all the gas were to flow to the center; this implies that the mass deposition rate is not the same at all radii but is shown to be closely proportional to r (Arnaud 1985):

$$\dot{M}(r) \propto r \tag{3.20}$$

This result has been explained in the context of inhomogeneous models (Nulsen 1986; Thomas, Fabian & Nulsen 1987): in these models the gas is considered to be highly multi–phase, i.e. at each radius different phases, characterized by different temperatures and densities, coexist. The different phases are kept in pressure equilibrium since the sonic timescale, on which pressure waves propagate, is shorter than the cooling timescale. The phases comove with typical velocities substantially smaller than the sound speed. A chaotic magnetic field, which is supposed to be present in the cores of cooling clusters, may help in threading the phases together (Daines, Fabian & Thomas 1994). The same magnetic field is invoked to suppress heat conduction (e.g. Jafelice 1992) which would otherwise rapidly bring the different phases to the same temperature. At temperatures of the order of 10^6 K the cooling timescale becomes shorter than the sonic timescale (Cowie, Fabian & Nulsen 1980) and the gas blobs which reach this temperature can easily drop out of pressure equilibrium with the surrounding gas. As a consequence, the cooler blobs decouple from the flow which continues to move inwards, and thus the cooled material is deposited throughout the central few tens to hundreds of kpc rather than all flowing to the centers of the clusters.

Even though deprojections of X–ray surface brightness profiles show that mass cools and is deposited from the flow in a distributed matter, thus demonstrating the multi–phase nature of the ICM in cooling flows, the single–phase approximation is still widely adopted because of the complexity of the multi–phase theory and lack of data with high spatial resolution.

3.2.3 X–ray Spectral Evidence for Cooling Flows

The second source of evidence for cooling flows comes from X–ray spectroscopy, which demonstrates the presence of a range of temperature and density phases in the central regions of cooling flow clusters. Early observations, made with non–imaging detectors such as the Solid State Spectrometer (SSS) on the *Einstein Observatory*, the Medium Energy array on *EXOSAT* and the Large Area Counter on *GINGA*, showed statistically significant improvements in spectral fits when model components accounting for the expected emission from cooling flows were incorporated.

Since in a cooling flow the gas cools continually from some upper temperature $T_{\rm max}$, the spectrum of the cooling gas is given by the sum of the luminosities of the gas present at all temperatures below $T_{\rm max}$. The amount of gas at each temperature is controlled by how rapidly the gas can cool at each temperature. A volume V of gas cooling at constant pressure from temperature T to $T - dT$ emits a luminosity:

$$dL_{\rm cool} = n_{\rm e}\, n_{\rm p}\, \Lambda(T)\, dV = \frac{5}{2}\frac{\dot{M}}{\mu m_{\rm p}}\, k\, dT \tag{3.21}$$

The luminosity of the spectrum at each frequency is:

$$dL_{\rm cool}(\nu) = n_{\rm e}\, n_{\rm p}\, \Lambda(\nu, T)\, dV \tag{3.22}$$

where $\Lambda(\nu, T)$ is the emission per ion per unit electron density at frequency ν (see Sect. 1.2.2). Substituting for $n_{\rm e} n_{\rm p} dV$ and integrating one obtains:

$$L_{\rm cool}(\nu) = \frac{5}{2} \frac{\dot{M} k}{\mu m_{\rm p}} \int_0^{T_{\rm max}} \frac{\Lambda(\nu, T)}{\Lambda(T)}\, dT \tag{3.23}$$

The cooling spectrum is therefore simply the sum of the emissivities of isothermal plasma models at each temperature inversely weighted by the value of the cooling function at that temperature (e.g. Johnstone et al. 1992). The normalization is set by the mass deposition rate, which is a free parameter in the spectral fitting.

High spectral resolution observations made with the Focal Plane Crystal Spectrometer (FCPS) on the *Einstein Observatory* (Canizares, Markert & Donahue 1988) also indicated the presence of emission lines from gas at temperatures of a few $\times 10^6$ K, again with an emissivity in good agreement with the predictions from the imaging data. These early spectral observations provided strong evidence for the presence of cooling gas in cooling flow cluster, however the data could not firmly constrain the spatial distribution of this material. *ROSAT*, launched in 1990, provided the first opportunity for detailed spatially–resolved spectroscopy of clusters. Observations made with the Position Sensitive Proportional Counter (PSPC) clearly established the presence of material cooler than the ambient cluster temperature, within the cooling radii inferred from the X–ray images (e.g. Allen et al. 1993; Allen & Fabian 1994). The fluxes associated with these cool components were generally in good agreement with the predictions from the imaging data. Observations made with *ASCA* (launched in 1993) have established the multi–phase nature of the central ICM from the spectral data (e.g. Fabian et al. 1994; Fukazawa et al. 1994; Allen et al. 1996).

X–ray Absorption in Cooling Flows

Both the X–ray spectra and imaging data present a consistent picture of inhomogeneous cooling flows in clusters of galaxies. Even so, for some years, the primary uncertainty with the standard inhomogeneous model of cooling flows was the fate of the cooled matter (e.g. Fabian, Nulsen & Canizares 1991). No identification of the large masses of cooled gas, which should presumably be accumulated by the flows over their lifetimes, had indeed been made. However, the study of 21 clusters observed with the *Einstein* SSS by White et al. (1991) showed that large masses of X–ray absorbing material are common in cooling flows. Typical excess column densities of $\sim 10^{21}$ cm^{-2} over the Galactic values were observed. Note that such a column density spread over a typical radius of 100 kpc implies a total mass exceeding $10^{11}M_{\odot}$, assuming solar abundance ratios. Simple considerations of the enormous emission expected if the absorber material were at intermediate temperatures (e.g. 10^2 - 10^7 K) strongly indicates that it is very cold ($T < 10$ K). This work also showed that significant excess absorption is not present in non cooling flow clusters.

Although the *Einstein* SSS data provided convincing evidence for the presence of excess X–ray absorption in cooling flow clusters, they gave little information on the spatial distribution of the absorbing gas. Spatially–resolved X–ray spectroscopy of the massive cooling flow cluster Abell 478 made with *ROSAT* PSPC (Allen et al. 1993) showed that the distribution of intrinsic absorbing material in this system is well–matched to that of the cooling flow. Allen et al. (1993) also demonstrated that the mass of absorbing material was in good agreement with the mass likely to have been accumulated by the cooling flow over its lifetime. A similar study of 2A 0335+096 was made by Irwin & Sarazin (1995). The data thus suggest the X–ray absorbing material as a plausible sink for much of the cooled gas deposited by cooling flows. Subsequent results on the spatial distribution of cooling gas and intrinsic X–ray absorbing material in cluster cooling flows are presented by Allen & Fabian (1997b).

Studies with *ASCA* (e.g. Allen 2000; Allen et al. 2001) have further confirmed the presence of intrinsic absorbing material in cooling flows and showed that reasonably good agreement with the data is found if an absorbed cooling spectrum plus an isothermal spectrum (to represent the outer gas projected along the line of sight) are fitted to the data. The mass deposition rates inferred from these spectral fits were found to be in good agreement with the results inferred from the imaging data. The consistency between estimates of $\dot{M}$ derived from spectral measurements and those derived from analysis of the surface brightness is shown in Fig. 3.3.

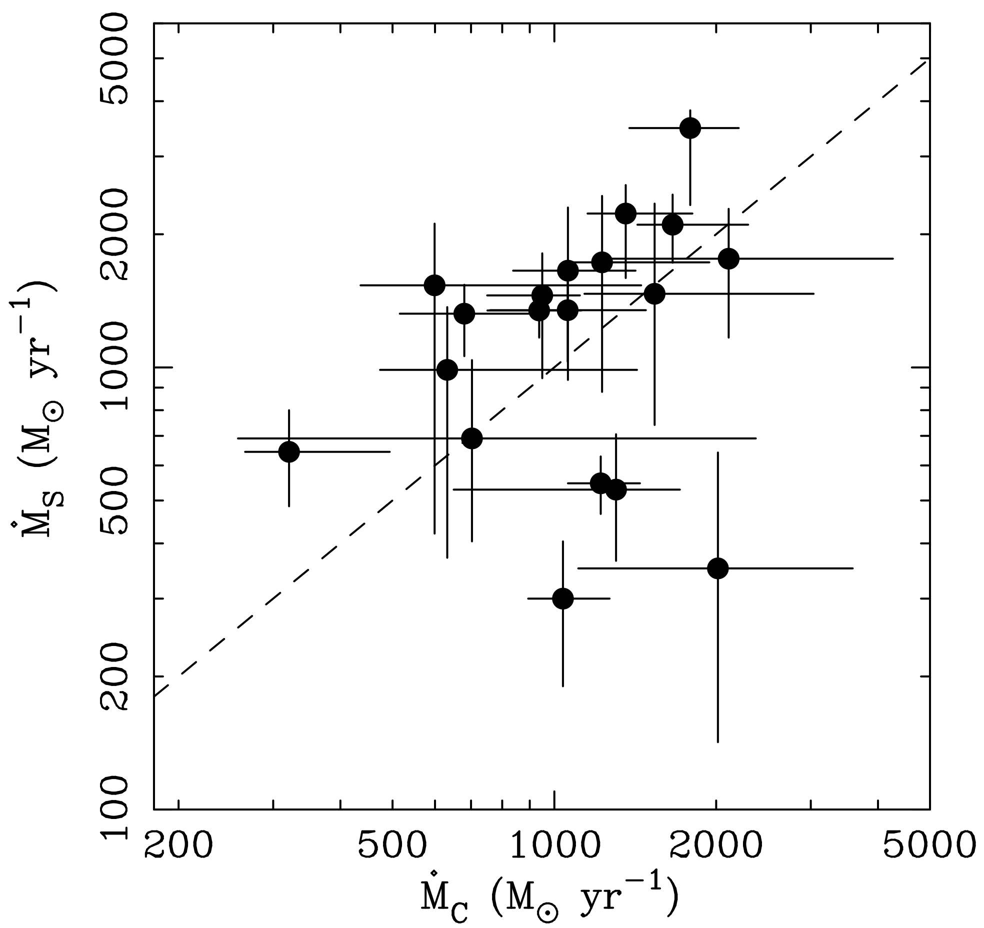

Figure 3.3: The mass deposition rates determined from the *ASCA* spectra ($\dot{M}_S$) versus the values measured from the deprojection analysis of the *ROSAT* imaging data, corrected for the effects of intrinsic absorption ($\dot{M}_C$). The dashed line indicates equality between the values. From Allen (2000).

The spectral estimate uses emission lines and blends as a measure of the rate at which matter is cooling through a given temperature, whereas the estimate from the image is based on the rate with which matter must be cooling given its apparent density and temperature profiles. A general agreement between these two methods gives further support for the existence of cooling flows.

3.2.4 Observations at Other Wavelengths

As we have just discussed, the primary evidence for cooling flows comes from X–ray observations. There is less evidence at other wavelengths, and none of it supports the large mass deposition rates inferred from the X–ray data (e.g. Fabian 1994). Some evidence exists for copious amounts of cooler gas emitting in the UV (Oegerle et al. 2001) and in Hα emission (Heckman et al. 1989; Crawford et al. 1999). In addition, molecular hydrogen has been detected (Jaffe & Bremer 1997; Donahue et al. 2000), and the existence of significant quantities of dust has been inferred from infrared emission (Edge et al. 1999; Irwin, Stil & Bridges 2001; Allen et al. 2001). However, HI absorption measurements have found no evidence for cold condensed clouds (e.g. O'Dea, Payne & Kocevski 1998) and in a review of indications of star formation in cooling flows McNamara (1997) show that the inferred star formation rates are typically only 1 - 10% of the model predicted mass deposition rates (e.g. McNamara & O'Connell 1989, 1993; Crawford et al. 1999). At the same time, even though recent interesting observations of molecular emission lines from CO and indications of warm dust have led to the implications of a large reservoir of cold gas in cooling flows (Wilman et al. 2000; Edge 2001; Edge et al. 1999), the amount of cold molecular material is still a factor ~ 10 below what is predicted by X–ray cooling estimates. These observations provide strong support that mass deposition happens in the more massive cooling flows, but they do not necessarily confirm the very high mass deposition rates inferred for these clusters from X–ray imaging data.

Therefore, the connection between these observations and the X–ray data is still unclear, and the exact quantity and location of cooling flow byproducts is unresolved. Following Peterson et al. (2002b), we refer to this as the *classic cooling flow problem*. This is , perhaps, the crux of the controversial aspect of cooling flows:

it is difficult to prove or disprove their existence with observations in wavebands other than the X–ray. The lack of clear evidence at other wavebands does not make the X–ray evidence any less compelling, though it does challenge more detailed X–ray spectroscopic observations to further test the cooling flow picture (see Sect. 3.4).

3.3 Magnetic Fields in Cooling Flows

It is well established that the ICM is magnetized (see Sect. 1.3.2), with an intracluster field strength and coherence length of roughly $B \sim 1\mu$G and $l_{\mathrm{B}} \lesssim 10$ kpc (e.g. Carilli & Taylor 2002). Magnetic fields have three potentially important effects in cooling flows (e.g. Nulsen 1997). First, in a gas at temperature T, with electron density n_{e} and magnetic field B, the ratio of the Larmor radius to the mean free–path for thermal electrons is:

$$\frac{r_{\mathrm{L}}}{\lambda} \simeq \left(\frac{n_{\mathrm{e}}}{10^{-3}\mathrm{cm}^{-3}}\right)\left(\frac{T}{10^{8}\ \mathrm{K}}\right)^{-3/2}\left(\frac{B}{1\mu\mathrm{G}}\right)^{-1} \tag{3.24}$$

Thus a tiny magnetic field can dramatically suppress cross field thermal conduction (e.g. Sarazin 1986; Rosner & Tucker 1989; Tribble 1989; Pistinner & Shaviv 1996). Due to the complexity of plasma processes, the degree and the physical mechanisms for suppression of thermal conduction remain uncertain. Nevertheless, it seems likely that a highly disordered or tangled field can effectively stop thermal conduction in a cooling flow. Without such suppression, conductive heating can prevent cluster cooling flows. Secondly, a magnetic field can pin density fluctuations to the mean gas flow, thereby facilitating the development of thermal instability (e.g. Nulsen 1986, 1988). The third effect is dynamical. The the ratio of the magnetic pressure to the gas pressure is roughly:

$$\frac{P_{\mathrm{B}}}{P} \simeq 1.5 \times 10^{-3}\left(\frac{B}{1\mu\mathrm{G}}\right)^{2}\left(\frac{n_{\mathrm{e}}}{10^{-3}\mathrm{cm}^{-3}}\right)^{-1}\left(\frac{T}{10^{8}\ \mathrm{K}}\right)^{-1} \tag{3.25}$$

implying that, for typical intracluster field strengths, the field is too weak to affect the dynamics of the outer parts of clusters. However, although cluster magnetic fields may be generally weak, they are enormously amplified by the compression and inflow in cooling flows (e.g. Soker & Sarazin 1990; Godon, Soker & White 1998). In the inner regions of cooling flows, the magnetic field should then be dynamically important. If amplified by compressed inflowing gas, the strong magnetic fields in the centers of cluster cooling flows may serve as further indirect evidence for the presence of inflow. In order to use the strong magnetic fields as an indication for inflow, is it crucial to understand its behaviour in the center of cooling flow clusters.

3.3.1 Models for Magnetic Field Amplification

Radial Field

The simplest model for the behaviour of the magnetic field in cooling flow clusters assumes that the magnetic field is frozen–in to the cooling gas, that the inward cooling flow is homogeneous, and that there is no mass drop–out from the flow (Soker & Sarazin 1990). Under these assumptions, the radial component of the magnetic field goes as $B_{\rm r} \propto r^{-2}$ while the transverse components varies as $B_{\rm t} \propto (rv)^{-1}$, where r is the radius and v the inflow velocity.

This model predicts that the magnetic pressure varies as:

$$P_{\rm B} \approx \frac{P_{\rm Bc}}{3}\left[\left(\frac{r}{r_{\rm c}}\right)^{-4} + 2\left(\frac{r}{r_{\rm c}}\right)^{-2}\left(\frac{v}{v_{\rm c}}\right)^{-2}\right] \tag{3.26}$$

where $v_{\rm c}$ and $B_{\rm c}$ are the inflow velocity and the magnetic field at the cooling radius $r_{\rm c}$, respectively. Combining Eqs. 3.25 and 3.26, one has that the magnetic field reaches equipartition with the thermal pressure at a radius:

$$r_{\rm B} \approx 10\left(\frac{B_{\rm c}}{1\mu{\rm G}}\right)^{1/2}\left(\frac{n_{\rm c}}{3\times10^{-3}\ {\rm cm}^{-3}}\right)^{-1/4}\left(\frac{T_{\rm c}}{7\times10^{7}\ {\rm K}}\right)^{-1/4}\ {\rm kpc} \tag{3.27}$$

Given the relatively simple correspondence between the cooling radius and the total cooling inflow rate $\dot{M}_{\rm c}$ (which comes from the assumption that at $r_{\rm c}$ the cooling time and the inflow time are both equal to the age of the system $\sim 10^{10}$ yr), i.e.:

$$r_{\rm c} \approx 90 \left(\frac{\dot{M}_{\rm c}}{100\ {\rm M}_\odot\ {\rm yr}^{-1}}\right)^{1/3} \left(\frac{n_{\rm c}}{3\times 10^{-3}\ {\rm cm}^{-3}}\right)^{-1/3}\ {\rm kpc} \tag{3.28}$$

the radius at which the magnetic pressure equals the gas pressure can be written as:

$$r_{\rm B} \approx 9 \left(\frac{B_{\rm c}}{1\mu{\rm G}}\right)^{1/2} \left(\frac{n_{\rm c}}{3\times 10^{-3}\ {\rm cm}^{-3}}\right)^{-7/12} \left(\frac{T_{\rm c}}{7\times 10^{7}\ {\rm K}}\right)^{-1/4} \left(\frac{\dot{M}_{\rm c}}{100\ {\rm M}_\odot\ {\rm yr}^{-1}}\right)^{1/3}\ {\rm kpc} \tag{3.29}$$

The other main prediction of this model is that the Faraday rotation measure RM (see Sect. 1.3.2) should increase rapidly toward the center:

$$\begin{aligned} RM \ \approx\ & 4000 \left(\frac{n_{\rm c}}{3\times 10^{-3}\,{\rm cm}^{-3}}\right)^{2/3} \left(\frac{l_{\rm Bc}}{10\,{\rm kpc}}\right)^{1/2} \\ & \times \left(\frac{\dot{M}_{\rm c}}{100\,M_\odot\,{\rm yr}^{-1}}\right)^{1/2} \left(\frac{T_{\rm c}}{7\times 10^{7}\,{\rm K}}\right)^{1/2} {\rm rad\,m}^{-2}\,, \end{aligned} \tag{3.30}$$

where $l_{\rm Bc}$ is the magnetic coherence length at the cooling radius, which in the inner regions of the cooling flow is still expected to be about 10 kpc. Numerical simulations in 2-D cylindrical symmetry performed by Christodoulou & Sarazin (1996) confirm the basic results of Soker & Sarazin (1990).

Isotropic Field

Obviously, the model for radial field can not be realistic for the entire cooling flow region since it does not consider the back reaction of the field on the flow and the fate of the magnetic field. The decreasing of the transverse coherence length $l_{\rm t} \propto r$, leading to a field that is predominantly radial, and the increase in the magnetic pressure will result in strong transverse magnetic pressure gradients and a possibly outcome is turbulent motion which will isotropize the magnetic field.

An isotropized magnetic field model is discussed by Tribble (1993) in the contest of turbulent cooling flow. In fact, cooling flows are turbulent (Heckman et al. 1989;

Loewenstein & Fabian 1990), and this turbulence is in part due to the multi–phase nature of the gas, with denser gas blobs falling in and stirring the rest of the gas. The turbulence in the inner region will stir the gas, stretching and possibly amplifying the magnetic field. Tribble (1993) pointed out that this turbulence stirring will also isotropize the magnetic field, indeed the turbulent velocities are much greater than the mean inflow velocity, which is of order 10 km s^{-1}, so characterization of the flow as smooth and steady (used in Soker & Sarazin's model) is incorrect. Rather, an individual element of gas in the flow is in constant motion relative to the mean flow and its shape and orientation are constantly changing, while its mean position falls slowly inwards on a 10^{10}–yr time scale. The overall effect is isotropic compression of the field. As the gas cools further, the magnetic field becomes stronger and eventually becomes both dynamically and energetically important (Tribble 1991). Assuming that the magnetic field is frozen into the flow and isotropized, the variation of field B with gas density ρ within the central cooling region is:

$$B \propto \rho^{2/3} \tag{3.31}$$

3.3.2 Observations

The central galaxy in a cluster cooling flow is usually a radio galaxy, and these radio sources have been used to search for Faraday rotation (see Sect. 1.3.2). In all cases observed so far, the central radio sources in cluster cooling flows have either very large Faraday rotations or depolarization. Examples of radio sources with rotation measures of $\sim 10^3$ - 2×10^4 rad m^{-2} include M87/Virgo (Owen, Eilek & Keel 1990), Cygnus A (Dreher, Carilli & Perley 1987), Hydra A (Taylor & Perley 1993), 3C295 (Perley & Taylor 1991), Abell 1795, Abell 2199, Abell 2052 (Ge 1991; Ge & Owen 1993), Abell 2029, and Abell 4059 (Taylor, Barton & Ge 1994). A number of cases have also been found of amorphous radio sources at the centers of cooling flows which are highly depolarized, e.g. PKS 0745-191 (Baum & O'Dea 1991), and 2A 0335+096 (Sarazin, Baum & O'Dea 1995).

From a survey of Faraday rotations, Ge (1991) concluded that all sources in the centers of strong cooling flows have high RM ($\gtrsim 1000$ rad m^{-2}), and that all other

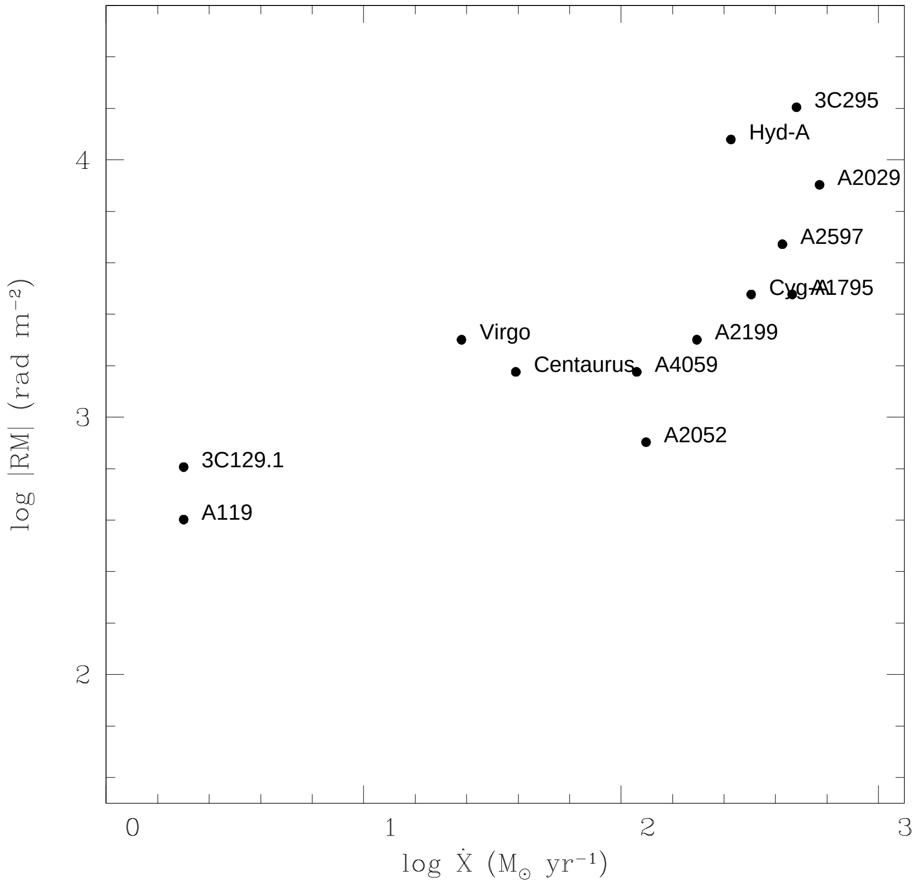

Figure 3.4: The maximum absolute RM plotted as a function of the estimated cooling flow rate, called here $\dot{X}$, for a sample of X–ray luminous clusters with measured RMs. Both RM and $\dot{X}$ are expected to depend on density to a positive power, so in that sense the correlation is expected. From Carilli & Taylor (2002).

sources (in the centers of clusters without cooling flows and in the outer regions of clusters with cooling flows) have much smaller RMs ($\lesssim 100$ rad m^{-2}). Hence, current data are consistent with all radio galaxies at the center of cooling flow clusters having extreme RMs, with the magnitude of the RMs roughly proportional to the cooling flow rate (Carilli & Taylor 2002, see Fig. 3.4). This is consistent with the RM being created in a cooling flow (e.g. Soker & Sarazin 1990). If the RM occurs in the ambient medium (see Rudnick & Blundell 2003 for an opposite interpretation of the rotation as local to the source), then the RMs can be used to study the strength and geometry of the magnetic field in the cooling flow. The observed RMs of $\sim 10^3$

- 10^4 rad m^{-2} are consistent with $B \sim 10$ - 50 μG over scales of kpc to tens of kpc (e.g. Carilli & Taylor 2002).

These observations confirm the prediction that the magnetic fields in cooling flows are strong. Since the amplification of the field is due to compression and inflow, the large rotation measures provide indirect evidence that gas is indeed flowing into the center. The implied field strengths in the inner regions give magnetic pressures which are comparable to the very high gas pressures and thus it is likely that magnetic fields affect the dynamics of the gas in these regions.

One important question is the ultimate fate of the magnetic flux which is advected into cooling flows. If the flux were not removed by some process, the field would grow to very large values. The magnetic fields might be convected out of the cluster center, or might be reduced by field line reconnection. Physical arguments and initial numerical simulations suggest that reconnection is more important in cooling flows (Soker & Sarazin 1990; Christodoulou & Sarazin 1996).

3.4 New Insights from *Chandra* and *XMM*

As seen in Sect. 3.2, the bulk of the thermal energy of the cooling ICM is thought to radiate at X–ray wavelengths, and thus studying the X–ray spectrum is critical to understand cooling flows and test cooling flow models. As previously stated, if the plasma cools homogeneously the density profile of the cores of clusters should be much steeper than observed (e.g. Johnstone et al. 1992), which has led to the conclusion that the cooling plasma must condense locally into smaller clouds distributed over a large volume, i.e. in a multi–phase medium. However, even ignoring the details of the resulting spatial distribution, simple thermodynamic arguments show that the X–ray spectrum of such a cooling flow can be robustly predicted by integrating the spectral luminosity from the different temperature phases, fixed by the mass flow rate (Eq. 3.23). Given an isothermal outer cluster temperature and a set of assumed abundances, the isobaric multi–phase model yields a unique spectral signature. This is shown in the top panel of Fig. 3.5 for a maximum temperature of 8 keV and for 1/3 solar abundances: the model predicts detectable emission lines from the complete range of Fe L charge states, as well as from He–like and H–like charge states of N, O, Ne and Mg.

Data acquired by the Reflection Grating Spectrometer (RGS) on *XMM–Newton* enable this robust spectral prediction to be quantitatively tested for the first time. Surprisingly, the observed spectra reveal a remarkable systematic deficit of emission at the lowest temperatures (Peterson et al. 2001; Tamura et al. 2001a; Kaastra et al. 2001; Tamura et al. 2001b; Xu et al. 2002; Sakelliou et al. 2002). This result has been confirmed through medium resolution spatially–resolved spectroscopy using the *XMM–Newton* European Photon Imaging Cameras (EPIC) and *Chandra* ACIS observations, where spectral fits have yielded significantly smaller $\dot{M}$ than expected (David et al. 2001; Böhringer et al. 2001; Molendi & Pizzolato 2001; Schmidt, Allen & Fabian 2001; Ettori et al. 2002; Johnstone et al. 2002). Following Peterson et al. (2002b), we refer to the observed deficit of the predicted soft X–ray emission as the *soft X–ray cooling flow problem.*

3.4.1 Spectroscopic Evidence for the Absence of Low Temperature Phases

Recent results from *XMM–Newton* (Jansen et al. 2001) observations have provided unpreceded detailed spectroscopic diagnostics of the central regions of clusters providing new insights into the structure of cooling core regions. Making use of *XMM* RGS, den Herder et al. (2001) show, for several cooling core regions, spectral signatures of different temperature phases ranging approximately from the hot virial temperature of the cluster to a lower limiting temperature, $T_{\rm low}$, which is still significantly above the "drop out" temperature where the gas would stop to emit significant X–ray radiation. That is, the clearly observable spectroscopic features of the lower temperature gas, expected by a cooling flow model, are not observed. In the case of the massive cooling flow cluster Abell 1835 with a bulk temperature of about 8.3 keV no lines or features for temperature phases below 2.7 keV are found (Peterson et al. 2001, see Fig.3.5). Similar results have been derived for the cluster Abell 1795 (Tamura et al. 2001a). This is in clear conflit with the standard cooling flow model.

These results coming from the *XMM* RGS data are confirmed by *XMM–*

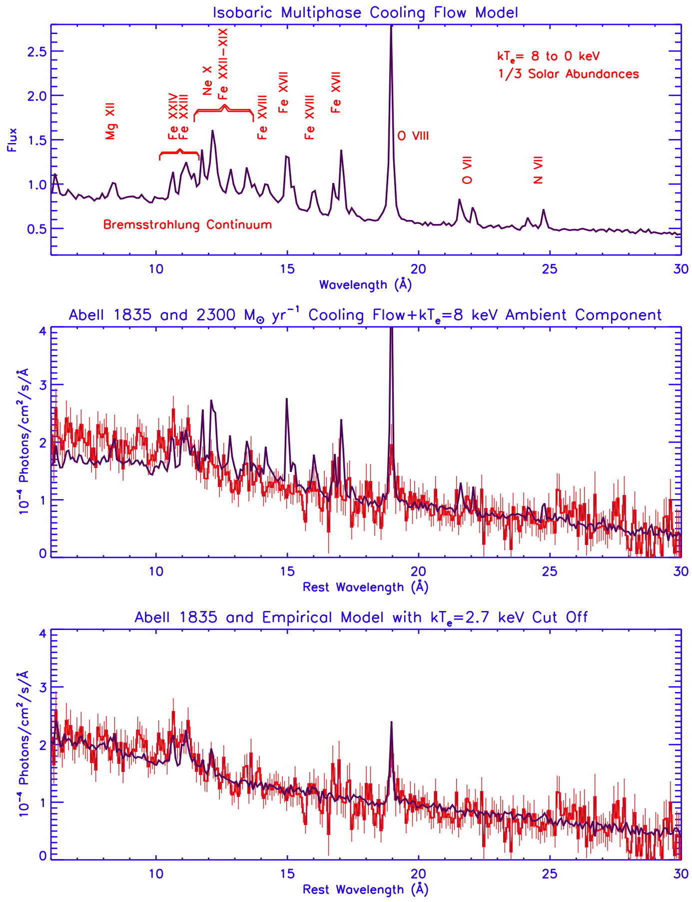

Figure 3.5: The first panel show the prediction for the isobaric cooling flow model. The comparison of this model with the spectrum of Abell 1835 is shown in the second panel. As can be seen, the fit is reasonable for the higher ionization Fe L lines (Fe XXIV and Fe XXIII), but the model vastly overpredicts the emission line intensities for the lower charge states, especially Fe XVII. The final panel shows an empirical parameterization, where the isobaric model temperature distribution has been arbitrarily truncated at temperatures below $kT = 2.7$ keV. This model has no clear physical motivation, but it does provide a good fit to the data. From Peterson et al. (2002a).

Newton observations with the energy sensitive imaging devices, EPN (Strüder et al. 2001) and EMOS (Turner et al. 2001). The spectral fitting of the X–ray emission in the cooling flow clusters M87, Abell 1795, Abell 496, and Abell 1835 showed that single temperature models provided a better representation of the data than cooling flow models (Böhringer et al. 2002, Molendi & Pizzolato 2001) also implying the lack of low temperature components. In a recent, very detailed analysis of the temperature structure of the closest and best studied cooling flow in M87, Matsushita et al. (2002) have shown that the temperature structure is well described locally by a single temperature over most of the cooling core region. In particular the spectral features originating from gas below a temperature of 0.8 - 1 keV, predicted by the standard cooling flow model through Eq. 3.23, are not detected.

Recently, Peterson et al. (2002b) presented high resolution X–ray spectra of 14 cooling flow clusters, spanning a large range of temperatures and mass deposition rates, obtained with *XMM* RGS. Various spectra exhibit line emission from O VIII, Ne X, Mg XII & XI, Al XIII & XII, Si XIV & XIII, N VII, and C VI as well as all Fe L ions. Among the spectroscopic signatures which are sensitive to the temperature of the hot plasma in the temperature range relevant to cooling flows, the complex of iron L-shell lines is the most important and provides the primary method for determining the temperature distribution. The spectra exhibit strong emission from cool plasma at just below the ambient temperature of the ICM outside the cooling region, $T_{\rm max}$, down to $T_{\rm max}/2$, but also exhibit a severe deficit of emission with respect to relative to the predictions of the isobaric cooling flow model at lower temperatures ($< T_{\rm max}/3$). In addition, the best–resolved spectra show emission throughout the entire X–ray temperature range, but they show that there is increasingly less emission at lower temperatures than the cooling flow model would predict. Empirically, the differential luminosity distribution appears to be roughly consistent with the expression:

$$\frac{dL}{dT} = \frac{5}{2}\frac{\dot{M}k}{\mu m_{\rm p}}\,(a+1)\left(\frac{T}{T_{\rm max}}\right)^{a} \tag{3.32}$$

where $a \approx 1$ - 2. Therefore the differential luminosity distribution is consistent with being proportional to the temperature to the power of ≈ 1 - 2, instead of being independent of the temperature, as expected in the standard multi–phase model (Peterson et al. 2002b).

3.4.2 Refining the Standard Picture: Suggestions

For the sake of completeness, here we briefly summarize the various explanations proposed for the observed disagreement with simple cooling flow expectations. They can be divided into mechanisms which modify the isobaric cooling flow model, but involve no real modification of the general paradigm of radiatively driven flows in gravitationally–relaxed cluster cores, and mechanisms which lead to substantial modifications of the general cooling flow process by inclusion of additional heating mechanisms or non X–ray cooling channels.

Modifications to the standard spectral prescriptions

Two recent explanations of the soft X–ray cooling flow have been proposed that involve no real modification of the multi–phase model (3.19). First, Peterson et al. (2001) suggested that differential absorption by colder material could absorb more of the emission from cold ions. This, however, is somewhat implausible, since one would expect hot and cold parcels of plasma to have roughly equal probability of being obscured. An explanation offered by Fabian et al. (2001) and developed in Morris & Fabian (2003) involves a locally non–uniform distribution of metals in the ICM, which modifies the spectrum significantly. This requires that the metal abundance variations occur on scales smaller than cooling parcels of plasma, and that the variations sample a particular bimodal distribution. If metallicity variations were the relevant explanation, one would expect that the measured line strengths, which depend on the mass fraction of the metal–rich gas, should draw away from the standard cooling flow expectation near roughly a common temperature ~ 1 keV, where line cooling dominates over bremsstrahlung for super–solar abundances. However, this is not observed and this model is therefore not compatible with Peterson et al. (2002b)'s results.

Modifications to radiatively–driven flows

A variety of additional physical processes have been proposed to operate in the cores of clusters, which could, in principle, account for the soft X–ray cooling flow problem (Peterson et al. 2001; Fabian et al. 2001; Böhringer et al. 2002;

Sasaki & Yamasaki 2002; Brighenti & Mathews 2002; Peterson et al. 2002b and references therein). Models for external heat sources include:

Time-dependent heating by AGN outflows — These kind of models have been considered by a variety of authors (e.g. Rosner & Tucker 1989; Tabor & Binney 1993; David et al. 2001). Buoyant bubbles carrying relativistic plasma appear to be a common phenomena in clusters with central AGNs. The thermal energy seems to be enough to heat cooling flows through cosmic ray interactions and mechanical heating, but it is unclear whether this energy gets properly channeled into the cooling volume (e.g. Fabian et al. 2001). In addition, since the gas does not appear to accumulate at $T_{\rm low}$ but rather it appears to cool down to that temperature then vanish, these models must be made self–regulating to counterbalance cooling at a rate proportional to the mass deposition rate, and with periods of heating roughly as long as periods of cooling. Clearly, it requires a significant degree of fine–tuning.

Electron thermal conduction from the outer regions of clusters — There is considerable thermal energy in the outer regions of clusters that can destroy any existing cooling flow through electron thermal conduction (e.g. Tucker & Rosner 1983; Stewart et al. 1984; Bertschinger & Meiksin 1986; Voigt et al. 2002; Ruszkowski & Begelman 2002; Zakamska & Narayan 2003). The critical question is to what level is conduction suppressed by tangled magnetic fields (Chandran & Cowley 1998; Narayan & Medvedev 2001). Voigt et al. (2002), Zakamska & Narayan (2003) and Fabian, Voigt & Morris (2002) have demonstrated that the heat flow from the outer regions of clusters with a small suppression ($> 10^{-1}$) in the Spitzer conductivity would appear to cancel radiative losses in many clusters. The spatial distribution of the heating and overall energetic requirements appear to be satisfied by conduction models, but there is no explanation for why the cluster would cool to their current temperature distribution (conduction should indeed suppress temperature gradients by definition).

Continual sub–cluster mergers — Markevitch et al. (2000) showed that clusters previously thought to be fully relaxed exhibit temperature fronts consistent

with plasma exhibiting large bulk motions in the gravitational potential. This provides another source of energy that has not been dissipated and therefore leads to an increase of the cooling time above previous estimates (Gomez et al. 2002), so that the time scales for radiative cooling and dynamical relaxation may be similar. However, there is no reason for this process to be self–regulating, and one would expect a much larger difference in the temperature distributions, depending on each cluster merger history.
Models for rapid cooling mechanisms include:

UV cloud interfaces — Begelman & Fabian (1990) and Fabian et al. (2001) discussed the possibility that hot electrons are cooled conductively by interfaces with cold clouds. This leads to emission in the UV where the cooling function is the highest, and is consistent energetically with the large observed Hα luminosities (Heckman et al. 1989; Crawford et al. 1999) of 10^{42} - $10^{44}\,\mathrm{erg\,s^{-1}}$ in cooling flows. However, by itself, this model does not explain the observed temperature distribution in the soft X–ray band, since high temperature electrons are cooled by this process as well.

Dust mixing — Some clusters have been established as strong IR sources, typically of order 10^{43} - $10^{45}\,\mathrm{erg\,s^{-1}}$ (Edge et al. 1999). Fabian et al. (2002b) demonstrated that in all systems studied, the missing soft X–ray luminosity is more than accounted for by the IR luminosity. Hot electrons sputtering on dust grains could collisionally heat the grains and this in turn cools the hot electrons. The cooling function for this process has been discussed in Burke & Silk (1974) and Draine & Salpeter (1979) and is 100 times larger than the X–ray cooling function for a typical ISM composition of dust grains. As such, this explanation appears promising, but there is no strong temperature dependence to either the X–ray or dust cooling function that would systematically reduce the overall level of soft X–ray emission.

Relativistic particles and Alfvén waves — MHD turbulence present in the ICM and amplified by the compression of magnetic fields in cooling flow regions may allow for considerable energy to be released via Alfvén waves or mildly relativistic particles. This problem could concern the research carried out in this thesis and will be discussed later (see Chapter 5). In particular, a step forward in this PhD work would be that of calculating the turbulence–induced heating of the ICM and studying whether it could be efficient in balancing the cooling (see Chapter 7).

3.4.3 The Emerging Picture and Future Work

The central 100 kpc radius region in most clusters has a radiative cooling time shorter than 5 Gyr (Peres et al. 1998) and many have cooling times which drop to the center to a value of only 10^8 yr or so. At the same time, the gas temperature is observed to drop by a factor of 3 or more over this radius range. It is plausible that the temperature drop and short radiative cooling times are related, and that the low temperatures are caused by radiative cooling. Although this indicates that cooling flows are taking place, *XMM–Newton* spectra show no evidence for strong mass cooling rates of gas below 1 - 2 keV (the data are consistent with modest levels of cooling: $\dot{M}$ of tens rather than hundreds $\mathrm{M}_{\odot}\,\mathrm{yr}^{-1}$). It is then a puzzle as to why gas which has lost two thirds of its thermal energy, and for which the radiative cooling time is very short, is not seen to cool further.

There are two obvious solutions, both of which have some difficulties (Fabian 2002). The first solution is that the gas does cool but either the soft X–ray emission is absorbed or the cooling is non–radiative and due, say, to mixing. The problem of the fate of cooled gas then remains, although significant masses of cold gas have been found in some objects. The second solution is that some heating balances cooling. The problem here is that the heat has to balance cooling over a wide range of radii and a wide range of timescales.

Implicit in the discussion of proposed solutions is that only one mechanism explains the observations. Since many of the above ideas are energetically viable, this may be unlikely. It may be that the soft X–ray cooling flow problem and the classic cooling flow problem are solved by different solutions (Peterson et al. 2002b). It may also be possible that a combination of processes could have different effects, resulting in a more efficient method than each mechanism does individually (e.g. Ruszkowski & Begelman 2002 for heating model). However, we notice that since the different mechanisms proposed depend on the physical conditions of the cluster, which may likely be different from cluster to cluster, a very surprising fine–tuning would be required for the overall response to be similar in all the cluster population, as observed.

Clearly, the model for the multi–phase distribution is inadequate. More detailed comparisons between observations at X–ray and other wavelengths may more carefully address which of the physical mechanisms are important energetically. Much more theoretical work is needed in addressing why any of the proposed mechanisms would dynamically conspire to produce the observed temperature distribution. These descriptions, however, are just beginning to be developed and it remains a theoretical challenge either to cool keV plasma with little resulting soft X–ray radiation, or to balance radiative cooling both energetically and dynamically.

As seen in Sect. 1.3, the presence of cooling flows in clusters of galaxies is anticorrelated with that of extended diffuse radio emission. However, some cooling flow clusters host diffuse radio emission with extension smaller than that of radio halos: these radio sources are called *mini–halos*. The possible connection between cooling flows and radio mini–halos is the main topic of this PhD work and will be discussed in Chapter 4.

Chapter 4

Model for the Origin of Radio Mini–Halos

4.1 Introduction

In spite of the observed anti–correlation between the presence of cooling flows and extended radio emission in clusters of galaxies, there are a few cooling flow clusters where the relativistic particles can be traced out quite far, forming what is called a "*mini–halo*" (e.g. Perseus: Burns et al. 1992; Abell 2390: Bacchi et al. 2003)

Mini–halos are diffuse radio sources, extended on a small scale (up to ~ 500 kpc), surrounding a dominant radio galaxy at the cluster center. In the literature, because of the presence of the central radio galaxy, these sources have been considered of different nature from that of extended halos and relics, and the problem of their origin has never been investigated in detail. Here, we point out that mini–halos do not appear as extended lobes maintained by an Active Galactic Nucleus (AGN), as in classical radio galaxies (Giovannini & Feretti 2002), therefore their radio emission is indicative of the presence of diffuse relativistic particles and magnetic fields in the ICM. The age of the radio–emitting electrons injected at a given time in the intense fields present in cooling flow regions (see Sect. 3.3) is of the order of $\sim 10^7$ - 10^8 yr, much shorter than any reasonable transport time over $\sim$ hundred kpc scales, so that the diffuse radio emission from mini–halos suggests the presence of reaccelerated electrons.

In this sense we consider mini–halos similar to halos: their origin may be due to the reacceleration of a relic population of previously injected relativistic electrons (see Sect. 2.3 for models for radio halo formation). However, unlike the case of halos, the source of the necessary energy for the reacceleration can not be supplied by mergers, since observations in general show no mergers acting in clusters with cooling flows.

Here we argue that the necessary energetics to reaccelerate the relativistic electrons responsible for the diffuse radio emission is supplied by cooling flows, thus supporting a direct connection between cooling flows and radio mini–halos.

In this Chapter we will investigate the reacceleration of relativistic electrons in cooling flows and present a model for radio mini–halos. The application of this model to two observed mini–halos will be presented in Chapter 5.

4.2 General Picture of the Model

Before discussing the detailed physics of the model for electron reacceleration in cooling flows and origin of radio mini–halos, we will briefly describe its general picture.

The main assumption is that a relic population of relativistic electrons is present in the cooling flow region, and that it can be efficiently reaccelerated by magnetohydrodynamic (MHD) turbulence amplified by the compression of the magnetic field in the cooling flow region.

Population of Relativistic Electrons

As an initial condition, we assume the presence in the cluster volume of a relic population of relativistic electrons previously injected. It should be stressed that we do not investigate the ultimate origin of the seed population of relativistic electrons: obvious and promising candidates are normal radio galaxies at the cluster center, so a consistent picture could be that relativistic electrons originated in a central active galaxy and then were spread throughout the whole cooling flow region by diffusion in few Gyr. On the other hand, it may also be that relativistic electrons are present in the whole cluster volume as a remnant of an earlier acceleration due for example to a past merger event, and then they are carried by the cooling flow towards the center where the magnetic field strength strongly increases. As it will be shown in the following (see Sect. 4.3.2), in both cases a reacceleration is needed in order to observe a persistent diffuse radio emission from these relativistic electrons.

MHD Turbulence

The other condition we assume is the presence in the cluster volume of a seed large–scale turbulence, naturally present in the ICM for example as a result of past merger events or motion of the galaxies in the cluster, or due to the interaction of the radio lobes of the central galaxy with the cooling flow itself. This turbulence will be amplified in the cooling flow region; however, a too energetic turbulence would cause the disruption of the cooling flow, as indeed happens in the radio halo scenario. Therefore, we suggest a picture in which the physical conditions of the ICM in a cooling flow cluster with a radio mini–halo are intermediate between those which lead to the formation of extended radio halos, hosted by clusters without cooling flows, and those holding in cooling flow clusters without radio halos. The energetics of the turbulence plays the main part in discriminating between these two opposite situations. A turbulence with a high enough energy density will be efficient at reaccelerating the relativistic electrons: depending on the characteristic scale of the turbulence, which is proportional to the reacceleration time, these electrons are able to produce a diffuse synchrotron emission either in the form of an extended radio halo or a mini–halo. On the contrary, if the energy density of the turbulence is too low, there will be no efficient reacceleration of the electrons and consequently no diffuse radio emission, independently of the turbulence scale.

The model for the origin of mini–halos in cooling flow clusters thus requires the presence of some turbulence to reaccelerate the relic electrons that produce the diffuse radio emission, but at the same time the turbulence must not be too high in order to avoid the disruption of the cooling flow: this fine–tuning of the turbulent energy could explain, at least qualitatively, the rarity of these radio sources.

Concerning the values of the turbulent scale which could be expected, in the general teory of turbulent plasma one can calculate the wavelength which carries most of the turbulent energy in a spectrum of Alfvén waves (e.g. Tsytovich 1972). When applied to the case of ICM, with standard values of the physical parameters, it gives results of the order of tens to hundreds kpc (see Sect. 5.2.2).

The Cooling Flow Problem

High resolution X–ray studies with *XMM–Newton* have recently shown that the soft X–ray spectra of several cooling flow clusters of galaxies are inconsistent with standard cooling flow models, as the gas cools down to about 2 - 3 KeV but not to lower temperatures (see Sect. 3.4). How to reconcile cooling flow models with these observations is still a matter of debate (see Sect. 3.4.2), but it should be stressed that the compression of the thermal plasma and of the magnetic field within the cooling region is well ascertained. As a consequence, even if the cooling flow is stopped somewhere close to the central galaxy, the basic results of our model remain unchanged: once the turbulence has been energized by the flow, it takes a time of order of several $\times 10^8$ yr for it to be dissipated. During this time, turbulence continues to reaccelerate the electrons and determines the radio properties of the mini–halo.

4.3 Magnetic fields and Relativistic Electrons in Cooling Flows

In order to develop a model for the origin of radio mini–halos, the first step is to study the behaviour of magnetic fields and relativistic electrons in cooling flows. Since the cooling radius $r_{\rm c}$ sets the relevant scale in a cooling flow region, we will state all quantities as a function of $x = r/r_{\rm c}$, where r is the distance from the center, and we will indicate with the subscript 'c' their value at $r_{\rm c}$.

In what follows, we consider the idealized hypothesis of a homogeneous, single–phase, spherically symmetric cooling flow, with no mass drop–out from the flow. In these conditions the theory of smooth flows presented in Sect. 3.2.1 is valid. In particular, we consider thermal bremsstrahlung models ($\alpha = 1/2$ in Eq. 1.14): in this case, the decrease of the temperature with distance is $T(x) \propto x^{1.2}$ and the gas density increases towards the center with the same behaviour (see Eq. 3.11). For convenience, we assume that $n_{\rm e} \sim n_{\rm p} = n$, thus the gas pressure is $p \sim 2nkT$ and the gas density is $\rho \sim n m_{\rm p}$ (see Sect. 1.2.1).

4.3.1 Magnetic Field Amplification

As seen in Sect. 3.3, the compression of the thermal gas in the cooling flow region is expected to produce a significant increase of the strength of the frozen–in cluster magnetic field. Depending on the physical conditions prevailing in a cooling flow, in particular on the relative values of the turbulent velocity $v_{\rm T}$ and of the mean inflow velocity $v_{\rm F}$, two possibilities arise:

- if $v_{\rm T} \ll v_{\rm F}$, the inward cooling flow is homogeneous and the turbulence does not distort the field geometry during the infall. In this case we can follow Soker & Sarazin's model (1990). They have presented numerical solutions showing that the frozen–in magnetic field is greatly increased by the compression of the ICM and its lines become predominantly radial as the gas flows inwards. Under the assumption that the field is not dynamically important, the magnetic pressure depends on $v_{\rm F}/v_{\rm F,c}$ (Eq. 3.26). From Eqs. 3.17 and 1.14 one finds that $v_{\rm F} \propto T^{-1/4} r^{-1/2}$ and thus, given the solution of hydrodynamic equations (Eq. 3.10), $v_{\rm F} \propto r^{-4/5}$. When substituted in Eq. 3.26 one has that:

$$B(x) = \frac{B_{\rm c}}{\sqrt{3}}\, x^{-2} \left(1 + 2x^{\frac{18}{5}}\right)^{\frac{1}{2}} \sim x^{-2} \tag{4.1}$$

- if $v_{\rm T} \gg v_{\rm F}$, as pointed out by Tribble (1993), an individual element of gas in the flow is in constant motion relative to the mean flow and its mean position falls slowly inwards. Turbulence greatly affects the field geometry, and the overall result is an isotropic compression of the field. In this case the variation of the field with the gas density n within the central cooling region is (see Eq. 3.31) $B \propto n^{2/3}$, so that being $n(x) \propto x^{-1.2}$, it results:

$$B(x) = B_{\rm c}\, x^{-0.8} \tag{4.2}$$

The resulting intensity profile of the magnetic field in these two different cases is plotted in Fig. 4.1. In both cases the field strength increases towards the center, but with quite different behaviours. In Soker & Sarazin's model the field strength grows faster than in Tribble's one and in the central region it reaches values which are at

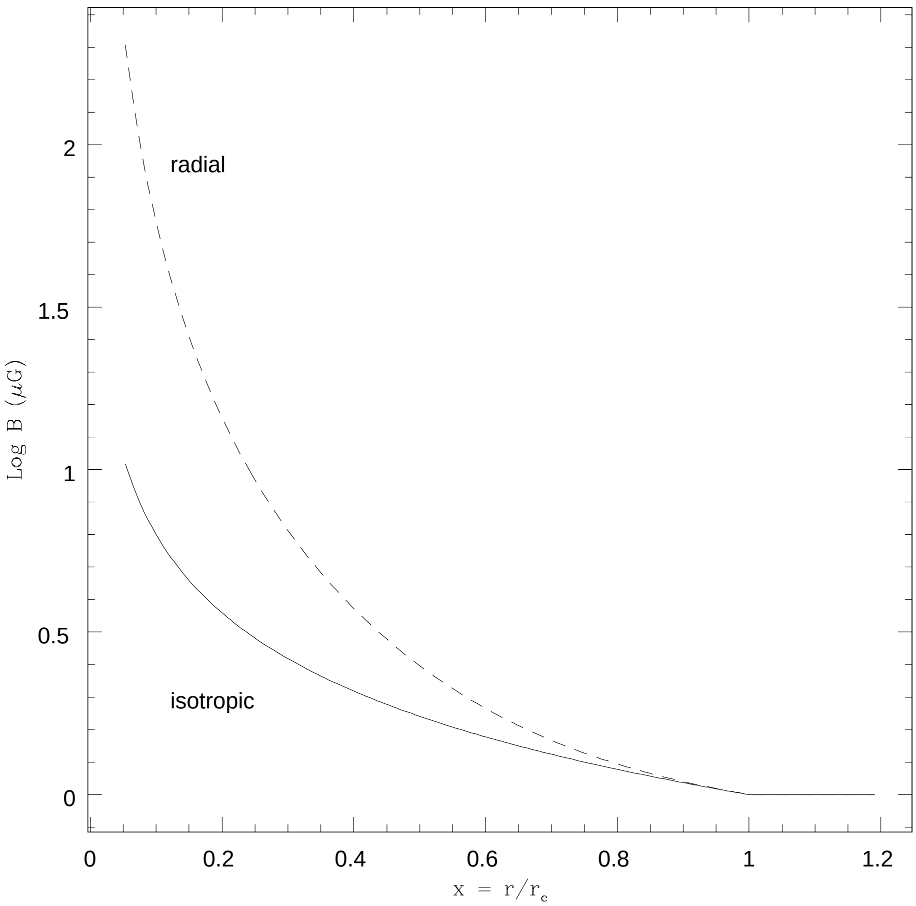

Figure 4.1: The calculated field increase in the cooling flow region for Soker & Sarazin's model (radial field, dashed line) and Tribble's model (isotropic field, solid line). We have assumed $B_c = 1\,\mu$G.

least one order of magnitude larger than those reached by the isotropic compression model. It should be mentioned that, in agreement with the predictions of these models, intense fields of the order of some tens of μG have been derived by detections of extremely high Faraday rotation measures throughout radio galaxies in the center of cooling flow clusters (see Sect. 3.3.2). Such high values of the magnetic field have important consequences on the evolution of the energy and spectrum of relativistic electrons in the cooling flow region.

4.3.2 Need for Reacceleration

The radiative lifetime $\tau = -\gamma/\dot{\gamma}$ of an ensemble of relativistic electrons losing energy via synchrotron emission and IC scattering off the cosmic microwave background photons (CMB) is given by:

$$\tau_{\sin+\mathrm{IC}} \approx 1.64 \times 10^{13} \left[\left(\frac{B}{1\mu\mathrm{G}} \right)^2 \sin^2\vartheta + \frac{2}{3} \left(\frac{B_{\mathrm{CMB}}}{1\mu\mathrm{G}} \right)^2 \right]^{-1} \gamma^{-1} \quad \mathrm{yr} \tag{4.3}$$

where γ is the Lorentz factor, ϑ is the pitch angle of the emitting electrons and $B_{\mathrm{CMB}} = 3.18(1+z)^2$ μG denotes the magnitude of the magnetic field equivalent to the CMB from the standpoint of the losses. Without any reacceleration mechanism at work, with the strong fields present in the cooling flow region ($B \sim$ few $\times 10\mu$G) the emission of the relativistic electrons in the radio band ($\gamma \sim 10^4$) should not be observable for more than $\sim 10^7$ yr. This short lifetime contrasts with the diffuse radio emission observed in mini–halos, and whatever the model for the origin and presence of the relativistic electrons in the mini–halo region is, the more plausible explanation is that relativistic electrons are reaccelerated.

To see this, let us consider the two hypothesis for the origin of the seed population of relativistic electrons presented in Sect. 4.2. The hypothesis that the radio–emitting region is filled with electrons carried by the cooling flow can not account for the persistent emission observed from mini–halos, since the characteristic lifetime of radio–emitting electrons is shorter than the cooling time. On the other hand, if one assumes that the central AGN plays an important role in the injection of the relativistic electrons, it should be noticed that it is difficult to find a direct connection between the central radio galaxy and the mini–halo in terms of simple particle diffusion or buoyancy. Indeed, the idea of diffuse radio emission as due to buoyant old radio lobes should be ruled out since the expansion and buoyancy of blobs would produce severe adiabatic losses which further reduce the lifetime of relativistic electrons. At the same time, the diffusion of relativistic electrons out of the central galaxy can not explain the extension of the observed radio emission either, since their radiative lifetime is shorter than the crossing time (both assuming the Alfvén velocity or the diffusion time as in Sarazin 2002, see Eq. 2.30). In the time needed for the relativistic electrons to diffuse to scales > 100 kpc, one expects to end up with a steep power–law energy distribution of the relic population with a break at $\gamma_b < 10^3$: such a population would produce no detectable radio synchrotron emission. Another way to see this is to calculate the typical diffusion length of the electrons as a function of γ. One estimates that the radio emitting electrons can not diffuse for more than about 30 kpc (e.g. Brunetti 2002). This contrasts with the diffuse radio emission observed in mini–halos up to scales $\sim$ 200 kpc, hence it seems plausible that the electrons have been reaccelerated.

In addition, a reaccelerated relic electron population in cluster radio halos would naturally produce radio synchrotron spectra which steepen with increasing distance from the center (Brunetti et al. 2001b), as observed in a few radio halos. Here we stress that the presence of a similar progressive steepening of the spectral index with increasing distance has been also found in the well studied radio mini–halo of the Perseus cluster (Sijbring 1993), the only one for which good multifrequency radio data were available. This provides an additional indication for the presence of an effective mechanism for electron reacceleration operating in the ICM in the cooling flow region.

4.4 Electron Reacceleration in Cooling Flows

In our model we assume that the relativistic electrons are continuosly reaccelerated by stochastic *Fermi type* mechanisms (Fermi–II). As discussed in Sect. 2.2.3, given an initial monoenergetic electron distribution these processes act as to produce both a *systematic* acceleration of the electrons with an efficiency α_2, and a *random* change of their energy with an efficiency α_1. These two combined effects result in a relatively wide distribution of the energy of the electrons around a mean value determined by systematic processes. In particular, it is well known that MHD turbulence can efficiently accelerate electrons via Fermi–like processes (e.g. Melrose 1980). In order to allow relativistic electrons to still be emitting in the radio band, the reacceleration mechanism has to act with an efficiency comparable to the energy loss processes.

4.4.1 Competing Mechanisms at Work

The time evolution $d\gamma/dt$ of the energy of a relativistic electron is determined by the competing processes of loss and reacceleration (both related to the magnetic field, obtained either from Eq. 4.1 or 4.2), and it is important to study the efficiency of these processes in the cooling flow region as a function of x:

$$\frac{d\gamma(x)}{dt} = -\beta(x) \cdot \gamma^2(x) + \alpha_2(x) \cdot \gamma(x) - \chi(x) \tag{4.4}$$

where $\beta(x)$ is the coefficient of synchrotron and IC losses, $\alpha_2(x)$ the reacceleration coefficient and $\chi(x)$ the Coulomb losses term. The Coulomb losses depend on the ICM density as (e.g. Sarazin 1999):

$$\begin{aligned} \chi(x) &= 1.2 \times 10^{-12} n(x) \left(1 + \frac{\ln\left(\frac{\gamma}{n(x)}\right)}{75}\right) \quad \mathrm{s}^{-1} \\ &\sim 1.4 \times 10^{-12} n(x) \quad \mathrm{s}^{-1} \end{aligned} \tag{4.5}$$

where $n(x) = n_c x^{-1.2}$. The coefficient of the radiative losses is:

$$\beta(\vartheta, x) = 1.9 \times 10^{-9} \left[B^2(x) \sin^2 \vartheta + \frac{2}{3} B^2_{\mathrm{CMB}}\right] \quad \mathrm{s}^{-1} \tag{4.6}$$

where ϑ is the pitch angle. If the pitch angle scattering is an efficient process, then the electrons will be continuosly isotropized and by averaging over angles one obtains $\langle B^2 \sin^2 \vartheta \rangle = 2/3 B^2$, so Eq. 4.6 can be written in the form:

$$\beta(x) \sim 1.3 \times 10^{-21} \left[\left(\frac{B(x)}{1\mu\mathrm{G}}\right)^2 + 10\right] \quad \mathrm{s}^{-1} \tag{4.7}$$

where in substituting the value of B_{CMB} we have neglected the dependence on the redshift, not important in our model.

According to the usual Fermi acceleration theory (see Sect. 2.2.3), it is $\alpha_2 = 2\alpha_1$ and the coefficient of systematic Fermi acceleration due to MHD turbulence is given by:

$$\alpha_2(x) \approx \frac{\pi\, v_{\rm A}^2(x)}{l(x)\, c} \left(\frac{\delta B(x)}{B(x)}\right)^2 \tag{4.8}$$

where $v_{\rm A}(x) = \sqrt{B(x)^2/4\pi\rho(x)} \sim 2.2 \times 10^{11}\, n_{\rm c}^{-0.5}\, x^{0.6}\, B(x) \quad {\rm cm\ s^{-1}}$ is the Alfvén velocity, and $l(x)$ is the characteristic distance between two subsequent peaks of MHD turbulence.

We assume the existence of an energetic turbulence such that $\delta B(x)/B(x) \sim 1$ constant through the whole cooling flow region. It is worth noticing that MHD turbulence can efficiently accelerate electrons via Fermi–like processes only if an additional efficient pitch–angle scattering process, which isotropizes the electron momenta, is at work (see Sect. 2.2.3). An efficient process may be resonant interaction with Alfvén waves, which requires that the electron velocity parallel to the magnetic field is $v_{\|} > (m_{\rm p}/(m_{\rm e}\mu))^{1/2} \times v_{\rm A}$, where $v_{\|} = v\mu$ (Eilek & Hughes 1991; Hamilton & Petrosian 1992). The fact that in our model we deal with a seed population of relativistic electrons guarantees the efficiency of this process.

Under the simple assumption that the total number of turbulent elements is conserved during the infall, $l(x)$ is roughly proportional to $n(x)^{-\frac{1}{3}}$, so that $l(x) = l_{\rm c}\, x^{0.4}$. The underlying assumption is that the turbulence does not decay on a time scale shorter than the acceleration time scale.

With these hypothesis, the reacceleration of relativistic electrons by MHD turbulence via Fermi-like processes acts on a time scale given by:

$$\tau_{\rm acc}(x) = \alpha_2(x)^{-1} \sim 1.9 \times 10^7 \left(\frac{l_{\rm c}}{1{\rm pc}}\right) \left(\frac{n_{\rm c}}{10^{-3}{\rm cm}^{-3}}\right) \left(\frac{B(x)}{1\mu{\rm G}}\right)^{-2} x^{-0.8} \quad {\rm yr} \tag{4.9}$$

In Fig. 4.2 we report $d\gamma/dt$ due to the above processes as a function of γ. It is clear that the different processes dominate in different energy regions, with the Coulomb losses being especially important at low energies. In addition, due to its dependence

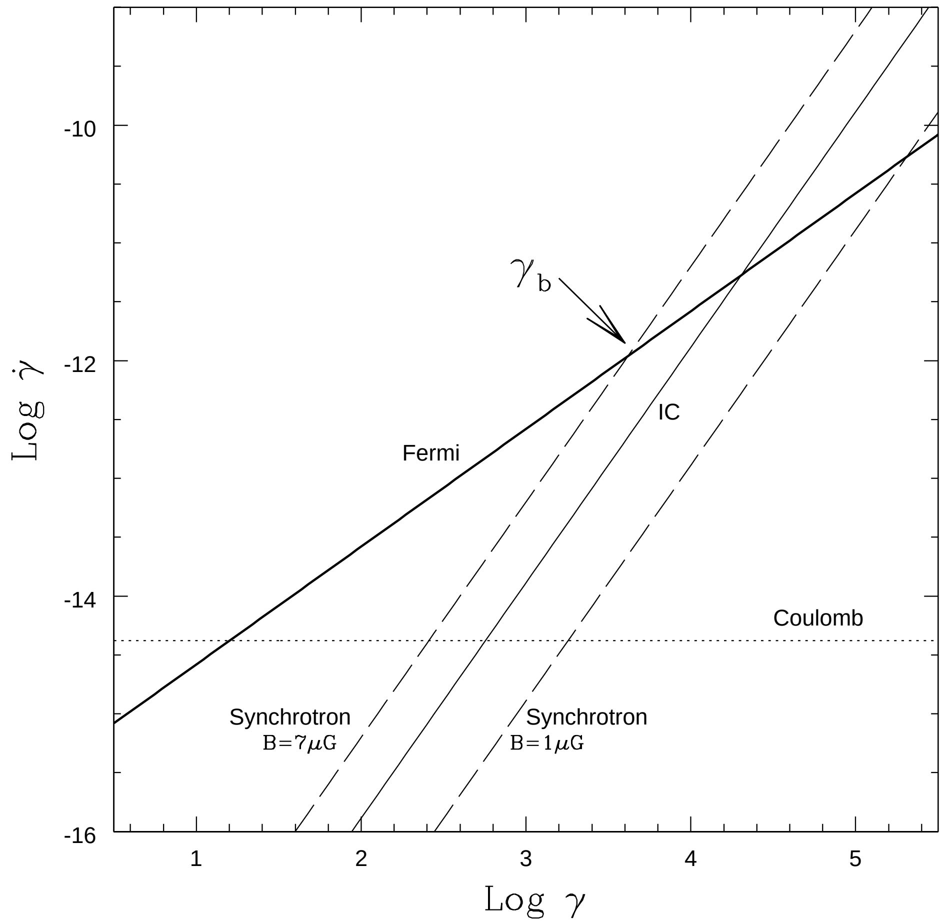

Figure 4.2: $\dot{\gamma} = d\gamma/dt$ is plotted for the processes in Eqs. 4.5, 4.7 and 4.8 as a function of γ. The value of γ_b is shown for synchrotron losses with $B = 7\mu$G.

on the energy ($\propto \gamma$), the Fermi–like reacceleration can be an efficient process in a restricted energy band, whereas Coulomb and radiative losses respectively prevent, in general, electron reacceleration at lower and higher energies.

4.4.2 The Break Energy

Since the characteristic time of radiative losses is proportional to γ^{-1} (Eq. 4.3), while that of Fermi acceleration is independent of γ (Eq. 4.9), the losses dominate the time evolution of the electrons for energies higher than γ_b, the *break energy* (see

Fig.4.2). We will now derive the expression for $\gamma_{\rm b}(x)$ from Eq. 4.4. In the following calculation, for simplicity of notation, we omit the dependence of the coefficients on the adimensional distance x from the cluster center. The evolution of γ with time is obtained by solving the following integration:

$$\int_{\gamma(t=0)}^{\gamma(t)} \frac{d\gamma'}{-\beta\gamma'^2+\alpha_2\gamma'-\chi} = \int_0^t dt' \tag{4.10}$$

It is convenient to define $q=\alpha_2^2-4\beta\chi$, which expresses the importance of the reacceleration. The general solution of the left side of Eq. 4.10 for $q>0$ (i.e. for reaccelerations more efficient than losses) is:

$$\int \frac{d\gamma}{-\beta\gamma^2+\alpha_2\gamma-\chi} = \frac{1}{\sqrt{q}}\ln\left(\frac{\alpha_2-2\beta\gamma-\sqrt{q}}{\alpha_2-2\beta\gamma+\sqrt{q}}\right) \tag{4.11}$$

so that by integrating Eq. 4.10 one obtains:

$$\gamma(t)=\frac{\alpha_2}{2\beta}+\frac{\sqrt{q}}{2\beta}\left(\frac{\alpha_2-2\beta\gamma_0-\sqrt{q}}{\alpha_2-2\beta\gamma_0+\sqrt{q}}e^{\sqrt{q}t}+1\right)\left(\frac{\alpha_2-2\beta\gamma_0-\sqrt{q}}{\alpha_2-2\beta\gamma_0+\sqrt{q}}e^{\sqrt{q}t}-1\right)^{-1} \tag{4.12}$$

The break energy $\gamma_{\rm b}(t)$ corresponds to the energy at the time t of the electrons having a near infinite energy γ_0 at the initial time $t=0$, thus is obtained by calculating Eq. 4.12 in the limit $\gamma_0\to\infty$. It results:

$$\gamma_{\rm b}(t)=\frac{\alpha_2}{2\beta}+\frac{\sqrt{q}}{2\beta}\cdot\frac{e^{\sqrt{q}t}+1}{e^{\sqrt{q}t}-1} \tag{4.13}$$

which can be written in terms of hyperbolic functions as (e.g. Brunetti et al. 2001b):

$$\gamma_{\rm b}(t)=\frac{1}{2\beta}\left(\alpha_2+\frac{\sqrt{{\alpha_2}^2-4\beta\chi}}{\tanh\left(\frac{t}{2}\sqrt{{\alpha_2}^2-4\beta\chi}\right)}\right) \tag{4.14}$$

Since the reacceleration time scale (Eq. 4.9) is much shorter than the time it takes for a volume element to be convected by the flow from r_c into the center, we can assume the condition of stationarity. The break energy of the stationary spectrum, which corresponds to the energy at which the losses are balanced by the reacceleration, is obtained by evaluating Eq. 4.14 in the limit $t \to \infty$, resulting:

$$\gamma_{\rm b} = \frac{1}{2\beta}\left(\alpha_2 + \sqrt{{\alpha_2}^2 - 4\beta\chi}\right) \tag{4.15}$$

where α_2, β and χ are taken from Eqs. 4.8, 4.7 and 4.5, respectively.

Because of the distance dependence of the coefficients, the break energy in the electron spectrum is not the same throughout the whole cooling flow region, but it (weakly) depends on the radial distance. The evolution of $\gamma_{\rm b}$ inside the cooling flow region is represented by the bold line in Fig. 4.3, where, for comparison, we have also plotted $\gamma_{\rm b}(x)$ as obtained with two other coefficients α_+ of reacceleration. It is worth noticing that the reacceleration due to MHD turbulence is able to make $\gamma_{\rm b}$ weakly increasing inside the cooling flow region and thus it has the correct radial dependence on the parameters to naturally balance the radial behaviour of the radiative losses.

4.4.3 The Electron Energy Spectrum

According to Kardashev (1962), the time evolution of the electron energy distribution in terms of Lorentz factor, $N(\gamma, t)$, is obtained by solving the continuity equation (see Sect. 2.2.1):

$$\frac{\partial N(\gamma,t)}{\partial t} = \alpha_1(t)\,\frac{\partial}{\partial\gamma}\left[\gamma^2\frac{\partial N(\gamma,t)}{\partial\gamma}\right] + \frac{\partial}{\partial\gamma}\left\{\left[-\alpha_2(t)\gamma + \beta(t)\gamma^2 + \chi(t)\right]N(\gamma,t)\right\} \tag{4.16}$$

where the term containing $\alpha_1(t)$ takes into account random acceleration by the Fermi mechanism, the term containing $\alpha_2(t)$ takes into account systematic acceleration by the Fermi mechanism, the term containing $\beta(t)$ takes into account synchrotron and IC losses of relativistic electrons, and the term containing $\chi(t)$ takes into account Coulomb losses. Under stationary conditions, $\partial N(\gamma,t)/\partial t = 0$ and Eq.4.16 becomes:

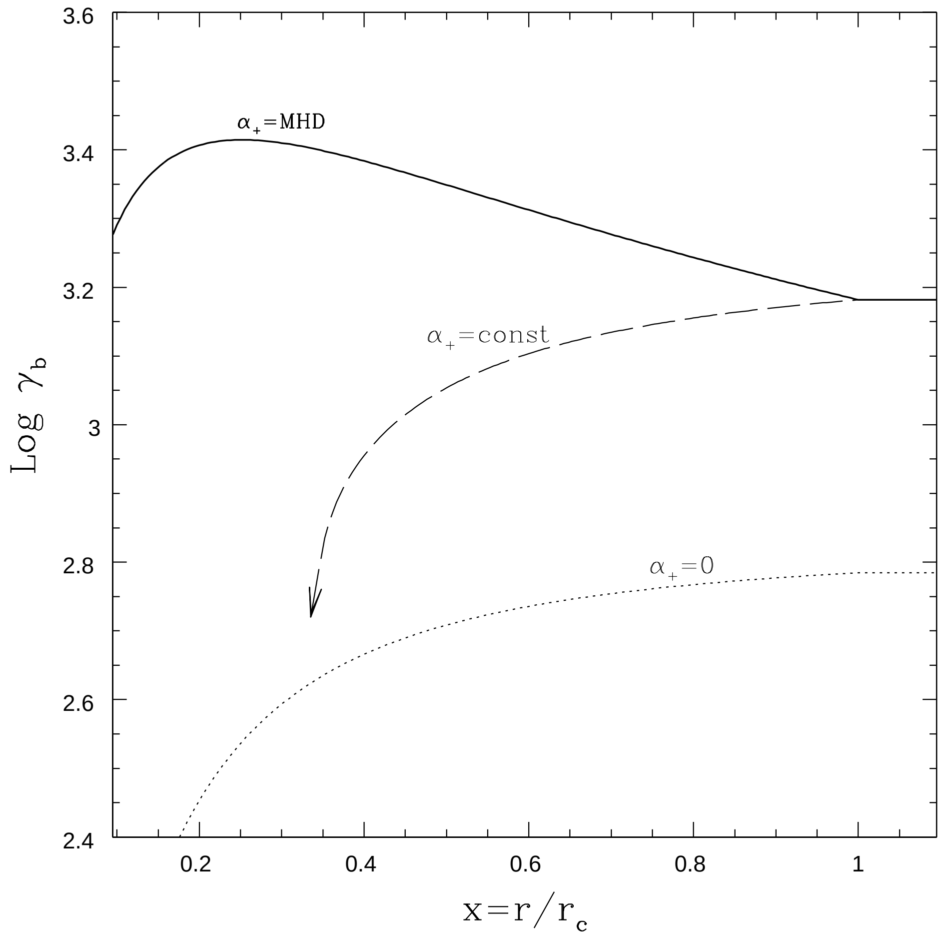

Figure 4.3: Evolution of γ_b inside the cooling flow region for three different cases of reacceleration (see Eq. 4.15 with α_2 replaced by the generic α_+): • α_+ given by Fermi–like processes related to the MHD turbulence in the cooling flow (bold line); • α_+=const (dashed line); • α_+=0, assuming $\Delta t \sim 4 \times 10^9$ yr from injection (dotted line).

$$\frac{d}{d\gamma}\left[\alpha_1\gamma^2\frac{dN(\gamma)}{d\gamma} - \alpha_2\gamma N(\gamma) + \beta\gamma^2 N(\gamma) + \chi N(\gamma)\right] = 0 \tag{4.17}$$

$$\alpha_1\gamma^2\frac{dN(\gamma)}{d\gamma} + \left(\beta\gamma^2 - \alpha_2\gamma + \chi\right) N(\gamma) = \text{ const} \tag{4.18}$$

The value of the constant appearing in Eq. 4.18 is determined by the consistency requirement that in a physical system $N(E) = 0$ in both limits $E = (\gamma-1)m_e c^2 \to 0$ and $E \to \infty$, leading to const $= 0$. Since the coefficient α_2 of systematic Fermi acceleration is twice that of random Fermi acceleration, Eq. 4.18 becomes:

$$\frac{1}{2}\alpha_2\gamma^2\frac{dN(\gamma)}{d\gamma} + \left(\beta\gamma^2 - \alpha_2\gamma + \chi\right) N(\gamma) = 0 \tag{4.19}$$

The general solution of this differential equation is in the form:

$$N(\gamma) = \exp\left[-\int \frac{2(\beta\gamma^2 - \alpha_2\gamma + \chi)}{\alpha_2\gamma^2} d\gamma\right] \tag{4.20}$$

which integrated gives the expression for the spectral distribution of the electrons:

$$N(\gamma) = N(\gamma_\mathrm{b})\gamma_\mathrm{b}^{-2} \exp\left(\frac{2\beta\gamma_\mathrm{b}}{\alpha_2} - \frac{2\chi}{\alpha_2\gamma_\mathrm{b}}\right)\gamma^2 \exp\left(\frac{2\chi}{\alpha_2\gamma} - \frac{2\beta\gamma}{\alpha_2}\right) \tag{4.21}$$

where we have arbitrarily set γ_b as the lower limit of the integration. Eq. 4.21 can be also written in terms of γ/γ_b. From Eq. 4.15, one can set:

$$\left(\frac{2\chi}{\alpha_2\gamma} - \frac{2\beta\gamma}{\alpha_2}\right) = \frac{\frac{2\chi}{\beta\gamma_\mathrm{b}{}^2} - 2\left(\frac{\gamma}{\gamma_\mathrm{b}}\right)^2}{\left(1+\frac{\chi}{\beta\gamma_\mathrm{b}{}^2}\right)\left(\frac{\gamma}{\gamma_\mathrm{b}}\right)} \equiv f\left(\frac{\gamma}{\gamma_\mathrm{b}}\right) \tag{4.22}$$

$$\left(\frac{2\chi}{\alpha_2\gamma_\mathrm{b}} - \frac{2\beta\gamma_\mathrm{b}}{\alpha_2}\right) = 2 - \frac{4}{1+\frac{\chi}{\beta\gamma_\mathrm{b}{}^2}} \equiv \Phi \tag{4.23}$$

so that Eq. 4.21 can be written in the form:

$$N(\gamma) = N(\gamma_\mathrm{b})\exp(-\Phi)\cdot\left(\frac{\gamma}{\gamma_\mathrm{b}}\right)^2 \exp\left[f\left(\frac{\gamma}{\gamma_\mathrm{b}}\right)\right] \tag{4.24}$$

where $N(\gamma_\mathrm{b})$ is the number density (per γ unit) of electrons at γ_b.

Note that the spectral distribution of the electrons $N(\gamma)$ (Eq. 4.24) depends on γ/γ_b only, while the values of the coefficients simply produce a "normalisation" of the spectrum which depends on the radial distance. Indeed, in the limit $\chi/(\beta\gamma_\mathrm{b}^2) \ll 1$

and $\chi/(\beta\gamma_{\rm b}^2) \ll (\gamma/\gamma_{\rm b})^2$, which is valid in our case, Eq. 4.24 can be approximated as:

$$N(\gamma) \propto \left(\frac{\gamma}{\gamma_{\rm b}}\right)^2 \exp\left(-2\gamma/\gamma_{\rm b}\right) \tag{4.25}$$

in agreement with the result of Borovsky and Eilek's (1986), that indeed have not considered the Coulomb losses.

Energetics

In principle, in order to correctly derive the energy density of the relativistic electrons as a function of x one should solve the spatial diffusion equation for the relativistic electrons starting from some initial distribution of the number density and spectrum of the electrons which, however, are basically unknown. As a consequence, we prefer to parameterize the electron energy density $\mathcal{E}(x)$ as:

$$\mathcal{E}(x) = \int_0^\infty N(E)\, E\, dE \;\propto\; x^{-s} \tag{4.26}$$

or equivalently:

$$\mathcal{E}(x) = m_{\rm e}c^2 \int_1^\infty N(\gamma)\,(\gamma-1)\, d\gamma \;\propto\; x^{-s} \tag{4.27}$$

where s is a free parameter which will be constrained and discussed in the application of the model to particular mini–halos (see Chapter 5).

Given Eq. 4.25 (written in terms of the energy E), the integral in Eq. 4.26 is in the form $\int_0^\infty y^n\, {\rm e}^{-ay}\, dy$ which has the analytic solution $\Gamma(n+1)/a^{n+1}$, where Γ is the Gamma function. Therefore, in the estimate of the total energy and number of reaccelerated electrons, we can approximate the integral in Eq. 4.27 as:

$$\int_1^\infty N(\gamma)\,(\gamma-1)\, d\gamma \;\approx\; \frac{{\rm e}^2}{4} N(\gamma_{\rm b})\, {\gamma_{\rm b}}^2 \tag{4.28}$$

and similarly:

$$\int_1^{\infty} N(\gamma)\, d\gamma \;\approx\; \frac{\mathrm{e}^2}{3} N(\gamma_{\mathrm{b}})\, \gamma_{\mathrm{b}} \tag{4.29}$$

Thus the adopted parameterization (Eq. 4.27) leads to:

$$N(\gamma_{\mathrm{b}})_x\, \gamma_{\mathrm{b},x}^2 = N(\gamma_{\mathrm{b}})_{\mathrm{c}}\, \gamma_{\mathrm{b,c}}^2 \cdot x^{-s} \tag{4.30}$$

The energetics associated with the reaccelerated electron population is:

$$E_{\mathrm{e}} = 4\pi\, r_{\mathrm{c}}^3 \int_{\mathrm{CF\ region}} \mathcal{E}(x)\, x^2\, dx \tag{4.31}$$

where, from Eq. 4.27 and 4.28, the total energy density is $\mathcal{E}(x) \approx (\mathrm{e}^2/4)\, m_{\mathrm{e}}c^2\, N(\gamma_{\mathrm{b}})_{\mathrm{c}}\, \gamma_{\mathrm{b,c}}^2 \cdot x^{-s}$, $N(\gamma_{\mathrm{b}})_{\mathrm{c}}$ being the number density (per γ unit) of electrons with energy $\gamma_{\mathrm{b}} m_{\mathrm{e}} c^2$ at r_{c}. It results:

$$E_{\mathrm{e}} \approx \frac{\pi\, r_{\mathrm{c}}^3\, \mathrm{e}^2\, m_{\mathrm{e}}c^2\, N(\gamma_{\mathrm{b}})_{\mathrm{c}}\, \gamma_{\mathrm{b,c}}^2}{(3-s)} \tag{4.32}$$

Similarly, one can calculate the total number of electrons as:

$$N_{\mathrm{e}} = 4\pi\, r_{\mathrm{c}}^3 \int_{\mathrm{CF\ region}} \mathcal{N}(x)\, x^2\, dx \tag{4.33}$$

where, from Eq. 4.29 the total number density is $\mathcal{N}(x) \approx (\mathrm{e}^2/3)\, N(\gamma_{\mathrm{b}})_x\, \gamma_{\mathrm{b},x}$, with $N(\gamma_{\mathrm{b}})_x\, \gamma_{\mathrm{b},x} = N(\gamma_{\mathrm{b}})_{\mathrm{c}}\, \gamma_{\mathrm{b,c}}\, (\gamma_{\mathrm{b,c}}/\gamma_{\mathrm{b},x}) \cdot x^{-s}$ (from Eq. 4.30). Since $\gamma_{\mathrm{b},x} \approx \gamma_{\mathrm{b,c}}$ in the cooling flow region, by integrating Eq. 4.33 it results:

$$N_{\mathrm{e}} \approx \frac{4}{3} \frac{\pi\, r_{\mathrm{c}}^3\, \mathrm{e}^2\, N(\gamma_{\mathrm{b}})_{\mathrm{c}}\, \gamma_{\mathrm{b,c}}}{(3-s)} \tag{4.34}$$

and therefore it is:

$$N_{\mathrm{e}} = \frac{4}{3} \frac{E_{\mathrm{e}}}{m_{\mathrm{e}}c^2\, \gamma_{\mathrm{b,c}}} \tag{4.35}$$

4.4.4 The Synchrotron Spectrum

The synchrotron emissivity of a population of relativistic electrons with energy distribution per unit solid angle $N(\gamma, \Omega)$ is given by (e.g. Ginzburg & Syrovatskii 1965; Pacholczyk 1970):

$$J_\nu = \int_\Omega \int_1^\infty p(\nu, \vartheta) N(\gamma, \Omega) d\gamma d\Omega \tag{4.36}$$

where

$$p(\nu, \vartheta) = \frac{\sqrt{3} e^3 B \sin\vartheta}{m_e c^2} F\left(\frac{\nu}{\nu_{\rm c}}\right) \tag{4.37}$$

is the emitted power per unit frequency and per unit solid angle from each electron, $F\left(\frac{\nu}{\nu_{\rm c}}\right)$ being the Kernel function and

$$\nu_{\rm c} = \frac{3}{4\pi} \frac{eB\sin\vartheta}{m_{\rm e} c} \gamma^2 \tag{4.38}$$

the critical frequency. Under the assumption of an isotropic distribution of electron momenta and of the magnetic field lines (at least if one considers a fraction of the cooling flow region), we can assume the synchrotron emissivity to be isotropic. In this case $N(\gamma, \Omega) = N(\gamma)/4\pi$, where in our model $N(\gamma)$ is given by Eq. 4.24.

Note that $N(\gamma_{\rm b})$ appearing in Eq. 4.24 can be derived from Eq. 4.30 in terms of the parameter s. The other free parameters in the model are the values at the cooling radius of the magnetic field intensity, $B_{\rm c}$, and of the characteristic distance between two subsequent peaks of MHD turbulence, $l_{\rm c}$. Once these three parameters are fixed, one can derive, as a function of x, the magnetic field intensity (Eq. 4.1 or 4.2), the losses (Eqs. 4.5 and 4.7), the reacceleration (Eq. 4.8) and the value of $\gamma_{\rm b}$ (Eq. 4.15), then from Eq. 4.24 one can calculate the spectral distribution of the electrons as:

$$N(\gamma) = N(\gamma_{\rm b})_{\rm c} \gamma_{\rm b,c}^2 \cdot \exp(-\Phi)\, x^{-s} \gamma_{\rm b}^{-2} \cdot \left(\frac{\gamma}{\gamma_{\rm b}}\right)^2 \exp\left[f\left(\frac{\gamma}{\gamma_{\rm b}}\right)\right] \tag{4.39}$$

where the first term is a costant value determined only by the initial parameters, the second term takes into account the radial dependence of the coefficients, and the third term is the shape of the spectrum which is independent of the distance.

With the energy distribution of the relativistic electrons given by Eq. 4.39, the synchrotron emissivity per unit solid angle is:

$$J_\nu(x) = K(x) \cdot \int_0^{\frac{\pi}{2}} \int_1^{\infty} \sin^2\vartheta \, F\left(\frac{\nu}{\nu_\mathrm{b}} \frac{{\gamma_\mathrm{b}}^2}{\gamma^2 \sin\vartheta}\right) \gamma^2 \exp\left[f\left(\frac{\gamma}{\gamma_\mathrm{b}}\right)\right] d\vartheta d\gamma \tag{4.40}$$

where

$$K(x) = \frac{\sqrt{3}e^3}{m_\mathrm{e}c^2} N(\gamma_\mathrm{b})_\mathrm{c}\, \gamma_{\mathrm{b,c}}^2 \cdot B(x)\, \gamma_\mathrm{b}^{-4} \exp(-\Phi)\, x^{-s} \tag{4.41}$$

ν_b being the critical frequency for $\gamma = \gamma_\mathrm{b}$ ($\vartheta = 90°$). The shape of the synchrotron spectrum is plotted in Fig. 4.4: at low frequencies the synchrotron spectrum is approximately proportional to $\nu^{-1/3}$, as in the case of the emission by a single electron, it remains roughly flat just below the break frequency (contributed by the electrons at the break energy γ_b) and then it falls down exponentially.

Again, once the three parameters of the model are fixed, the synchrotron emissivity at each distance x is uniquely determined by Eq. 4.40 and the model is able to provide some radio properties of the diffuse radio emission from the population of reaccelerated electrons . For example, by integrating Eq. 4.40 over the cluster volume at two different frequencies, we can calculate the total spectral index between these two frequencies, while by integrating the same equation along the line of sight we can calculate the surface brightness profile at a particular frequency.

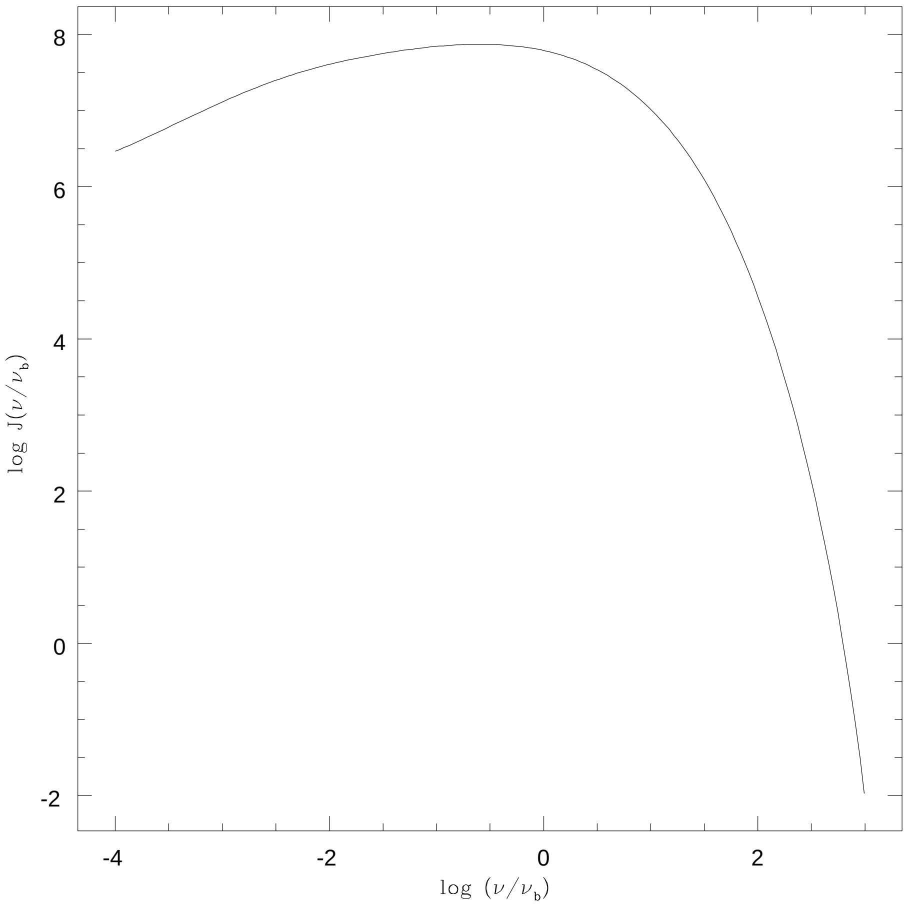

Figure 4.4: The predicted synchrotron spectrum from a population of relativistic electrons reaccelerated in the cooling flow region is shown in arbitrary units (see Eq. 4.40).

Chapter 5

Model Application to Observed Radio Mini–Halos

5.1 Introduction

In order to validate the model for the origin of radio mini–halos, presented in Chapter 4, we have applied it to observed mini–halo candidates.
In this Chapter we will present the application of this model to the prototype of the mini–halo source class, the Perseus cluster, and a new mini–halo candidate, Abell 2626, and discuss the physical implications of the results.
In particular, our aims are:

- to verify whether the model is able to reproduce the observed radio properties of the mini–halos in these clusters, in particular the brightness profile, the total radio spectrum and the steepening of the synchrotron spectrum with the distance from the center;
- to test the basic idea of the model, i.e. that the necessary energy to power radio mini–halos can be extracted by cooling flows.

5.2 Perseus Cluster

The first observed and well studied case of radio mini–halo is that in the Perseus cluster (Burns et al. 1992). This cluster (Abell 426), at a redshift $z = 0.0183$ ($1'$ corresponds to ~ 30 kpc), is one of the brightest clusters in the sky in X–ray band ($L_X \sim 2 \times 10^{45}\,\mathrm{erg\,s^{-1}}$, White, Jones & Forman 1997). The average temperature of the ICM is $kT = 6.33^{+0.21}_{-0.18}$ keV (Allen et al. 1992). The Perseus cluster hosts the nearest large cooling flow; X–ray deprojection analysis of *ROSAT* PSPC surface brightness profiles indicates that the mass deposition rate is $519^{+3}_{-17} \mathrm{M}_{\odot}\ \mathrm{yr}^{-1}$ and the cooling radius is 210^{+100}_{-20} kpc (Ettori, Fabian & White 1998). The electron number density at the cooling radius n_c can be estimated from $\dot{M}$ and r_c by Eq. 3.28 as:

$$n_{\rm c} \approx 2.18 \times 10^{-3}\ \mathrm{cm}^{-3} \left(\frac{\dot{M}}{100\ \mathrm{M}_{\odot}\ \mathrm{yr}^{-1}} \right) \left(\frac{r_{\rm c}}{100\ \mathrm{kpc}} \right)^{-3} \tag{5.1}$$

resulting $n_{\rm c} \sim 1.2 \times 10^{-3}\ \mathrm{cm}^{-3}$. The dominant galaxy in the cluster core is the

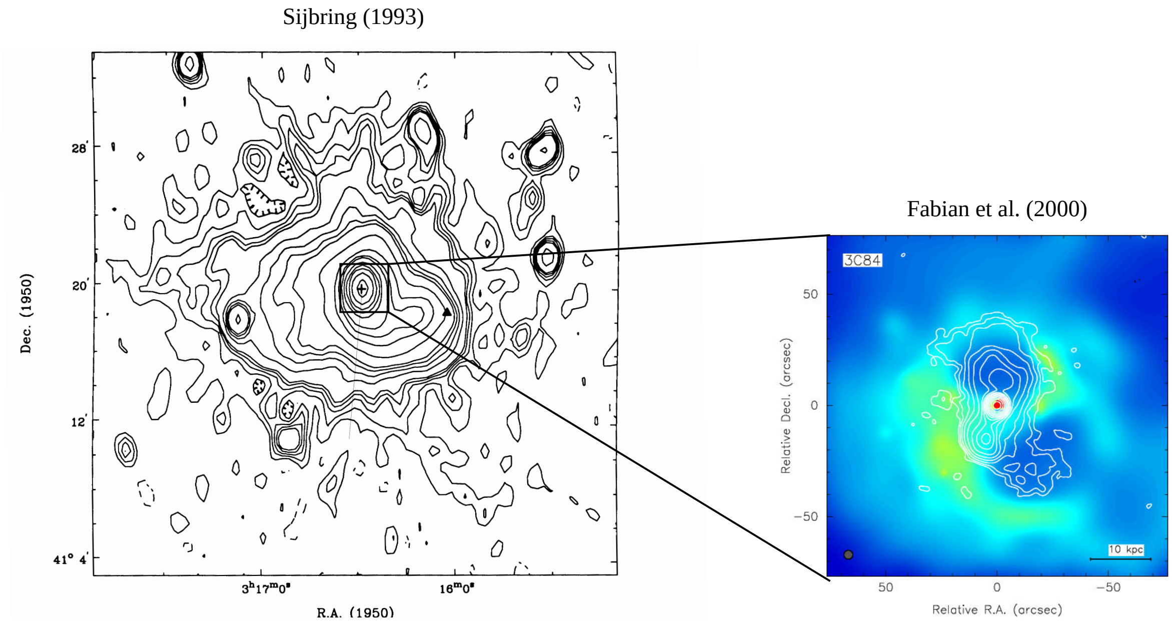

Figure 5.1: **Left panel**: 92 cm map of 3C 84 at a resolution of 51″ × 77″ (Sijbring 1993). The contour levels are -4 (dashed), 4, 8, 12, 16, 20, 40, 60, 80, 100, 200, 400, 600, 800, 1500, 2500, 4000, 8000, 16000 mJy/beam. The r.m.s. noise is 1.4 mJy/beam. The cross indicates the position of NGC1275 and the dashed line represents the direction we have considered. **Right panel**: X–ray (colours)/radio (contours) overlay for the central part of the Perseus cluster around NCG 1275 (Fabian et al. 2000).

active galaxy NGC 1275. The associated radio source (Perseus A or 3C 84) is one of the brightest radio sources (the total flux density at 327 MHz is 40.66 Jy), with a complex structure. The radio mini–halo, whose diffuse radio emission surrounds 3C 84, (see left panel in Fig. 5.1) has a total extension of $\sim 15'$ (comparable with that of the cooling flow region) and a morphology correlated with that of the cooling flow X–ray map (Sijbring 1993; Ettori, Fabian & White 1998). The radio mini–halo has a steep spectrum with spectral index $\alpha = 1.4$ (between 327 MHz and 609 MHz, $S_\nu \propto \nu^{-\alpha}$) and its total flux is 17.57 Jy at 327 MHz. In addition there is evidence for a spectral steepening in the outer regions (Sijbring 1993).

On smaller scales ($\sim 1'$), Böhringer et al. (1993) showed evidence of interaction between the radio lobes of the central radiogalaxy 3C 84 and the X–ray emitting intra–cluster gas. Recent results obtained with *Chandra* confirm this interaction (Fig. 5.1, right panel) and support the interpretation of the holes in the X–ray emission as due to buoyant radio lobes which are currently expanding subsonically (Fabian et al. 2002a). We notice that the spectral index in these lobes ranges from ~ 0.7 in the center to ~ 1.5 in the outer regions (Pedlar et al. 1990), i.e. a value similar to the spectrum of the mini–halo extended over a scale ~ 10 times larger. Thus it is difficult to find a direct connection between the radio lobes and the mini–halo in terms of simple particle diffusion or buoyancy: in fact, the expansion and buoyancy of blobs would produce adiabatic losses and a decrease of the magnetic field, causing a too strong steepening of the spectrum. On the other hand, by calculating the typical diffusion length as a function of γ of the electrons, one can estimate that the radio emitting electrons can not diffuse for more than about 30 kpc (see Sect. 2.3.3), and thus also electron diffusion can not explain the observed mini–halo size. The relativistic electrons of the mini–halo should then be reaccelerated and we can apply our model to this cluster.

5.2.1 Model Results

In order to compare the expected properties of the mini–halo in the model with those observed, we have considered the 92 cm (327 MHz) radio image shown in the left panel of Fig. 5.1. In this map the bright radio core of 3C 84 can be very

well approximated by a point–like source and we have estimated that the diffuse mini–halo emission is affected by this intense central emission only within $\sim 1'$ from the cluster center, in agreement with *ROSAT* and *Chandra* imaging which show an interaction between the radio lobes of 3C 84 and the ICM only on this scale (Böhringer et al. 1993; Fabian et al. 2000). For this reason, the application of our model is justified for $r \gtrsim 30$ kpc.
In order to test the prediction of the model we have calculated the following expected observable properties:

- *total spectrum*: the total synchrotron spectrum is obtained by integrating the synchrotron emissivity (Eq. 4.40 calculated with the observational parameters for the Perseus cluster) over the cluster volume, assumed to be spheric (we notice that the resulting spectrum in this model is weakly dependent on the radius of the sphere, and thus the assumption of spherical symmetry does not significantly affect the results);

- *brightness profile*: the surface brightness profile expected by the model is obtained by integrating the synchrotron emissivity at 327 MHz along the line of sight;

- *radial spectral steepening*: at varying projected radius, we obtain the surface brightness at 327 MHz and 609 MHz, and compute the spectral index between these two frequencies.

We notice that, in spite of the spherical symmetry assumed in our model, the left panel of Fig. 5.1 shows that the diffuse mini–halo is rather asymmetric. We have thus compared the expected brightness profile and radial spectral steepening in the model to the observed profiles along a particular direction across the apparently more regular region deprived of field radio sources. However, it is worth noticing that there exists a strong morphological correlation between the cooling flow X–ray map and the radio mini–halo (Ettori, Fabian & White 1998; Sijbring 1993). This means that our choice of a specific direction does not appear as an effective restriction to the conclusions we lead to by applying our spherically symmmetric model to such an asymmetric emission. On the contrary, our results could reasonably be applied to any other direction, once the correct values for the physical parameters of the cooling flow in that particular direction are taken into account. Moreover, this strong morphological correlation can be taken as a hint to the influence of the cooling flow over the relativistic plasma behaviour, hence supporting the idea of the electron reaccleration being powered by the cooling flow itself.

We have separately considered the two cases of field compression previously discussed (see Sec. 4.3.1). The free parameters of our model are the energy density distribution of the relativistic electrons, i.e. the parameter s of Eq. 4.26, and the values at the cooling radius of the magnetic field intensity, $B_{\rm c}$, and of the characteristic distance between two subsequent peaks of MHD turbulence, $l_{\rm c}$. In order to investigate the range of parameters required by the model to match the observations, the calculation has been performed as follows: for each case of field compression we have fixed s and we have allowed the other two parameters $B_{\rm c}$ and $l_{\rm c}$ to vary. Then, for a given set of parameters, we have calculated the brightness profile, the total spectrum and the radial spectral steepening and compared them with the observations.

Tribble's case of isotropic compression of the field gives results in agreement with the observations. The best results are obtained for $1.5 \lesssim s \lesssim 2.5$. The parameter space which well reproduces the surface brightness profile and the total synchrotron spectrum is in good agreement with that producing an acceptable radial spectral steepening. In particular, at the 90% confidence level the values of the parameters are: $s = 2 \pm 0.25$, $B_{\rm c} \sim 0.9$ - $1.2\ \mu$G, $l_{\rm c} \sim 35$ - 60 pc, $l_{\rm c}$ increasing with the strength of the magnetic field $B_{\rm c}$. For these parameters, from Eq. 4.15, one obtains that the break energy at the cooling radius is $\gamma_{\rm b} \simeq 1600$. For one set of the parameters which best reproduces all the observational contraints we show in Figs. 5.2, 5.3 and 5.4 the fits to the surface brightness profile, total spectrum and radial spectral steepening.

On the other hand, our model results, assuming Soker & Sarazin's case of radial field, are not compatible with the observations. In fact, it is not possible to reproduce the spectral steepening for the same values of the parameters which produce the observed radio surface brightness profile and total synchrotron spectrum (Fig. 5.4).

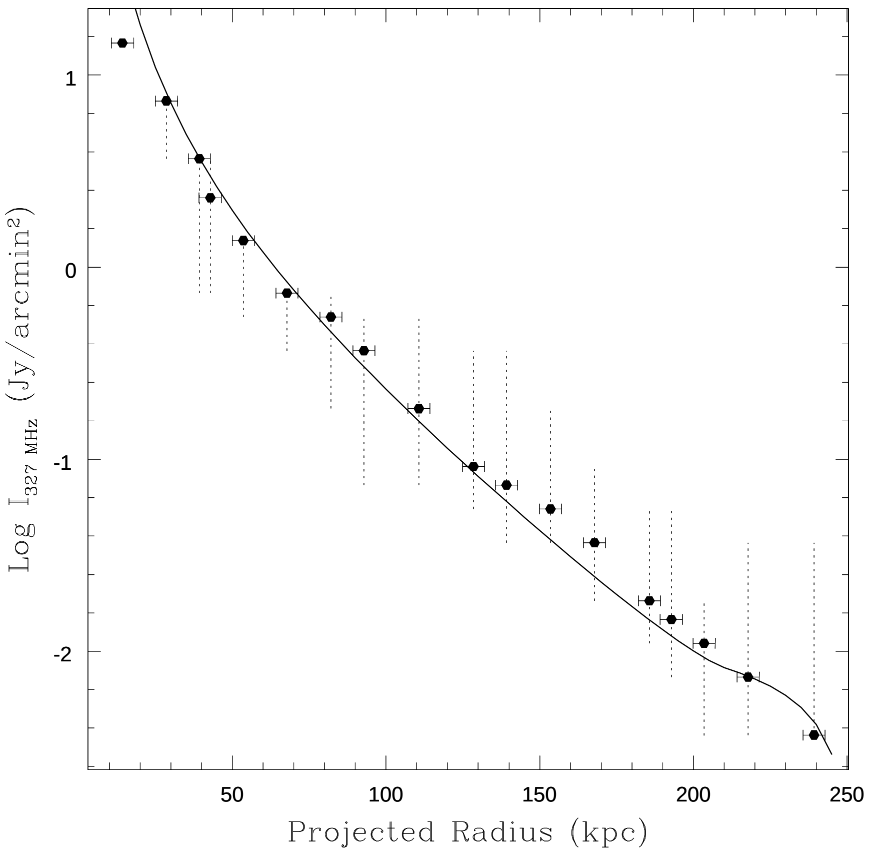

Figure 5.2: Fit to the surface brightness profile obtained in the case of isotropic field with the following set of parameters: $B_\mathrm{c} = 1.2\mu$G, $l_\mathrm{c} = 58$ pc, $s = 2.1$. Vertical bars represent the deviations from the spherical symmetry of the diffuse radio emission in other directions in the cluster with respect to the one we have considered (see left panel of Fig. 5.1).

The rapid decrease of the magnetic field towards the outer regions in Soker & Sarazin's case selects the relativistic electrons emitting between 327 - 609 MHz at progressively higher energies, causing a too rapid steepening of the synchrotron spectrum.

5.2.2 Discussion

We have shown that the main properties of the radio mini–halo in the Perseus cluster can be accounted for by the synchrotron radiation from relic relativistic electrons in

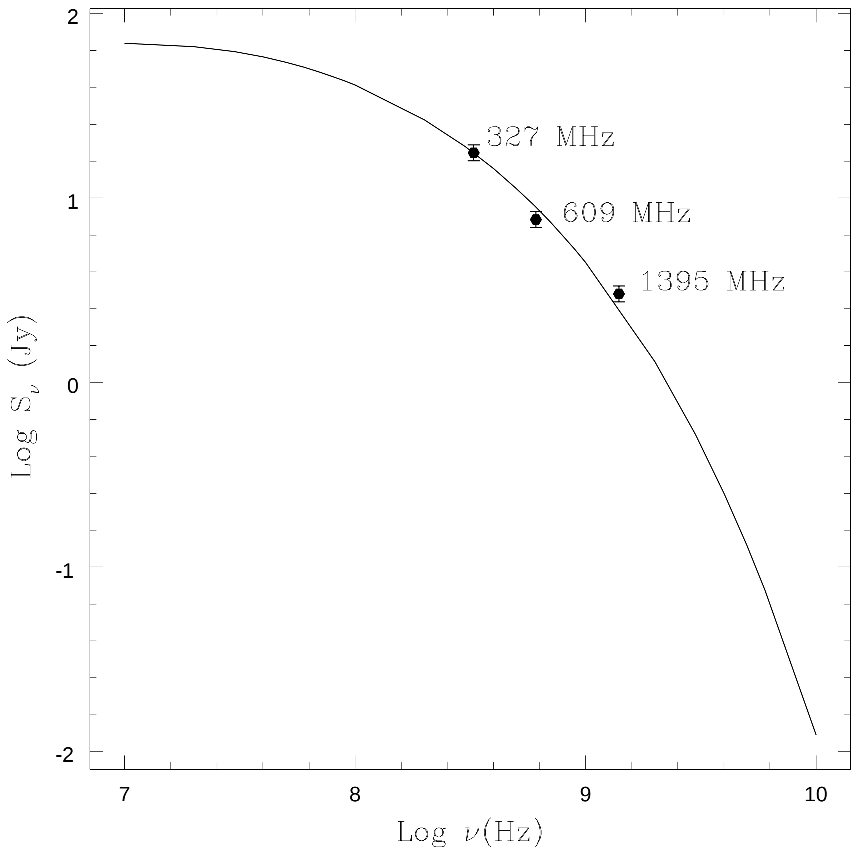

Figure 5.3: *Solid line*: fit to the total spectrum obtained with the same set of parameters of Fig. 5.2. The radio data are taken from Sijbring (1993).

the cluster, which are efficiently reaccelerated by MHD Fermi type mechanisms due to the compression of the cluster magnetic field in the cooling flow region. Under the assumption of an efficient MHD turbulence with $\delta B/B \sim 1$ and spherical symmetry, our model has only 3 free parameters, namely the magnetic field intensity $B_{\rm c}$ and the turbulence scale $l_{\rm c}$ at the cooling radius and the radial dependence of the relativistic electron energy density (parameterized as a power law of exponent $-s$ in Eq. 4.26).

Compression of the Magnetic Field

One important conclusion we have reached is that, in our model, an isotropic field compression appears to well reproduce the observed surface brightness profile and

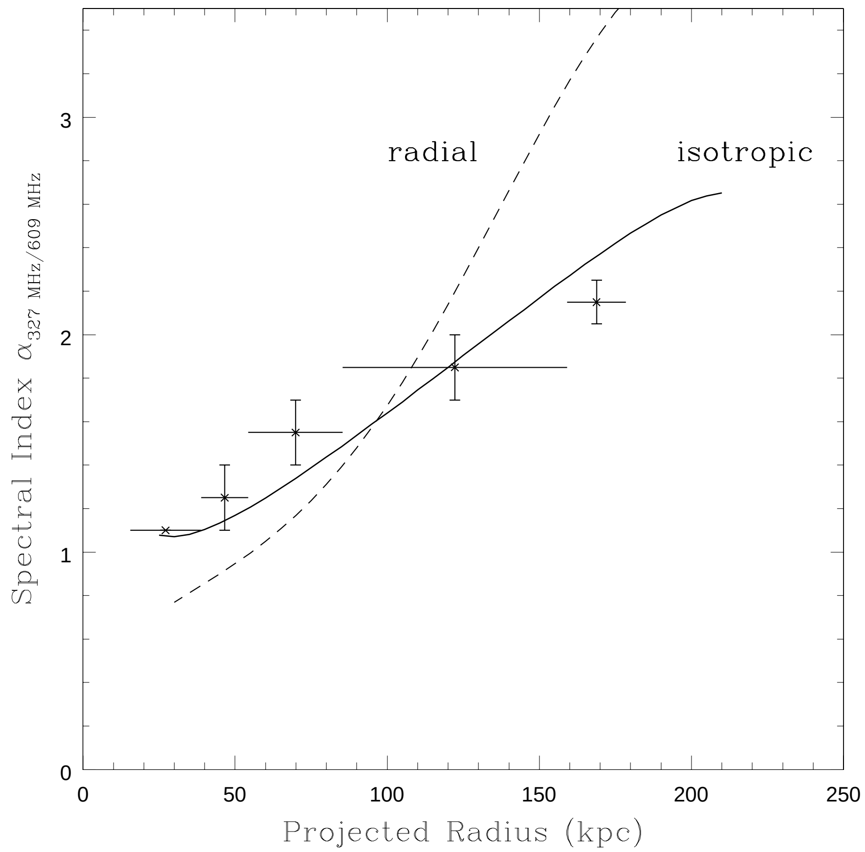

Figure 5.4: *Solid line*: fit to the radial spectral steepening between $\nu = 327$ MHz and $\nu = 609$ MHz obtained with the same set of parameters of Fig. 5.2. The data are taken from spectral index distribution map of Sijbring (1993) along the direction indicated in the left panel of Fig. 5.1. *Dashed line*: predicted spectral steepening in the case of radial field, for the values of parameters which match the observed brightness profile and total spectrum.

total synchrotron spectrum along with the radial spectral steepening. The fact that we can fit the spectral steepening for the same values of the parameters which provide a radio surface brightness profile and a total synchrotron spectrum in agreement with the observations (see Fig. 5.4) demonstrates the internal consistency of the model.

On the other hand, Soker & Sarazin's arguments leading to a prevailing radial field in the cooling flow do not appear applicable to the mini–halo in the Perseus cluster, as it is not possible to reproduce the radial spectral steepening for the same set of parameters reproducing the brightness profile and total radio spectrum. Our results show the goodness of Tribble's model in reproducing all the observational constraints and are consistent with the physical conditions prevailing in the cooling flow region of the Perseus cluster: at the cooling radius, the turbulent velocity (assumed to be the Alfvén velocity) is given by:

$$v_{\mathrm{T,c}} = v_{\mathrm{A}} \sim 69 \left(\frac{B_{\mathrm{c}}}{1\mu\mathrm{G}}\right)\left(\frac{n_{\mathrm{c}}}{10^{-3}\ \mathrm{cm}^{-3}}\right)^{-0.5} \quad \mathrm{km\ s}^{-1} \tag{5.2}$$

while the mean inflow velocity can be estimated as (Soker & Sarazin 1990):

$$v_{\mathrm{F,c}} \sim 21 \left(\frac{\dot{M}}{100\ \mathrm{M}_{\odot}\ \mathrm{yr}^{-1}}\right)\left(\frac{r_{\mathrm{c}}}{100\ \mathrm{kpc}}\right)^{-2}\left(\frac{n_{\mathrm{c}}}{10^{-3}\ \mathrm{cm}^{-3}}\right)^{-1} \mathrm{km\ s}^{-1} \tag{5.3}$$

In Perseus, we find that $v_{\mathrm{T,c}}$ ($\sim$ 60 km s^{-1}) is greater than $v_{\mathrm{F,c}}$ ($\sim$ 20 km s^{-1}), and thus an isotropic compression of the field is indeed expected (see Sec 4.3.1). Evidence in favour of Tribble's model in a number of cooling flows is also provided by Faraday rotation measurements (see Sect. 3.3.2). The range of values obtained for B_{c} is consistent with the measurements of magnetic fields diffused in the ICM (see Sect. 1.3.2).

Population of reaccelerated electrons

The energetics associated with the reaccelerated electron population in the cooling flow region, estimated from Eq. 4.32, is $E_{\mathrm{e}} \sim 1.6 \times 10^{58}$ erg. The number of relativistic electrons in the cooling flow region (Eq. 4.34) is $N_{\mathrm{e}} \sim 1.6 \times 10^{61}$. This is comparable to the number of the electrons in a typical radiogalaxy and may suggest an important role of the AGNs (and possibly of the central AGN) in the injecton of the electron relic population.

Once calculated the total number of relativistic electrons in the cooling flow region, we have estimated the energy rate P_{e} necessary to reaccelerate them. One possibility is to calculate the minimum energy one must supply to balance the radiative losses of the electrons: $P_{\mathrm{e}} \sim N_{\mathrm{e}} \cdot m_{\mathrm{e}} c^2 \beta \gamma_{\mathrm{b,c}}^2$ (β is that of Eq. 4.7). By assuming an average magnetic field in the cooling flow region of the order of

$\sim 3\mu$G (this value is justified by considering B_c obtained in the model and the radial behaviour of field amplification expected in the case of isotropic compression, see Fig. 4.1), we obtain:

$$P_e \approx 2 \times 10^{-26}\, \gamma_{b,c}^2 \cdot N_e \tag{5.4}$$

Cooling Flow as the Energy Source

In order to be consistent with the basic idea of the model, i.e. that radio mini–halos are powered by cooling flows, the necessary energy rate to reaccelerate the electrons should be significantly smaller than that supplied by the cooling flow.

The maximum possible energy rate P_{CF} which can be extracted from the cooling flow itself corresponds to the $p\,dV/dt$ work done on the gas per unit time as it enters r_c: $P_{CF} = p_c \cdot 4\pi r_c^2 \cdot v_{F,c}$, where we assume $p_c \sim 2n_c kT$. Note that this estimate of P_{CF} is consistent with the formula for the luminosity associated with the cooling region (see Eq. 3.19), resulting $P_{CF} = 2/5 L_{cool}$. One has:

$$P_{CF} \sim 2.3 \times 10^{43} \left(\frac{n_c}{10^{-3}\ \mathrm{cm}^{-3}}\right)\left(\frac{kT}{6\ \mathrm{keV}}\right)\left(\frac{r_c}{100\ \mathrm{kpc}}\right)^2 \cdot \left(\frac{v_{F,c}}{10\ \mathrm{km\ s}^{-1}}\right) \quad \mathrm{erg\ s}^{-1} \tag{5.5}$$

In the case of Perseus, one obtains that $P_{CF} \sim 2.6 \times 10^{44}$ erg s^{-1}, while the necessary energy rate to reaccelerate the relic population of electrons (Eq. 5.4) is $P_e \sim 8.9 \times 10^{41}$ erg s^{-1}. As a consequence, only a fraction of $\sim 0.34\%$ of P_{CF} should be converted into electron reacceleration, and thus processes associated with the cooling flow itself are able to provide sufficient energy to power the radio mini–halo.

MHD Turbulence Scale

Concerning the characteristic turbulence distance scale, a possible check for our model is whether or not the obtained values of l_c could be expected by some physical considerations on the turbulence in the ICM. In particular, assuming that the energy spectrum of MHD waves is a power law of the frequency ω, ($\propto \omega^{-\nu}$, $\nu > 1$, Lacombe 1977), we examine the possible value of the minimum frequency ω_{min}, i.e. the wavelength $L = 2\pi v_{\rm A}/\omega_{\rm min} = 2\pi/k_{\rm min}$ which carries most of the turbulent energy. Tsytovich (1972) suggests that the minimum frequency of an Alfvén wave spectrum is the collisional frequency of thermal protons, so that $k_{\rm min} \sim k_{\rm pp} \equiv 2\pi\nu_{\rm pp}/v_{\rm A}$, where $\nu_{\rm pp} = 3nT^{-3/2}$. For typical values of n and T in clusters of galaxies ($n \sim 10^{-3}$ cm^{-3}, $T \sim 10^7$ - 10^8 K), one has $L \sim 20$ - 600 pc, consistent with the order of magnitude of $l_{\rm c}$ obtained by our model.

The Emerging Picture

In the framework of our model, the possibility of giving rise to an observable radio mini–halo in a cooling flow region is related to several physical parameters. We have found that the electron spectrum near the cooling radius has a break energy which, for the values of parameters derived by fitting all the observational constraints, is approximately $\gamma_{\rm b} \sim 1600$. This value corresponds to the break energy of the relativistic electrons outside the cooling flow region, where no significant diffuse radio emission is detected. As the typical lifetime of $\gamma \sim 1600$ electrons (Eq. 4.3, with $B \sim \mu$G) is $\lesssim 1.5 \times 10^9$ yr, much less than the Hubble time, to balance the radiative losses of these electrons large–scale turbulence in the cluster volume is required. This scenario is similar to that of the classical cluster radio halos where, however, as the average magnetic field strength is considerably smaller than that in the cooling flow, higher energy electrons ($\gamma_{\rm b} \sim 10^4$) are required to emit in the radio band so that the turbulence efficiency would have to be correspondingly greater. In addition, we remind that in Perseus the turbulence can not be too high in order to avoid the disruption of the cooling flow.

Based on these considerations, we suggest that the physical conditions of the ICM in a cooling flow cluster which also shows a radio mini–halo are intermediate between those which lead to the formation of "standard" extended radio halos, hosted by clusters without cooling flows, and those holding in cooling flow clusters without radio halos. This could explain — at least qualitatively — the rarity of radio mini–halos.

The energetics of the turbulence plays the main part in discriminating between these two opposite situations. A turbulence with a high enough energy density will be efficient at reaccelerating the relativistic electrons: depending on the length scale of the turbulence, these electrons will be able to produce a diffuse synchrotron emission either in the form of extended radio halo or radio mini–halo. On the other hand, if the energy density of the turbulence is too low, independently of the turbulence scale there will be no efficient reacceleration of the electrons and consequently no formation of diffuse radio emission. Here we stress that the Perseus cluster may represent a borderline case: in fact there is evidence for a relatively recent merger event (Schwarz et al. 1992; Sijbring 1993; Dupke & Bregman 2001), which may have left a fossil turbulence still quite energetic, with a typical scale just above the limit for activating a radio halo, but not so weak to produce no reacceleration at all.

As a further step, we can set a quantitative constraint on the large–scale turbulence imposing that the reacceleration time scale (Eq. 4.9) well outside the cooling radius be more than 4 - 5 $\times 10^8$ yr, value derived by models on the formation of extended radio halos in clusters (Brunetti et al. 2001b). If this condition is verified then an extended radio halo will not be formed:

$$\left(\frac{l_{\rm c}}{1\rm pc}\right) \gtrsim 25 \left(\frac{n_{\rm c}}{10^{-3}\rm cm^{-3}}\right)^{-1} \left(\frac{B_{\rm c}}{1\mu\rm G}\right)^{2} \tag{5.6}$$

which represents the lower limit on the large–scale turbulence in order to avoid the formation of a radio halo. We notice that the value of the parameters obtained by our model for the Perseus cluster are relatively close (within a factor ~ 2) to this limit.

5.3 Abell 2626

The cluster Abell 2626, at a redshift $z = 0.0604$ (Rizza et al. 2000; $1'$ corresponds to ~ 95 kpc), hosts a relatively strong cooling flow (White, Jones & Forman 1997) and contains an amorphous radio source near to the center (Roland et al. 1985, Burns 1990) which is extended on a scale comparable to that of the cooling flow region with an elongation coincident with the X–ray distribution (see Fig. 5.5, Rizza et al.

2000). Therefore, Abell 2626 appears as a good mini–halo candidate and the similar morphology of the X–ray/radio map may suggest a physical connection between the cooling flow and the radio emitting plasma.

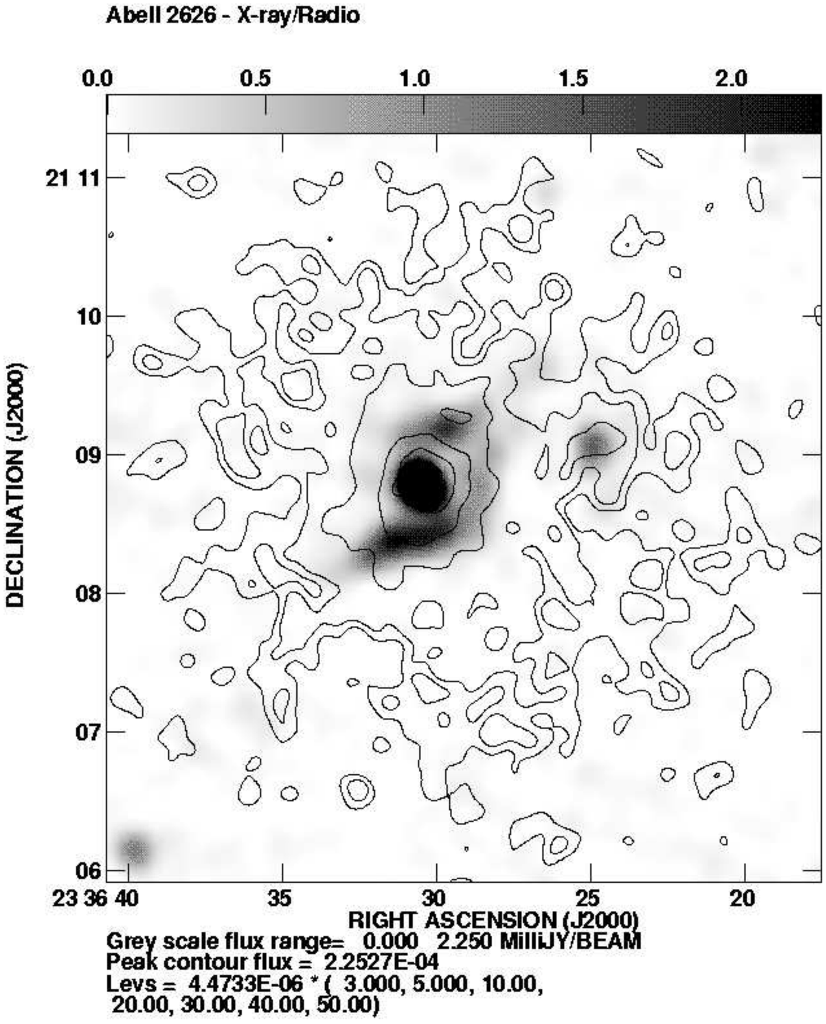

Figure 5.5: X–ray (contours, with *ROSAT*)/radio (grey scale) overlays for Abell 2626. From Rizza et al. 2000.

X–ray image deprojection analysis of *Einstein* IPC derived an average cluster temperature of $kT = 3.1^{+0.5}_{-1.0}$ keV, a mass deposition rate of $\dot{M} = 53^{+36}_{-30}$ $\dot{\mathrm{M}}_{\odot}$ yr^{-1} and a cooling radius of $r_c = 114^{+50}_{-59}$ kpc (White, Jones & Forman 1997). With these values of $\dot{M}$ and r_c, from Eq. 5.1 one estimates an electron number density at the

Table 5.1: VLA Data Archive

Proj Code	Source Name	Observation Date	Frequency (MHz)	Bandwidth (kHz)	Array	TOS (h)	RA (J2000) (h m s)	Dec (J2000) (° ′ ″)
AP001	3C464	Oct-22-1985	307.50/327.50	3.125	DnC	1.5	23 36 30	21 08 44
AR279	Abell 2626	May-04-1993	327.50/333.00	3.125	B	0.3	23 36 30	21 08 44
AR279	Abell 2626	Jul-15-1993	1464.900	5.000	C	0.5	23 36 30	21 08 44
ROLA	4C2057	Jul-20-1982	1464.900	5.000	B	0.7	23 36 30	21 08 06

cooling radius of $n_{\rm c} \sim 7.8 \times 10^{-4}$ cm^{-3}.

5.3.1 VLA Archive Data Analysis

In order to extend the application of our model to Abell 2626, we have requested and analyzed some of the VLA archive data (Table 5.1) of Abell 2626 with the aim to derive the surface brightness map, the total spectral index and the spectral index distribution of the diffuse radio emission.

Standard data reduction was done using the National Radio Astronomy Observatory (NRAO) AIPS package. We used the 1.5 GHz C array data and the 330 MHz B+DnC array data to produce low resolution images with a circular restoring beam of 17 arcsec. The imaging procedure at each frequency was performed using data with matched uv coverage.

These images (Fig. 5.6 and 5.7) allow to derive morphological and spectral information of the diffuse emission. The 1.5 GHz map (Fig. 5.6) shows an unresolved core and a diffuse boxy–shaped emission extended about $\sim 2'$, corresponding to about 190 kpc. No significant polarized flux is detected, leading to a limit of $< 2\%$ to the polarization percentage. An unrelated source is present west of the diffuse emission, with a total flux density of ∼3.9 mJy.

Because of the lower sensitivity, in the image at 330 MHz (Fig. 5.7), the diffuse structure is smaller in extent with respect to the 1.5 GHz one. It consists of two elongated almost parallel features located to the north and south of the core, respectively. No radio emission is detected at the location of the 1.5 GHz radio

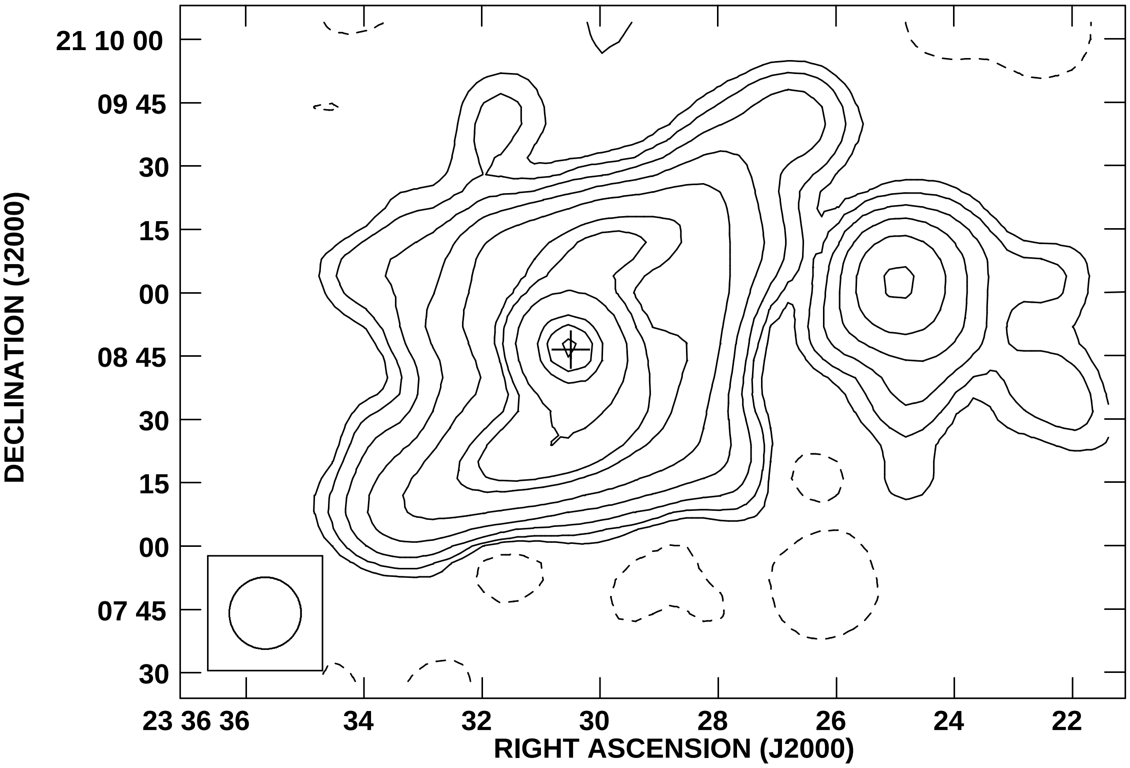

Figure 5.6: 1.5 GHz VLA map of Abell 2626 at a resolution of $17'' \times 17''$. The contour levels are -0.06 (dashed), 0.06, 0.12, 0.24, 0.48, 0.96, 1.92, 2.5, 4, 8, 10, 12 mJy/beam. The r.m.s. noise is 0.02 mJy/beam. The cross indicates the position of the cluster center.

nucleus. By taking for the 330 MHz core flux the 3σ upper limit, we obtain that the radio core has an inverted spectrum (see Table 5.2). The total flux density of the diffuse emission is $S_{330} \sim 1$ Jy. The unrelated source, detected at 1.5 GHz west of the diffuse radio emission, is not detected at 330 MHz. This implies a spectrum with $\alpha_{0.3}^{1.5} \lesssim 0.6$.

In order to estimate the total integrated flux density of the diffuse radio emission at 1.5 GHz and derive the surface brightness map and spectral trend, it is necessary to subtract the emission from the central nuclear source. One possibility is to make a high–resolution image and then extract the clean components of the central source.

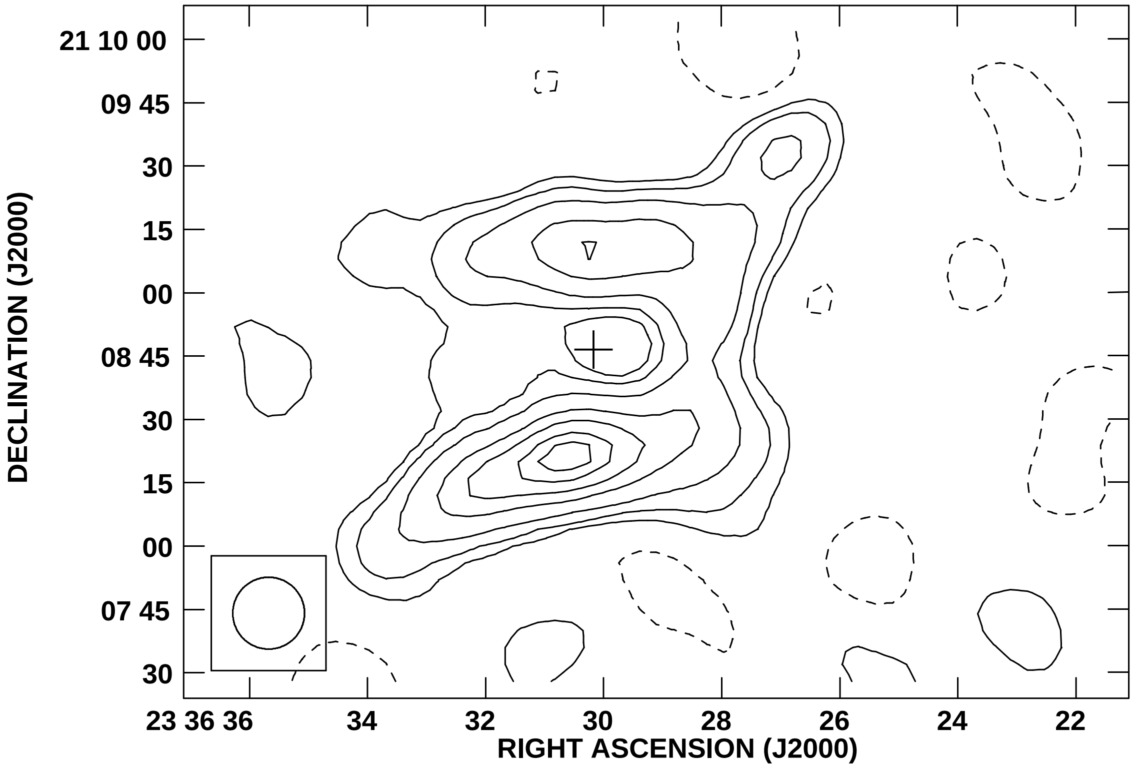

Figure 5.7: 330 MHz VLA map of Abell 2626 at a resolution of $17'' \times 17''$. The contour levels are -8.5 (dashed), 8.5, 17, 34, 68, 100, 135, 160 mJy/beam. The r.m.s. noise is 3.1 mJy/beam. The cross indicates the position of the center.

The 1.5 GHz B array data were used to obtain the high resolution image (Fig. 5.8) with a restoring beam of 4.5×3.9 arcsec. The central component is found to consist of an unresolved core, plus a jet–like feature pointing to the south–western direction. The extended emission is resolved out, and two elongated parallel features of similar brightness and extent are detected. The flux density of the central component, included the short jet, is $\simeq 13.5$ mJy, in agreement with Roland et al. (1985). The clean components of the central discrete source (jet included) were then restored with a circular beam of 17 arcsec and subtracted from the low–resolution map.

A radio image of the diffuse emission at 1.5 GHz, after the subtraction of the central discrete source, is shown in Fig. 5.9. This subtraction allows to derive a good estimate of the total flux density of the diffuse emission ($S_{1.5} \sim 29$ mJy). To be conservative, the region in which the surface brightness is affected by the subtraction procedure (within the dashed circle in Fig. 5.9) has not been considered in the application of the model.

The integrated spectral index of the diffuse emission between $\nu = 330$ MHz and $\nu = 1.5$ GHz is $\alpha \sim 2.4$. In Fig. 5.10 we show a greyscale image of the spectral index map of the diffuse radio emission between $\nu = 330$ MHz and $\nu = 1.5$ GHz. The spectrum steepens from the central region toward the north and south direction, with the spectral index increasing from ~1.2 to ~3. The steepening in the northern region is slighly smoother than in the southern one.

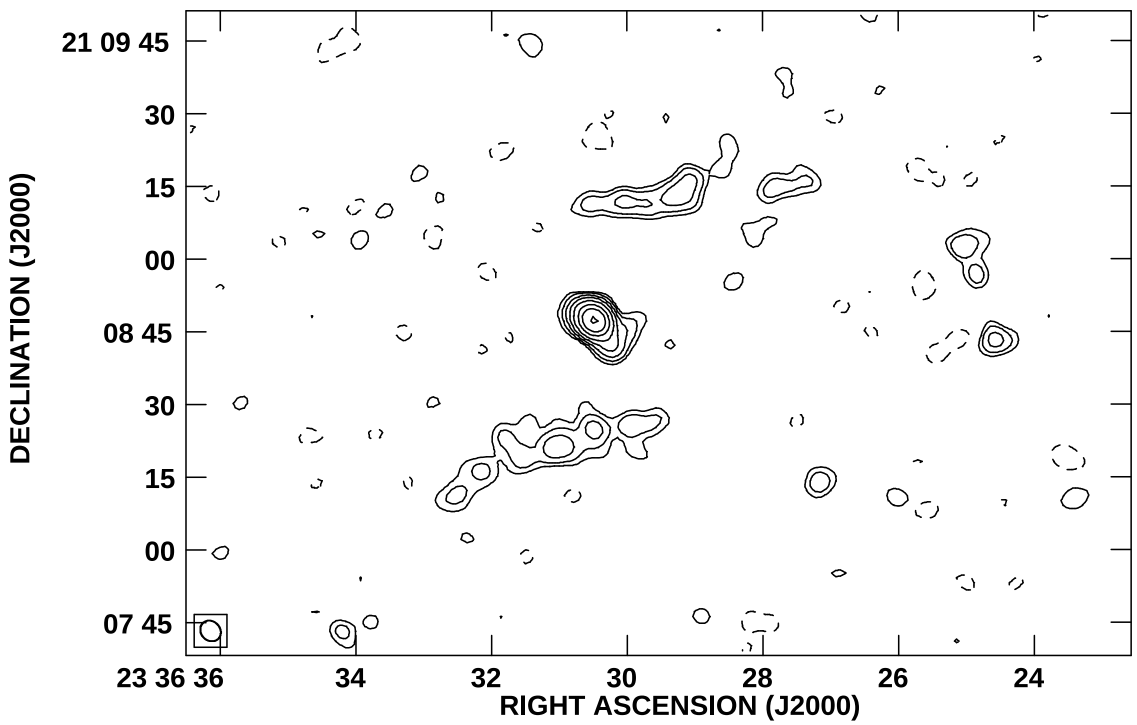

Figure 5.8: 1.5 GHz VLA map of Abell 2626 at a resolution of $4.5'' \times 3.9''$. The contour levels are -0.09 (dashed), 0.09, 0.18, 0.36, 0.7, 1.4, 3, 5.5, 11, 20 mJy/beam. The r.m.s. noise is 0.03 mJy/beam

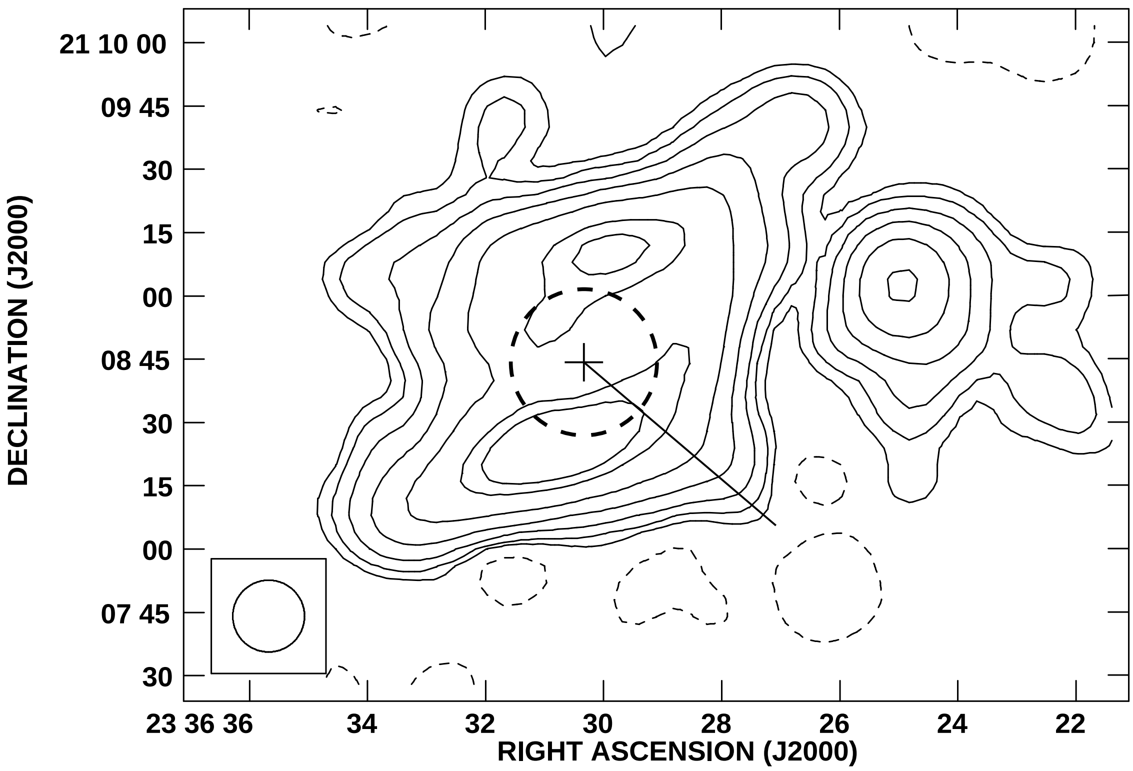

Figure 5.9: 1.5 GHz VLA map of Abell 2626 at a resolution of $17'' \times 17''$ after the subtraction of the central discrete source indicated by the cross. The contour levels are -0.06 (dashed), 0.06, 0.12, 0.24, 0.48, 0.96, 1.92, 2.5, 4, 8, 10, 12 mJy/beam. The r.m.s. noise is 0.02 mJy/beam. The dashed line defines the region in which the model is not applicable, while the solid line represents the direction we have considered for the surface brightness profile (see Fig. 5.11).

The radio results are summarized in Table 5.2.

5.3.2 Model Results

The results presented in Sect. 5.3.1 indicate that the extended radio source observed at the center of Abell 2626 can be classified as a mini–halo. Despite of the presence of a central radio core and of a jet–like feature, the diffuse emission has a boxy structure which can not be reconciled with the morphology of standard radio galaxies; moreover it shows a very steep spectrum which is uncommon in radio

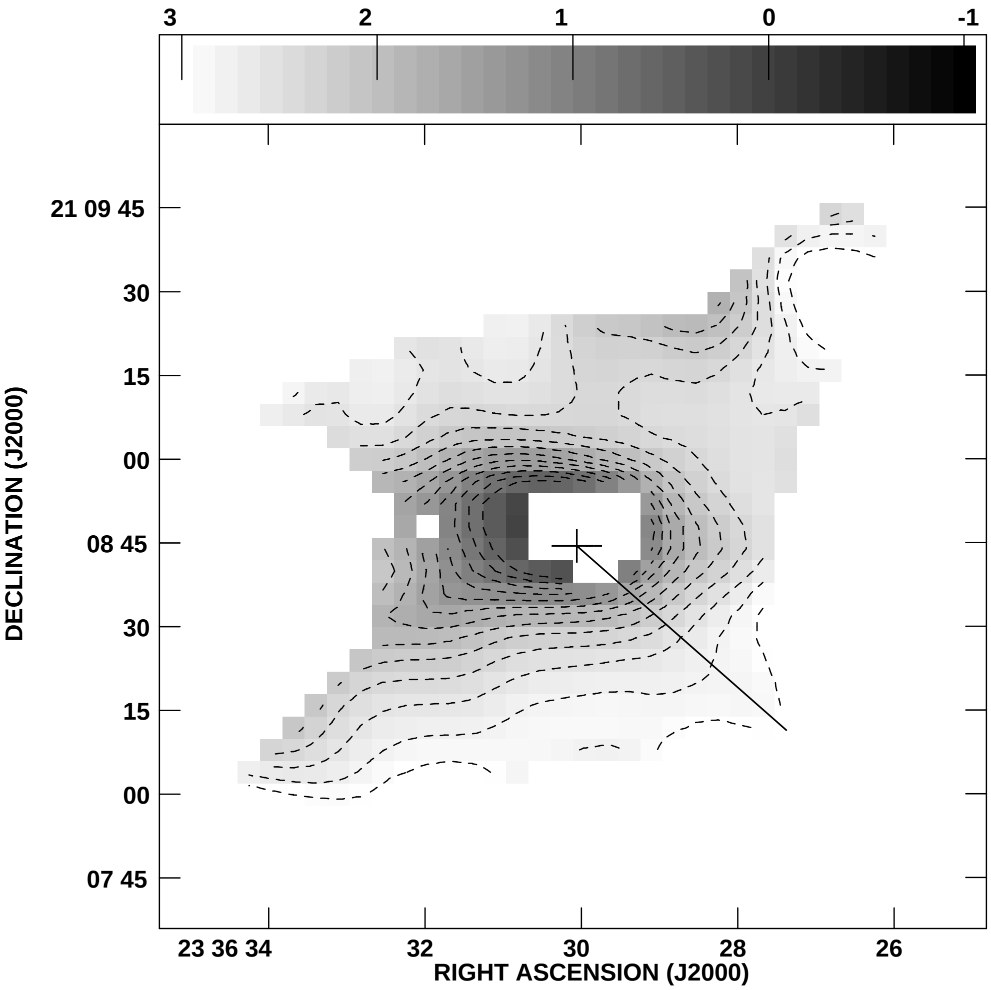

Figure 5.10: Spectral index distribution between $\nu = 330$ MHz and $\nu = 1.5$ GHz at a resolution of $17'' \times 17''$. The contours are in steps of 0.2, where the lightest grey is in the range 2.8 to 3. The lighter the grey, the steeper the spectral index. We have excluded the region in which the error is > 0.2. The cross indicates the position of the subtracted radio core and the solid line represents the direction we have considered for the spectral steepening profile (see Fig. 5.13).

Table 5.2: Radio results for Abell 2626

Emission	S_{330} (mJy)	$S_{1.5}$ (mJy)	Size (arcsec^2)	α ($S_\nu \propto \nu^{-\alpha}$)
Nuclear	<9.3	13.5 ± 1	-	$\lesssim -0.25$
Diffuse	990 ± 50	29 ± 2	135×128	2.37 ± 0.05

galaxies fed by an active nucleus. In addition, the lack of polarized flux is typical of amorphous radio sources in cooling flows (Sarazin 1997).

Qualitative scenario

The presence of the two structured radio features observed about 20″ on either side of the nucleus in the high resolution image at 1.5 GHz of Abell 2626 (Fig. 5.8) and the jet–like elongation of the nuclear component may indicate that there is still some injection of relatively young (10^8 yr) relativistic plasma in the cooling flow region. One possibility is that the two extended features are bubbles of radio emitting plasma, created by twin jets in the past, which are moving away from the center due to buoyancy, while the jet–like feature could be related to the present nuclear activity.

The qualitative picture is that a past radio activity may have injected radio–emitting plasma which then propagate through the cooling flow region in the form of buoyant subsonic plumes. We notice that the similar morphology of the X–ray distribution and the radio components (see Fig. 5.5) may support the scenario in which these radio bubbles are propagating in the cooling flow region and thus affected by this ambient. As shown by several authors who studied the hydrodynamic evolution of rising bubbles (e.g. Gull & Northover 1973; Churazov et al. 2000; Brüggen & Kaiser 2002), the moving away from the center is accompanied by adiabatic expansion and further mixing of the energetic radio source material with the ambient ICM. This latter process occurs via Kelvin-Helmholtz (K-H) instabilities on the surface of the bubbles and, more importantly, via Rayleigh-Taylor (R-T) instabilities in the "top" surface of the bubble that will actually disrupt and fragment it. Hydrodynamic simulations show a dramatic breakup and fine scale mixing of the bubble material with the ICM in about 10^7 - 10^8 years (e.g. Brüggen & Kaiser 2002); this is comparable to (or bigger than) the lifetime of the electrons producing synchrotron radiation.

The disruption of bubbles produced in past radio outbursts would then leave a population of relic relativistic electrons mixed with the thermal plasma in the cooling flow region. These relic electrons can diffuse in the thermal plasma up to $\sim$ 100 kpc scale in a few Gyr (e.g. Brunetti 2002) then filling the whole region inside the two elongated parallel features observed in Fig. 5.8, which instead may result from a more recent episod of nuclear activity. At this point, a subsequent reacceleration mechanism is needed for the relic electrons spread in the cooling flow region to produce the diffuse radio emission observed in Fig. 5.9.

Model application and results

Thus, it appears that the diffuse source observed in Abell 2626 is not directly related to the central radio core, and appears as a good candidate to apply our model for electron reacceleration in cooling flows.

One important conclusion reached in the application of the model to the Perseus cluster is that the results are compatible with the observations by assuming an isotropic compression of the magnetic field in the cooling flow region, while they are not by assuming a radial field. This is consistent with the fact that at the cooling radius the turbulent velocity (Eq. 5.2) is greater than the mean inflow velocity (Eq. 5.3), and one expects an isotropic compression of the field (Tribble 1993). In Abell 2626 one finds that $v_{\rm T,c} \sim 110$ km s^{-1} and $v_{\rm F,c} \sim 10$ km s^{-1}, thus we have only considered an isotropic compression of the magnetic field. Following the same procedure as for the Perseus cluster (Sect. 5.2.1), in order to test the prediction of the model we have calculated the following expected observable properties:

- *total spectrum*: the total synchrotron spectrum is obtained by integrating the synchrotron emissivity (Eq. 4.40 calculated with the observational parameters for Abell 2626) over the cluster volume, assumed to be spherical (again, we notice that the resulting spectrum in this model is weakly dependent on the radius of the sphere);

- *brightness profile*: the surface brightness profile expected by the model is obtained by integrating the synchrotron emissivity at 1.5 GHz along the line of sight;

- *radial spectral steepening*: at varying projected radius, we obtain the surface brightness at 330 MHz and 1.5 GHz, and compute the spectral index between these two frequencies.

The expected brightness profile and radial spectral steepening in the model are compared to the observed profiles along a particular direction (indicated in Fig. 5.9 and 5.10).

The values of the parameters required by the model to match the three observational constraints at the same time at the 90% confidence level are: $-0.5 \leq s \leq 0$, $B_{\rm c} \sim 1.35$ - 1.6 μG, $l_{\rm c} \sim 140$ - 200 pc, where the lower s, the lower $B_{\rm c}$ and $l_{\rm c}$. For these parameters, one obtains that the break energy at the cooling radius is $\gamma_{\rm b,c} \simeq 1100$. In Figs. 5.11, 5.12 and 5.13 we show the fits to the surface brightness profile, total spectrum and radial spectral steepening for one set of the parameters which best reproduces all the observational constraints.

5.3.3 Discussion

In this Section we will discuss the physical implications derived by applying our model to Abell 2626 and compare that with the results obtained for the Perseus cluster. The X–ray and radio data for these clusters are listed in Table 5.3 while the model results are summarised in Table 5.4.

It is worth pointing out that the model is able to reproduce all the observational constraints of Abell 2626 for physically–meaning values of the parameters (see columns 2, 3 and 4 in Table 5.4). In particular, the range of values obtained for $B_{\rm c}$ is in agreement with the typical measurements of magnetic field strengths in the ICM (see Sect. 1.3.2) and the values for the turbulence scale $l_{\rm c}$ are consistent with

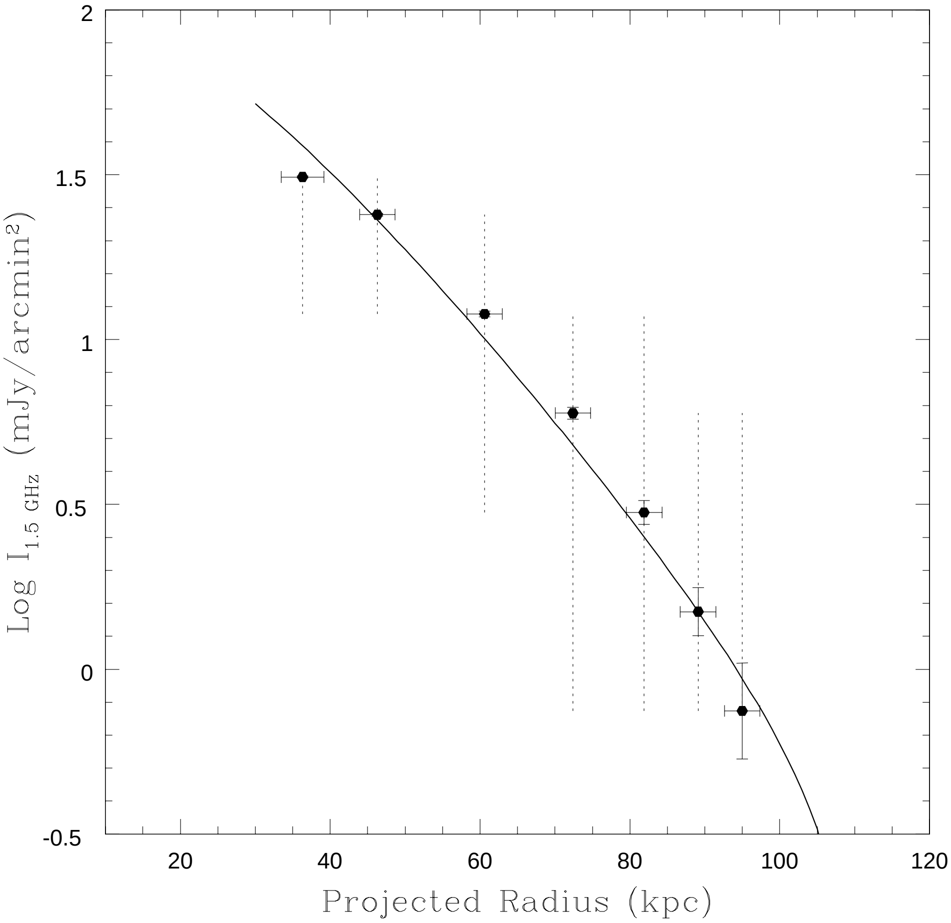

Figure 5.11: Fit to the surface brightness profile at 1.5 GHz obtained with the following set of parameters: $B_{\rm c} = 1.45\mu$G, $l_{\rm c} = 165$ pc, $s = -0.5$. Vertical bars represent the deviations from the spherical symmetry of the diffuse radio emission in other directions in the cluster with respect to the one we have considered (Fig. 5.9).

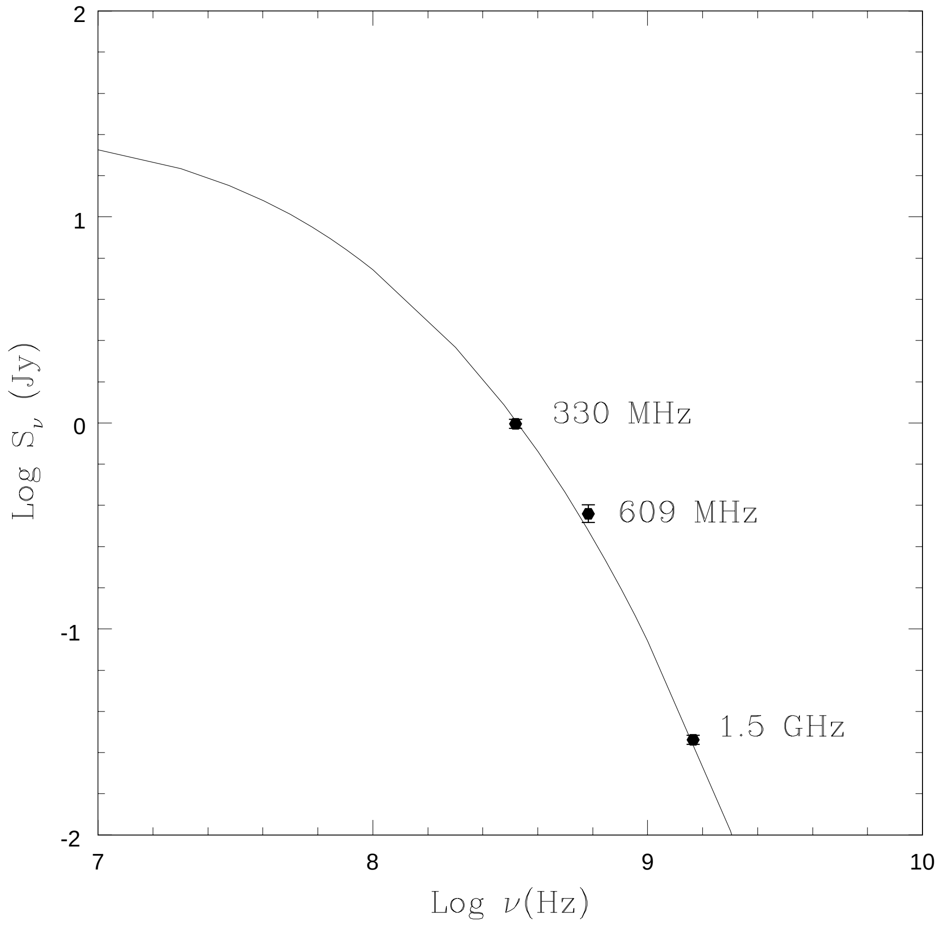

Figure 5.12: Fit to the total spectrum of the synchrotron emission obtained with the same set of parameters of Fig. 5.11. The flux densities observed at 330 MHz and 1.5 GHz are taken from Table 5.2, while the flux density at 609 MHz is obtained by subtracting the estimated core emission from the total flux given by Roland et al. 1985.

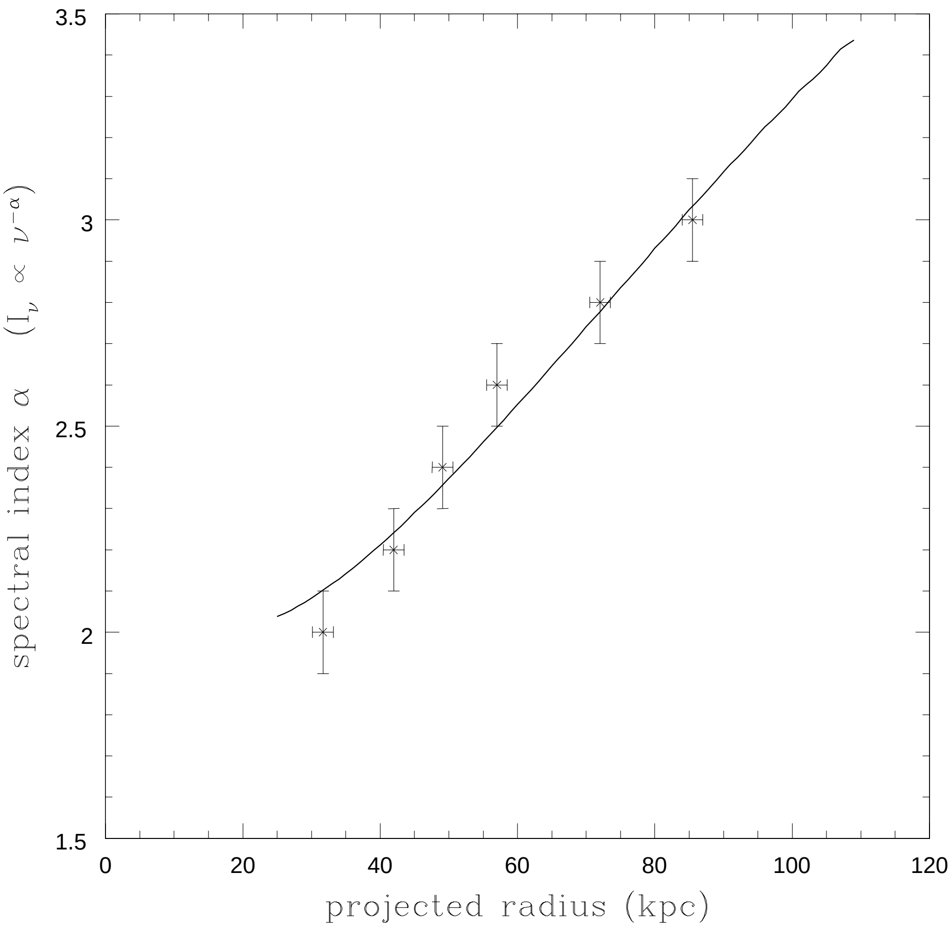

Figure 5.13: Fit to the radial spectral steepening between ν = 330 MHz and ν = 1.5 GHz obtained with the same set of parameters of Fig. 5.11. The data are taken from the spectral index distribution along the direction indicated in Fig. 5.10.

Table 5.3: Observational data for the cooling flow and mini–halo in Perseus and Abell 2626

	X–RAY DATA					RADIO DATA		
Cluster	$\dot{M}$ ($M_\odot$ yr^{-1})	r_c (kpc)	kT (keV)	n_c (cm^{-3})	P_{CF} (erg s^{-1})	$P_{1.5}$ (W Hz^{-1})	radius (kpc)	α ($S_\nu \propto \nu^{-\alpha}$)
Perseus	519^{+3}_{-17}	210^{+100}_{-20}	$6.33^{+0.21}_{-0.18}$	1.2×10^{-3}	2.6×10^{44}	4.4×10^{24}	~ 300	~ 1.4
Abell 2626	53^{+36}_{-30}	114^{+50}_{-59}	$3.1^{+0.5}_{-1}$	7.8×10^{-4}	1.2×10^{43}	4.3×10^{23}	~ 95	~ 2.4

Notes: Columns 2 and 3 list the cooling flow parameters, taken from Ettori, Fabian & White (1998) with *ROSAT* PSPC for Perseus and from White, Jones & Forman (1997) with *Einstein* IPC for Abell 2626. Column 4 lists the average temperature of the ICM, taken from Allen et al. (1992) with *Ginga* for Perseus and from White, Jones & Forman (1997) with *Einstein* IPC for Abell 2626. Column 5 lists the electron number density n_c, estimated from $\dot{M}$ and r_c by Eq. 5.1. Column 6 lists the power supplied by the cooling flow as estimated from X–ray data (see Eq. 5.5). Columns 7, 8 and 9 list the physical properties of the mini–halo. Radio data for Perseus are taken from Sijbring (1993).

Table 5.4: Model results for Perseus and Abell 2626

	MODEL PARAMETERS			MODEL RESULTS					
Cluster	B_c (μG)	l_c (pc)	s	$\gamma_{b,c}$	$N(\gamma_b)_c \cdot \gamma_{b,c}$ (cm^{-3})	E_e (erg)	N_e	P_e (erg s^{-1})	ϵ (%)
Perseus	0.9 - 1.2	35 - 60	~ 2	1600	2.2×10^{-12}	1.6×10^{58}	1.6×10^{61}	8.9×10^{41}	0.34
Abell 2626	1.35 - 1.6	140 - 200	~ 0	1100	5×10^{-12}	1.5×10^{57}	2.2×10^{60}	5.4×10^{40}	0.45

Notes: Columns 2, 3 and 4 list the parameters of the model derived by fitting all the observational constraints. Column 5, 6, 7, 8 and 9 list the physical properties derived by the model: respectively, the break energy of the electron spectrum at r_c, the number density of electrons with energy $\gamma_b m_e c^2$ at r_c, the energetics associated with the reaccelerated electrons in the cooling flow region (Eq. 4.32), their total number (Eq. 4.34) and the necessary power to reaccelerate them (Eq. 5.4). Column 10 lists the efficiency required by the cooling flow for reaccelerating the relativistic electrons, given in percetage of P_{CF} taken from colum 6 of table 5.3.

those expected from arguments of theory of turbulent plasma (e.g. Tsytovich 1972) when applied to the case of ICM (see Sect. 5.2.2).

Initial Distribution of Relic Electrons

Concerning the energy density of the relativistic electrons, we found that it is approximately constant inside the cooling flow region ($s \sim 0$). Since $\gamma_{\rm b}$ depends weakly on the radial distance, this means that the radial distribution of the number density of the electrons before the reacceleration is nearly constant, producing a sort of "plateau" of relic electrons in the cooling flow region. On the other hand, for Perseus we found that the energy density of the relativistic electrons increases towards the center (it is approximately proportional to the distance at the minus 2) and therefore the number density of the electrons before the reacceleration may not be constant.

If one assumes that the central AGN plays an important role in the injection of the relativistic electrons which form the seed population, the "plateau"of seed electrons required by the model in Abell 2626 would imply that electron diffusion from the central galaxy should be efficient with a diffusion length of seed electrons $\gtrsim r_{\rm c}$. We notice that the diffusion length of relic electrons at $\gamma \sim 10^2$ - 10^3 during their lifetime (~ 1 Gyr) is of the order of ~ 100 kpc (see Sect. 2.3.3), in agreement with this scenario.

Population of reaccelerated electrons

Table 5.4 summarises some physical properties of the reaccelerated electron population in Perseus and Abell 2626 which can be derived by applying our model (see columns 5, 6, 7, 8 and 9). The energetics associated with the population of reaccelerated electrons can be estimated from Eq. 4.32, while the total number of relativistic electrons reaccelerated in the cooling flow region can be estimated from the energetics by Eq. 4.35. With the model parameters found for Abell 2626, one obtains $E_{\rm e} \sim 1.5 \times 10^{57}$ erg and $N_{\rm e} \sim 2.2 \times 10^{60}$. It is worth noticing that both the energetics and the number of reaccelerated electrons in the cooling flow region are about one order of magnitude smaller than those found in Perseus. This is consistent with the radio power at 1.5 GHz, which is about one order of magnitude smaller than that in Perseus (see column 7 of table 5.3).

Cooling Flow as the Energy Source

Once calculated the total number of relativistic electrons in the cooling flow region, we have estimated the energy rate $P_{\rm e}$ necessary to reaccelerate them (Eq. 5.4, see column 9 of Table 5.4) and compared it with the maximum possible energy rate $P_{\rm CF}$ which can be extracted from the cooling flow itself (Eq. 5.5, see column 6 of Table 5.3). In the case of Abell 2626, one obtains that the necessary energy rate to reaccelerate the relic population of electrons is $P_{\rm e} \sim 5.4 \times 10^{40}$ erg s^{-1}, while the energy rate supplied by the cooling flow is $P_{\rm CF} \sim 1.2 \times 10^{43}$ erg s^{-1}, so only a fraction of ~ 0.45 % of it need be converted into electron reacceleration. We remind that a similar result is found for Perseus (see Sect. 5.2.2).

As a consequence, the cooling flow itself and the processes associated with it are able to provide sufficient energy to power the radio mini–halo also in the case of Abell 2626.

Chapter 6

Further Investigations and Prospects

6.1 Introduction

As discussed in Chapter 4 and 5, in this PhD thesis we suggest the existence of a direct physical connection between cooling flows and radio mini–halos. Therefore, we expect some correlations between mini–halo and cooling flow properties, and an observational check is needed. Unfortunately, the small number of known mini–halos do not allow to make statistical studies, however it is still possible to draw some considerations.

In this Chapter we will present the observational properties of the population of radio mini–halos in relation with those of host clusters (Sect. 6.2), and discuss them in the framework of our model (Sect. 6.3).

6.2 Observational Properties of Mini–Halos

6.2.1 Selected Mini–Halos

With the aim to explore the properties of mini–halos we selected a small sample of candidates from known diffuse radio sources in the literature. The candidates in the sample were selected based on both the presence of a cooling flow and a diffuse radio emission with no direct connection with a central radio source. In particular, since our model assumes a connection between the origin of the synchrotron emission and the cooling flow, we selected those clusters where the size of the diffuse radio

Table 6.1: Observational data for mini–halos

Cluster	z	$\dot{M}$ ($\mathrm{M_\odot}$ yr^{-1})	kT (keV)	$P_{1.4}$ (W Hz^{-1})
PKS 0745-191	0.1028	579^{+399}_{-215}	$8.3^{+0.5}_{-5.8}$	2.7×10^{25}
Abell 2390	0.2320	625^{+75}_{-75}	$9.5^{+1.3}_{-3.4}$	1.5×10^{25}
Perseus	0.0183	283^{+14}_{-12}	$6.3^{+1.5}_{-2.3}$	4.4×10^{24}
Abell 2142	0.0890	106^{+248}_{-106}	$11.4^{+0.8}_{-3.2}$	6.6×10^{23}
Abell 2626	0.0604	53^{+36}_{-30}	$3.1^{+0.5}_{-1.0}$	4.3×10^{23}
2A 0335+096	0.0350	105^{+88}_{-66}	$3.1^{+0.8}_{-0.8}$	1.1×10^{23}

References: **X–ray data:** Perseus, Abell 2142, Abell 2626: White, Jones & Forman (1997) with *Einstein* IPC; PKS 0745-191: White, Jones & Forman (1997) with *Einstein* HRI; 2A 0335-191: White et al. (1991) with *Einstein* SSS; Abell 2390: $\dot{M}$ from Böhringer et al. (1998) with *ROSAT* PSPC, kT from White, Jones & Forman (1997) with *Einstein* IPC. **Radio data:** PKS 0745-191: Baum & O'Dea (1991); Abell 2390: Bacchi et al. (2003); Perseus: Sijbring (1993); Abell 2142: Giovannini & Feretti (2000); Abell 2626: this work; 2A 0335-191: Sarazin, Baum & O'Dea (1995).

emission is comparable to the cooling radius. For this reason we excluded Abell 2052 and the Virgo cluster, which host amorphous radio sources (3C 317 and M87, respectively) with a size smaller than the cooling flow region. Relevant X–ray and radio data are reported in Tab. 6.1, along with references to the observational works.

6.2.2 Radio powers vs. Cooling Flow Powers

In Fig. 6.1 we reported the radio power at 1.4 GHz of the mini–halos (in terms of integrated radio luminosity νP_ν) versus the power of cooling flows, i.e. $P_{\rm CF} = \dot{M} kT/\mu m_{\rm p}$. A general trend is very clear, with the strongest radio mini–halos found in association with the most powerful cooling flows.

Comments on Observational X–ray Data

To be consistent, since for Abell 2626 the only available observation is from *Einstein* IPC, X–ray data were taken, when possible, from the catalog of White, Jones

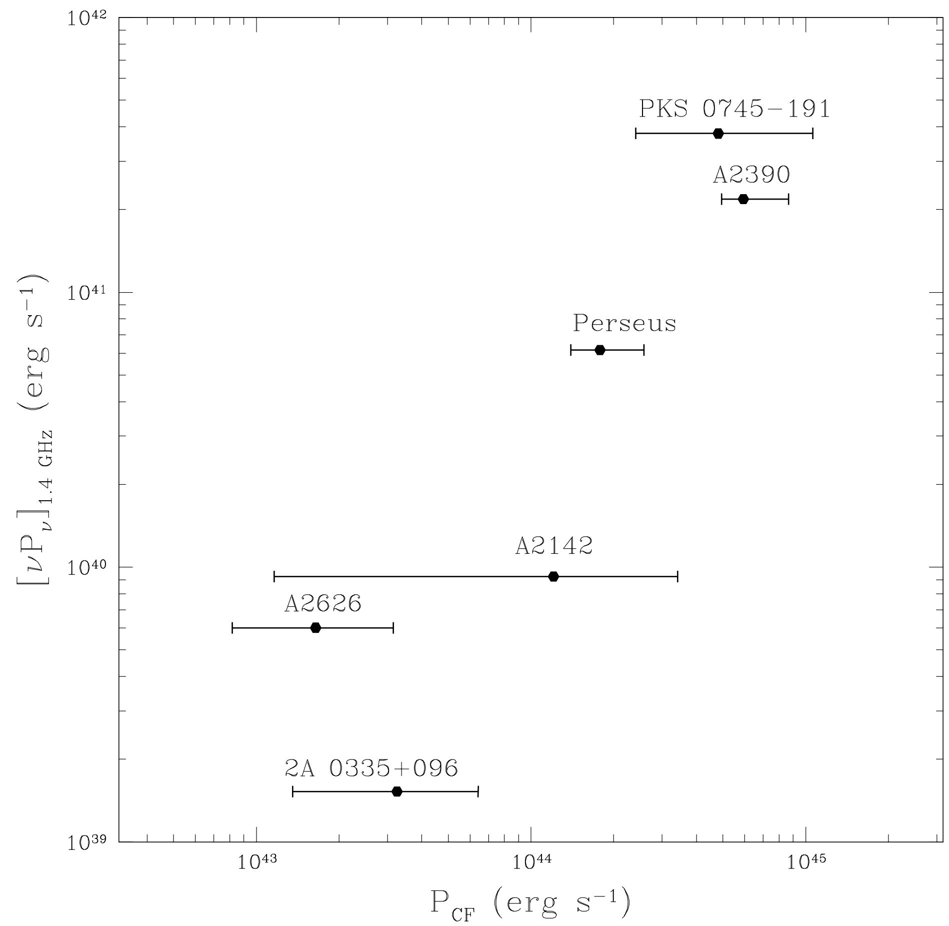

Figure 6.1: Integrated radio power at 1.4 GHz, $[\nu P_\nu]_{1.4\ \mathrm{GHz}}$, vs. cooling flow power, $P_{\mathrm{CF}} = \dot{M}kT/\mu m_{\mathrm{p}}$, for the mini–halo clusters in Tab. 6.1.

& Forman (1997) compiled with *Einstein Observatory.* For 2A 0335+096, not contained in this catalog, the data were taken from the *Einstein Observatory* Solid State Spectrometer (White et al. 1991). For Abell 2390, not detected as a cooling flow cluster by *Einstein* IPC, the value of $\dot{M}$ was taken from more recent observations with *ROSAT* PSPC, which have demonstrated the presence of a cooling flow in this cluster (Böhringer et al. 1998). We note that when both measurements from *Einstein* and *ROSAT* were available (e.g. Perseus, Abell 2142, PKS 0745 -191), the *Einstein*–based $\dot{M}$ resulted a factor ~ 2 below the *ROSAT*–based value. Thus the fact that for Abell 2390 we have considered X–ray data from a different satellite do not strongly affect the results, but simply produced a little right–shift of the the representative point in Fig. 6.1.

It is worth noticing that new *Chandra* and *XMM–Newton* results obtained for a limited number of objects hint to a possible overestimate of $\dot{M}$ derived by earlier observations. In particular, the consensus reached in these studies (see Sect. 3.4) is that the spectroscopically–derived cooling rates are factors of 5 - 10 less than earlier *ROSAT* and *Einstein* values. Therefore, even though uncertainties exists as to the reliability of cooling flow powers derived by X–ray measurements, these are very likely quasi–sistematic effects that will not spoil the trend reported in Fig. 6.1.

6.3 Model Predictions

We want to stress that the trend seen in Fig. 6.1 is expected in the framework of our model (see Chapter 4).

Qualitatively, $P_{\rm radio} \propto \langle\gamma_{\rm b}\rangle^2 \mathcal{N}_{\gamma_{\rm b}} \langle B\rangle^2 r_{\rm c}^3$, where $\langle\gamma_{\rm b}\rangle$ and $\langle B\rangle$ are the average values of gamma break and magnetic field in the cooling flow region, while $\mathcal{N}_{\gamma_{\rm b}}$ is the number density of relativistic electrons with Lorentz factor $\gamma = \gamma_{\rm b}$. We remind that the bulk of the observed radio emission is indeed produced by the electrons with Lorentz factor $\gamma \sim \gamma_{\rm b}$.

On the other hand, $P_{\rm CF} = p_{\rm c} \cdot 4\pi r_{\rm c}^2 \cdot v_{\rm F,c}$ (see Sect. 5.2.2) and, from Eqs. 3.3 and 3.28, one obtains: $P_{\rm CF} \propto p_{\rm c}\, r_{\rm c}^3$. Since cooling flows are pressure–constant processes (see Sect. 3.2.1), it results $P_{\rm CF} \propto r_{\rm c}^3$.

Therefore we expect $P_{\rm radio}$ increasing with $P_{\rm CF}$, with an efficiency ϵ which depends on details not considered in the model. As a first step, we can make the simple assumption of constant efficiency. In this case one has:

$$P_{\rm radio} = \epsilon \cdot P_{\rm CF}^{\delta} \tag{6.1}$$

where $\delta \sim 1$. In is worth noticing that Eq. 6.1 is based on both the assumptions of $(\delta B/B)^2 \sim 1$ in the cooling flow region and $\epsilon \approx$ const. Uncertainties in and deviations from these assumptions will cause a spread in the expected correlation between $P_{\rm radio}$ and $P_{\rm CF}$, but will not spoil it. Observatively, we notice that cooling flow powers are orders of magnitude larger than the integrated radio powers (see Fig. 6.1), in qualitative agreement with the very low efficiencies ϵ calculated in the model (see column 10 of Table 5.4).

Effects of Reduced Cooling Rates

Finally, it is worth pointing out that even if the reported value for $\dot{M}$ were sistematically overestimated of a certain factor, this would mean that the efficiency required by the cooling flow in the reacceleration increases by the same factor, and thus Eq. 6.1 remains still valid. In particular, the important point to note is that since corrections to the older data seem to amount to factors of order 5 - 10, we can safely conclude that the cooling flow powers (related to the mass flow rates) are well above the energy required for the reacceleration and, even more, well above the radio powers emitted by mini–halos.

Thus our conclusion is that the basic idea of this PhD work, i.e. that radio mini–halos are powered by cooling flows, is still valid.

Chapter 7

Summary and Conclusions

The work carried out in this PhD thesis concerns the study of the interaction between thermal intra–cluster medium (ICM) and relativistic plasma in cooling flow clusters of galaxies. In particular, in order to understand the nature and origin of the diffuse synchrotron emission from *radio mini–halos*, we studied the acceleration of relativistic electrons and their non–thermal radiation.

We developed a theoretical model which accounts for the origin of radio mini–halos as related to electron reacceleration in cooling flows. This model, which has been successfully applied to two clusters with mini–halo, represents a significant contribution to the understanding of these radio sources, whose origin had so far never been investigated in detail.

The conclusions of the PhD work can be summarized as follows:

Model for the origin of radio mini–halos

We have developed a model for radio mini–halos consisting in the reacceleration of relativistic electrons by MHD turbulence via Fermi–like processes. The MHD turbulence is assumed to be frozen in to the flow of the thermal ICM and it is thus amplified due to the compression of the turbulent coherence length scale and the amplification of the magnetic field in the cooling flow region. Our results showed that a relic population of relativistic electrons can be efficiently reaccelerated through this process, with the cooling flow itself providing the necessary energy. The effect of the reacceleration was included in the continuity equation giving the evolution of the number of electrons per unit energy. Under stationary conditions we derived the electron spectrum and the associated synchrotron emissivity as a function of the distance from the center and the three free parameters of the model: the magnetic field intensity and turbulence length scale at the cooling radius and the radial dependence of the electron energy density.

Model application to the Perseus Cluster and Abell 2626

The model was applied to the best studied mini–halo, that in the Perseus cluster, for which all data necessary for a comparison with model predictions were found in the literature, and to Abell 2626, for which we have produced surface brightness maps at two frequencies (330 MHz an 1.5 GHz) and the corresponding spectral index map. In both cases a very good agreement between the model and observations was found for the three observables: surface brightness profile, integrated spectrum and radial spectral steepening. The success of the model in reproducing the three observables with the same set of parameters shows its internal consistency. In addition, we found that only an isotropic compression of the magnetic field gives results in agreement with the data. Such an isotropic compression is indeed expected based on the physical conditions of both the Perseus and Abell 2626 cooling flows, again confirming the goodness of the model. Based on the best–fit values of the parameters, we estimated that in these two clusters a fraction as small as $\sim 0.4\%$ of the whole power supplied by the cooling flow need be converted in reacceleration of the electrons, thus validating the basic idea of the model. The fact that in both cases a similar efficiency is required to the cooling flow in order to supply the particle reacceleration may hint to a general property of this kind of mechanism.

Observational properties of mini–halos

With the aim to further explore the connection between mini–halos, ICM and cooling flows we collected data from the literature and studied the observational properties of the population of radio mini–halos in relation with those of host clusters. We found a trend where the radio power of mini–halos increases with the cooling flow power. This is in agreement with the expectations of our model, and gives further support to the model itself. We also considered the possible effects of new *Chandra* and *XMM–Newton* estimates of $\dot{M}$ and conclude that even if previously derived cooling rates were overestimated, cooling flow powers are still well above the radio powers of mini–halos. Therefore, as far as our model is concerned, these would only be minor changes with no implications on the basic idea. The trend we reported could be related to the more general problem of the missing X–ray luminosity from cooling flows, recently raised in the literature. In particular, in conjuction with other recent observations (mainly the correlation between rotation measures in cooling flow clusters and inferred $\dot{M}$), it may provide an important support to the idea that cooling flows, at least at some level, do exist.

As a general remark, we stress that many observational constraints have been found to fit very well in the framework of our model for the origin of radio mini–halos. Since in the model cooling flows play a crucial role in powering the diffuse radio emission, its successful application to observed clusters consitutes a very important point in favour of the existence of cooling flows.

Future Prospects

A step forward in this research will be provided by searching for other candidates of mini–halos, by comparing their fine radio properties with the predictions of the model and by making a statistical analysis of these properties in order to strengthen the observed trend between radio and cooling flow power. In addition, it would be very interesting to compare the properties of extended radio halos and mini–halos to better understand the differences of their origin. It is also worth investigating the role of the central AGN in the injection of the electron relic population. In this case, X–ray data analysis are required to clarify the connection between the cavities in the X–ray emission and the radio lobes of the central radiogalaxy in order to estimate the injection rate of relativistic electrons in the ICM by the central AGN.

Another interesting point related to our PhD work would be the study of the effects of turbulence in the ICM in the light of the *soft X–ray cooling flow problem*. We found that the energy necessary by MHD turbulence for the electron reacceleration is only a small fraction of the total cooling flow power, thus not affecting the cooling flow process itself. However, the energy reservoir in hydrodynamic turbulence may be larger, with only a small fraction associated to the MHD waves and some other fraction which may be converted in heating of the thermal ICM. It would be important to calculate the turbulence–induced heating of the ICM and study whether it can be efficient in balancing the cooling, thus affecting the whole cooling flow process.

Bibliography

[1] Abell G. O. 1958, *Ap.J.Suppl.*, 3, 211

[2] Allen S. W. 1998, *M.N.R.A.S.,* 296, 392

[3] Allen S. W. 2000, *M.N.R.A.S.,* 315, 269

[4] Allen S.W., Fabian A.C., Johnstone R.M., Nulsen P.E.J., & Edge A.C. 1992, *M.N.R.A.S.*, 254, 51

[5] Allen S. W., Fabian A. C., Johnstone R. M., White D. A., Daines S. J., Edge A. C., & Stewart G. C. 1993, *M.N.R.A.S.* 262, 901

[6] Allen S. W., & Fabian A. C. 1994, *M.N.R.A.S.,* 269, 409

[7] Allen S. W., Fabian A. C., Edge A. C., Bautz M. W., Furuzawa A., & Tawara Y. 1996, *M.N.R.A.S.,* 283, 263

[8] Allen S. W., & Fabian A. C. 1997a, in *Galactic and Cluster Cooling Flows*; ASP Conference Series; Vol. 115, p. 1, ed. N. Soker

[9] Allen S. W., & Fabian A. C. 1997b, *M.N.R.A.S.,* 286, 583

[10] Allen S. W., Fabian A. C., Johnstone R. M., Arnaud K. A., & Nulsen, P. E. J. 2001, *M.N.R.A.S.,* 322, 589

[11] Arnaud K. A. 1985, PhD Thesis, Univ. Cambridge

[12] Arnaud K. A. 1988, in *Cooling flows in Clusters and Galaxies*, ed A. C. Fabian, Dordrecht: Kluwer, p. 31

[13] Arnaud, M. 2001, in *Tracing cosmic evolution with galaxy clusters*, eds. Borgani, S., Mezzetti, M., & Valdarini, R., ASP Conf. Series vol. 268 p. 157

[14] Atoyan A. M., & Völk H. J. 2000, *Ap.J.,* 535, 45

[15] Bacchi M., Feretti L., Giovannini G., & Govoni F. 2003, *A.&A.* in press [astro–ph/0301206]

[16] Bahcall J. N., & Sarazin C. L. 1977, *Ap.J.,* 213, L99

[17] Bahcall J. N., & Sarazin C. L. 1978, *Ap.J.,* 219, 781

[18] Bahcall N. A. 1994, *Ap.J.*, 426, 513

[19] Baum S. A., & O'Dea C. P. 1991, *M.N.R.A.S.,* 250, 737

[20] Begelman M. & Fabian A. C. 1990, *M.N.R.A.S.,* 244, 26

[21] Bell A. R. 1978a, *M.N.R.A.S.,* 182, 147

[22] Bell A. R. 1978b, *M.N.R.A.S.,* 182, 443

[23] Berezinsky V. S., Blasi P., & Ptuskin V. S. 1997, *Ap.J.,* 487, 529

[24] Berger J. M., Newcomb W. A., Dawson J. M., Frieman E. A., Kulsrud R. M., & Lenard A. 1958, *Phys. Fluids* 1, 301

[25] Berghöfer T. W., Bowyer S., & Korpela E. 2000, *Ap.J.* 535, 615

[26] Berrington R. C., & Dermer C. D. 2002, contribution to the 13th Annual Astrophysics Conference in Maryland, *The Emergence of Cosmic Structure*, [astro-ph/0212461]

[27] Bertschinger E. & Meksin A. 1986, *Ap.J.,* 306, L1

[28] Binney J., & Tremaine S. 1987, *Galactic Dynamics*, Princeton University Press

[29] Blandford R. D. 1979, in *Particle acceleration mechanisms in astrophysics*; Proceedings of the Workshop, La Jolla, Calif., January 3-5, 1979. (A80-53201 24-90) New York, American Institute of Physics, 1979, p. 333-350

[30] Blandford R. D. 1986, in *Magnetospheric Phenomena in Astrophysics*, eds. R.I. Epstein & W.C. Feldman (New York: AIP), p.1

[31] Blandford R. D., & Ostriker J. P. 1978, *Ap.J.,* 221, L29

[32] Blandford R. D., & Eichler D. 1987, *Physics Rep.* 154, 1

[33] Blasi P. 2000, *Ap.J.,* 232, L9

[34] Blasi P. 2001, *Astrop. Phys.* 15, 275

[35] Blasi P., & Colafrancesco S. 1999, *Astrop. Phys.* 12, 169

[36] Böhringer H., Voges W., Fabian A.C., Edge A.C., & Neumann D.M. 1993, *M.N.R.A.S.,* 264, L25

[37] Böhringer H., Tanaka Y., Mushotzky R. F., Ikebe Y., & Hattori M. 1998, *A.&A.,* 334, 789

[38] Böhringer H., Belsole E., Kennea J., Matsushita K., Molendi S., et al. 2001, *Ap.J.,* 365, 181

[39] Böhringer H., Matsushita K., Churazov E., Ikebe Y., & Chen Y. 2002, *A.&A.,* 382, 804

[40] Bonamente M., Lieu R., & Mittaz J. P. D. 2001, *Ap.J* 546, 805

[41] Bonamente M., Lieu R., Joy M. K., & Nevalainen J. H. 2002, *Ap.J.,* 576, 688

[42] Borovsky J. E., & Eilek J. A. 1986, *Ap.J.,* 308, 929

[43] Bowyer S., & Berghöfer T. W. 1998, *Ap.J.,* 506, 502

[44] Bowyer S., Lieu R., & Mittaz J. 1998, in *The Hot Universe*, eds. K. Koyama, S. Kitamoto & M. Itoh (Dordrecht: Kluwer), 185

[45] Brighenti F., & Mathews W. G. 2002, *Ap.J.,* 573, 542

[46] Brüggen M., & Kaiser C., 2002, *Nature*, 418, 301

[47] Brunetti G. 2002, in *Matter and Energy in Clusters of Galaxies*, April 23–27 2002 Chung-Li, Taiwan; ASP Conf. Series, eds. S. Bowyer & C.-Y. Hwang, [astro–ph/0208074]

[48] Brunetti G., Feretti L., Giovannini G., & Setti G. 1999, in *Diffuse thermal and relativistic plasma in galaxy clusters*, eds. H. Böhringer, L. Feretti, P. Schuecker, MPE Report, 271, 263

[49] Brunetti G., Setti G., Feretti L., & Giovannini G. 2001a, *NewA* 6, 1

[50] Brunetti G., Setti G., Feretti L., & Giovannini G. 2001b, *M.N.R.A.S.,* 320, 365

[51] Buote D. A. 2001, *Ap.J.,* 553, L18

[52] Burbidge G. R. 1959, *Ap.J.,* 129, 849

[53] Burke J. R., & Silk J. 1974, *Ap.J.,* 190, 1

[54] Burns J.O. 1990, *A.J.* 99, 14

[55] Burns J.O., Sulkanen M.E., Gisler G.R., & Perley R.A. 1992, *Ap.J.,* 388, L49

[56] Cane H. V., Erickson W. C., Hanisch R. J., & Turner, P. J. 1981, *M.N.R.A.S.*, 196, 409

[57] Canizares C. R., Markert T. H., & Donahue M. E. 1988, in *Cooling flows in Clusters and Galaxies*, ed A. C. Fabian, Dordrecht: Kluwer, 63

[58] Carilli C. L., & Taylor G. B. 2002, *A.R.A.&A.,* 40, 319

[59] Cavaliere A., & Fusco-Femiano R. 1976, *A.&A.,* 49, 137

[60] Chandran B. D. G., & Cowley S. C. 1998, *Phis. Rev. Lett.* 80 Num. 14, 3077

[61] Chandrasekhar S. 1939, *An Introduction to the Study of Stellar Structure*, p.155, University of Chicago

[62] Chandrasekhar S. 1942, *Principles of Stellar Dynamics*, p.231, University of Chicago

[63] Christodoulou D. M., & Sarazin C. L. 1996, *Ap.J.,* 463, 80

[64] Churazov E., Forman W., Jones C., & Böhringer H. 2000, *A.&A.,* 356, 788

[65] Clarke T. E., Kronberg P. P., & Böhringer H. 2001, *Ap.J.,* 547, L111

[66] Colafrancesco S. 1999, in *Diffuse Thermal and Relativistic Plasma in Galaxy Clusters*, eds. Böringer H., Feretti L., Schuecker P.; MPE Report 271, p.269

[67] Colafrancesco S., & Blasi P. 1998, *Astrop. Phys.*, 9, 227

[68] Condon J. J., Cotton W. D., Greisen E. W., Yin Q. F., Perley, R. A., Taylor, G. B., & Broderick, J. J. 1998, *A.J.*, 115, 1963

[69] Cowie L. L., Fabian A. C., & Nulsen, P. E. J. 1980, *M.N.R.A.S.,* 191, 399

[70] Crawford C. S., Allen S. W., Ebeling H., Edge A. C., & Fabian, A. C. 1999, *M.N.R.A.S.,* 306, 857

[71] Daines S. J., Fabian A. C., & Thomas P. A. 1994, *M.N.R.A.S.,* 268, 1060

[72] Daly R. A., & Loeb A. 1990, *Ap.J.,* 364, 451

[73] David L. P., Nulsen P. E. J., McNamara B. R., Forman W., Jones C., Ponman T., Robertson B., & Wise M. 2001, *Ap.J.,* 557, 546

[74] Deiss B. M., Reich W., Lesch H., Wielebinski R. 1997, *A.&A.,* 321, 55

[75] den Herder J. W., Brinkman A. C., Kahn S. M., Branduardi-Raymont G., Thomsen K., et al. 2001, *A.&A.,* 365, L7

[76] Dennison B. 1980, *Ap.J.*, 239, L23

[77] De Young D. S. 1992, *Ap.J.,* 386, 464

[78] Dixon W. V. D., Hurwitz M., & Ferguson H. C. 1996, *Ap.J.,* 469, L77

[79] Dogiel V. A. 2000, *A.&A.,* 357, 66

[80] Dolag K., Bartelmann M., & Lesch H. 1999, *A.&A.,* 362, 151

[81] Dolag K., & Enßlin T. A. 2000, *A.&A.,* 362, 151

[82] Dolag K., Schindler S., Govoni F., & Feretti L. 2001, *A.&A.,* 378, 777

[83] Dolag K., Bartelmann M., & Lesch H. 2002, *A.&A.,* 387, 383

[84] Donahue M., Mack J., Voit G. M., Sparks W., Elston R. & Maloney P. R. 2000 *Ap.J.,* 545, 670

[85] Draine B. T., & Salpeter E. E. 1979, *Ap.J.,* 231, 77

[86] Dreher J. W., Carilli C. L., & Perley R. A. 1987, *Ap.J.,* 316, 611

[87] Dressler A. 1980, *Ap.J.,* 236, 351

[88] Drury L. O'C. 1983, *Rep. Prog. Physics*, 46, 973

[89] Dupke R. A., & Bregman J. N. 2001, *Ap.J.,* 547, 705

[90] Ebeling H., Voges W., Böhringer H., Edge A. C., Huchra J. P., & Briel U. G. 1996, *M.N.R.A.S.,* 281, 799

[91] Edge A. C. 2001, *M.N.R.A.S.,* 328, 762

[92] Edge A.C., & Stewart G.C. 1991a, *M.N.R.A.S.*, 252, 414

[93] Edge A.C., & Stewart G.C. 1991b, *M.N.R.A.S.*, 252, 428

[94] Edge A. C., Stewart G. C., & Fabian A. C. 1992, *M.N.R.A.S.,* 258, 177

[95] Edge A. C., Ivison R. J., Smail I., Blain A. W., & Kneib J.-P. 1999, *M.N.R.A.S.,* 306, 599

[96] Eilek J. A. 1979, *Ap.J.,* 230, 373

[97] Eilek J. A. 1999, in *Diffuse Thermal and Relativistic Plasma in Galaxy Clusters*, eds. Böringer H., Feretti L., Schuecker P.; MPE Report 271, p.71

[98] Eilek J. A., & Hughes P. A. 1991, in *Beams and Jets in Astrophysics*, ed. P. A. Hughes (Cambridge University Press)

[99] Eilek J., & Weatherall J. C. 1999, in *Diffuse thermal and relativistic plasma in galaxy clusters*, Eds. H. Böhringer, L. Feretti, P. Schuecker, MPE Report 271, 249

[100] Enßlin T. A. 1999, in *Diffuse thermal and relativistic plasma in galaxy clusters*, Eds. H. Böhringer, L.Feretti, P.Schuecker, MPE Report, 271, 275

[101] Enßlin T. A., & Biermann P. L. 1998, *A.&A.,* 330, 90

[102] Enßlin, T. A., Biermann P. L., Klein U., & Kohle, S. 1998, *A.&A.,* 332, 395

[103] Enßlin T. A., Lieu R., & Biermann P. L. 1999, *A.&A.,* 344, 409

[104] Enßlin T. A., & Gopal-Krishna 2001, *A.&A.,* 366, 26

[105] Enßlin T. A., & Brüggen M. 2002, *M.N.R.A.S.,* 331, 1011

[106] Ettori S., Fabian A. C., & White D. A. 1998, *M.N.R.A.S.,* 300, 837

[107] Ettori S., Fabian A. C., Allen S. W., & Johnstone, R. M. 2002, *M.N.R.A.S.,* 331, 635

[108] Fabian A.C. 1994, *A.R.A.&A.,* 32, 277

[109] Fabian A. C. 1997, *Science*, 275, 48

[110] Fabian A. C. 2002, to appear in *Galaxy Evolution: Theory and Observations*, Eds. V. Avila-Reese, C. Firmani, C. Frenk, & C. Allen, RevMexAA SC, [astro-ph/0210150]

[111] Fabian A. C., & Nulsen P. E. J. 1977, *M.N.R.A.S.,* 180, 479

[112] Fabian A. C., Hu E. M., Cowie L. L., & Grindlay, J. 1981, *Ap.J.,* 248, 47

[113] Fabian A. C., Nulsen P. E. J., & Canizares C. R. 1984, *Nature*, 310, 733

[114] Fabian A. C., Nulsen P. E. J., & Canizares C. R. 1991, *A.R.A.&A.,* 2, 191

[115] Fabian A. C., Arnaud K. A., Bautz M. W., & Tawara Y. 1994, *Ap.J.,* 436, L63

[116] Fabian A. C., Sanders J. S., Ettori S., Taylor G. B., Allen S. W., et al. 2000, *M.N.R.A.S.,* 318, 65

[117] Fabian A. C., Mushotzky R. F., Nulsen P. E. J., & Peterson, J. R. 2001, *M.N.R.A.S.,* 320, 20

[118] Fabian A. C., Celotti A., Blundell K. M., Kassim N. E., & Perley R. A. 2002a, *M.N.R.A.S.,* 331, 369

[119] Fabian A. C., Allen S. W., Crawford C. S., Johnstone R. M., Morris R. G., Sanders J. S., & Schmidt R. W. 2002b, *M.N.R.A.S.,* 332, 50

[120] Fabian A. C., Voigt L. M., & Morris R. G. 2002, *M.N.R.A.S.,* 335, L71

[121] Felten J. E., Gould R. J., Stein W. A., & Woolf N. J. 1966, *Ap.J.,* 146, 955

[122] Feretti L. 1999, in *Diffuse Thermal and Relativistic Plasma in Galaxy Clusters*, eds. Böringer H., Feretti L., Schuecker P.; MPE Report 271, p.3

[123] Feretti L. 2001, in *The Universe at Low Radio Frequencies*, Symp. IAU 199, Pune (India) [astro-ph/0006379]

[124] Feretti L., Dallacasa D., Giovannini G., & Tagliani A. 1995, *A.&A.,* 302, 680

[125] Feretti L., & Giovannini G. 1996, *IAUS*, 175, 333

[126] Feretti L., & Giovannini G. 1998, Proceedings of the meeting held in Marseilles (France), June 17-20, 1997, Eds.: Mazure A., Casoli F., Durret F. , Gerbal D., Word Scientific Publishing Co Pte Ltd, p 123.

[127] Feretti L., Brunetti G., Giovannini G., Govoni F., & Setti G. 2000, Contribution to the IAP 2000 Conference *Constructing the Universe with Clusters of Galaxies*, Paris, July 2000, eds. F. Durret & D. Gerbal

[128] Feretti L., Fusco-Femiano R., Giovannini G., & Govoni F. 2001, *A.&A.,* 373, 106

[129] Fermi, E. 1949, *Phys. Rev*, 75, 1169

[130] Flannery B. P., & Krook M. 1978, *Ap.J.*, 223, 447

[131] Fort B., & Mellier Y. 1994, *A.R.A.&A.,* 5, 239

[132] Fujita Y., & Sarazin C. L. 2001, *Ap.J.,* 563, 660

[133] Fukazawa Y., Ohashi T., Fabian A. C., Canizares C. R., Ikebe Y., Makashima K., Mushotzky R. F., & Yamashita K. 1994, *PASJ* 46, L55

[134] Fusco-Femiano R., dal Fiume D., Feretti L., Giovannini G., Grandi P., Matt G., Molendi S., & Santangelo A. 1999, *Ap.J.*, 513, L21

[135] Fusco-Femiano R., dal Fiume D., De Grandi S., Feretti L., Giovannini G., Grandi P., Malizia A., Matt G., & Molendi S. 2000, *Ap.J.,* 534, L7

[136] Fusco-Femiano R., Orlandini M., De Grandi S., Molendi S., Feretti L., Giovannini G., Bacchi M., & Govoni F. 2003, *A.&A.* in press, [astro-ph/0212408]

[137] Gabici S., & Blasi P. 2003, *Ap.J.,* 583, 695

[138] Ge J. P. 1991, PhD Thesis, New Mexico Inst. of Mining and Technology, Socorro

[139] Ge J. P., & Owen F. N. 1993, *A.J.*, 105, 778

[140] Giacconi R., Murray S., Gursky H., Kellogg E., Schreier E., & Tananbaum, H. 1972, *Ap.J.,* 178, 281

[141] Ginzburg V. L., & Syrovatskii S. I. 1965, *A.R.A.&A.,* 3, 297

[142] Giovannini G., & Feretti L. 2000, *NewA*, 5, 335

[143] Giovannini G., Feretti L., Venturi T., Kim K.T., & Kronberg P.P. 1993, *Ap.J.*, 406, 399

[144] Giovannini G., Tordi M., & Feretti L. 1999, *NewA*, 4, 141

[145] Giovannini G., Feretti L., & Govoni F. 2000, in *The Universe at Low Radio Frequencies*, Symp. IAU 199, Pune (India) [astro-ph/0006380]

[146] Giovannini G. & Feretti L. 2002, in *Merging Processes in Clusters of Galaxies*, eds. L. Feretti, I. M. Gioia, G. Giovannini (Dordrecht: Kluwer)

[147] Godon P., Soker N., & White R. E. 1998, *A.J.*, 116, 37

[148] Goldsmith O., & Rephaeli Y. 1993, *Ap.J.,* 411, 518

[149] Gomez P. L., Loken C., Roettiger K., & Burns, J. O. 2002, *Ap.J.,* 569, 122

[150] Govoni F., Enßlin T. A., Feretti L., & Giovannini G. 2001a, *A.&A.,* 369, 441

[151] Govoni F., Feretti L., Giovannini G., Böhringer H., Reiprich T. H., & Murgia M. 2001b, *A.&A.,* 376, 803

[152] Gull S. F., & Northover K. J. E. 1973, *Nature*, 244, 80

[153] Gunn J. E., Hoessel J. G., & Oke J. B. 1986, *Ap.J.,* 306, 30

[154] Hamilton R. J., Petrosian V. 1992, *Ap.J.,* 398, 350

[155] Hanish R. J. 1982, *A.&A.,* 111, 97

[156] Harris D. E., Kapahi V. K., & Ekers R. D. 1980, *Ap.J.Suppl.,* 39, 215

[157] Heckman T. M., Baum S. A., van Breugel W. J. M., & McCarthy P. 1989, *Ap.J.,* 338, 48

[158] Hunstead R. W., et al. 1999, in *Diffuse thermal and relativistic plasma in galaxy clusters*. eds. H. Bohringer, L. Feretti, P. Schuecker, MPE Report 271, 19

[159] Hwang Z. 1997, *Science*, 278, 1917

[160] Irwin J. A., & Sarazin C. L. 1995, *Ap.J.,* 455, 497

[161] Irwin J. A., Stil J. M., & Bridges T. J. 2001, *M.N.R.A.S.,* 328, 359

[162] Jafelice, L. C. 1992, *A.J.*, 104, 1279

[163] Jaffe W.J. 1977, *Ap.J.*, 212, 1

[164] Jaffe W. J. 1980, *Ap.J.*, 241, 925

[165] Jaffe W. J., & Rudnick L. 1979, *Ap.J.* 233, 453

[166] Jaffe W. & Bremer M. N. 1997, *M.N.R.A.S.,* 284, L1

[167] Jansen F., Lumb D., Altieri B., Clavel J., Ehle M., et al. 2001, *A.&A.,* 365, L1

[168] Johnstone R. M., Fabian A. C., Edge A. C., & Thomas P. A. 1992, *M.N.R.A.S.,* 255, 431

[169] Johnstone R. M., Allen S. W., Fabian, A. C., & Sanders, J. S. 2002, *M.N.R.A.S.,* 336, 299

[170] Jones C., & Forman W. 1984, *Ap.J.,* 276, 38

[171] Jones C., & Forman W. 1999, *Ap.J.,* 511, 65

[172] Kaastra J. S., Lieu R., Mittaz J. P. D., Bleeker J. A. M., Mewe R., Colafrancesco S., & Lockman F. J. 1999, *Ap.J*, 519, L119

[173] Kaastra J. S., Ferrigno C., Tamura T., Paerels F. B. S., Peterson J. R., & Mittaz J. P. D. 2001, *A.&A.,* 365, 99

[174] Kang H., Rachen J. P., & Biermann P. L. 1997, *M.N.R.A.S.,* 286, 257

[175] Kardashev N. S. 1962, *Soviet Astronomy – AJ*, 6, 3

[176] Karzas W. J., & Latter R. 1961, *Ap.J.Suppl.*, 6, 167

[177] Kellogg E., Baldwin J. R., & Koch, D. 1975 *Ap.J.,* 199, 299

[178] Kempner J. C., & Sarazin C. L. 2000, *Ap.J.,* 530, 282

[179] Kempner J. C., & Sarazin C. L. 2001, *Ap.J.,* 548, 639

[180] Kim K. T., Kronberg P. P., Dewdney P. E., & Landecker T. L. 1990, *Ap.J.*, 355, 29

[181] Kim K. T., Tribble P. C., & Kronberg P. P. 1991, *Ap.J.*, 379, 80

[182] King I. R. 1962, *A.J.*, 67, 471

[183] King I. R. 1966, *A.J.*, 71, 64

[184] Krall N. A., & Trivelpiece A. N. 1973, *Principles of Plasma Physics*, McGraw-Hill: New York

[185] Kronberg P. P., Lesch H., & Hopp U. 1999, *Ap.J.,* 511, 56

[186] Kulsrud R. M., & Ferrari A. 1971, *Astrophys. Space Sci.* 12, 302

[187] Lacombe C. 1977, *A.&A.,* 54, 1

[188] Liang H., Hunstead R. W., Birkinshaw M., & Andreani P. 2000 *Ap.J.,* 544, 686

[189] Lieu R., Mittaz J. P. D., Bowyer S., Breen J. O., Lockman F. J., Murphy E. M., & Hwang, C.-Y. 1996a, *Science*, 274, 1335

[190] Lieu R., Mittaz J. P. D., Bowyer S., Lockman F. J., Hwang C.-Y., & Schmitt J. H. M. M. 1996b, *Ap.J.*, 458, L5

[191] Lieu R., Bonamente M., & Mittaz J. P. D. 1999, *Ap.J*, 517, L91

[192] Livshitz E. M., & Pitaevskii L. P., 1981, *Physical Kinetics* (Pergamon: Oxford)

[193] Loewenstein M., & Fabian A. C. 1990, *M.N.R.A.S.,* 242, 120

[194] Mannheim K., & Schlickeiser R. 1994, *A.&A.,* 286, 983

[195] Markevitch M., Ponman T. J., Nulsen P. E. J., Bautz M. W., Burke D. J., et al. 2000, *Ap.J.,* 541, 542

[196] Matsushita K., Belsole E., Finoguenov A., & Böhringer H. 2002, *A.&A.,* 386, 77

[197] McKee C. F., & Cowie L. L. 1977, *Ap.J.*, 215, 213

[198] McNamara B. 1997, in *Galactic and Cluster Cooling Flows*; ASP Conference Series; Vol. 115, p. 109, ed. N. Soker

[199] McNamara B., & O'Connell R. W. 1989, *A.J.*, 98, 2018

[200] McNamara B., & O'Connell R. W. 1993, *A.J.*, 105, 417

[201] Melrose D. B. 1968, *Ap. Sp. Sci.*, 2, 171

[202] Melrose D. B. 1980, *Plasma Astrophysics: Nonthermal Processes in Diffuse Magnetized Plasmas*, Gordon and Breach

[203] Mewe R. & Gronenschild E. H. 1981, *A.&A.Suppl.*, 45, 11

[204] Miley G. 1980, *A.R.A.&A.,* 165, 218

[205] Miniati F., Jones T. W., Kang H., & Ryu D. 2001, *Ap.J.,* 562, 233

[206] Mittaz J. P. D., Lieu R., & Lockman F. J. 1998, *Ap.J.,* 498, L17

[207] Molendi S., & Pizzolato F. 2001, *Ap.J.,* 560, 194

[208] Morris R. G., & Fabian A. C., 2003 *M.N.R.A.S.* in press, [astro-ph/0209559]

[209] Narayan R., & Medvedev M. V. 2001, *Ap.J.,* 562, L129

[210] Neumann D. M., & Arnaud M. 1999, *A.&A.,* 348, 711

[211] Neumann D. M., & Arnaud M. 2001, *A.&A.,* 373, L33

[212] Newman W. I., Newman A. L., & Rephaeli Y. 2002, *Ap.J.,* 575, 755

[213] Nulsen P. E. J. 1986, *M.N.R.A.S.,* 221, 377

[214] Nulsen P. E. J. 1988, in *Cooling flows in Clusters and Galaxies*, ed A. C. Fabian, Dordrecht: Kluwer, p. 175

[215] Nulsen P. E. J. 1997, in *Galactic and Cluster Cooling Flows*; ASP Conference Series; Vol. 115, p. 135, ed. N. Soker

[216] O'Dea C. P., Payne H., & Kocevski D. 1998, *Ap.J.,* 116, 623

[217] Oegerle W. R., Cowie L., Davidsen A., Hu E., Hutchings J., Murphy E., Sembach K., & Woodgate B. 2001, *Ap.J.,* 560, 187

[218] Okoye S. E., & Onuora L. I. 1996, *M.N.R.A.S.,* 283, 1047

[219] Olinto A. V. 1997, in 3rd RESCEU International Symp. on *Particle Cosmology*, Tokyo [astro-ph/9807051]

[220] Owen F. N., Eilek J. A., & Keel W. C. 1990, *Ap.J.,* 362, 449

[221] Owen F., Morrison G., & Voges W. 1999 in *Diffuse Thermal and Relativistic Plasma in Galaxy Clusters*, eds. Böringer H., Feretti L., Schuecker P.; MPE Report 271, p.9

[222] Pacholczyk A. G. 1970, *Radio Astrophysics*, Freeman & Co. San Francisco

[223] Peacock J. A. 1981, *M.N.R.A.S.,* 196, 135

[224] Pedlar A., Ghataure H. S., Davies R. D., Harrison B. A., Perley R., Crane P. C., & Unger S. W. 1990, *M.N.R.A.S.,* 246, 477

[225] Peres C. B., Fabian A. C., Edge A. C., Allen S. W., Johnstone R. M., & White D. A. 1998, *M.N.R.A.S.,* 298, 416

[226] Perley R. A., & Taylor G. B. 1991, *A.J.*, 101, 1623

[227] Peterson J. R., Paerels F. B. S., Kaastra J. S., Arnaud M., Reiprich T. H., Fabian A. C., Mushotzky R. F., Jernigan J. G. & Sakelliou I. 2001, *A.&A.,* 365, 104

[228] Peterson J. R., Ferrigno C., Kaastra J. S., Paerels F. B. S., Kahn S. M., Jernigan J. G., Bleeker J. A. M., & Tamura T. 2002a, Proc. Symposium *New Visions of the X-ray Universe in the XMM-Newton and Chandra Era*, 26-30 November 2001, ESTEC, The Netherlands, [astro-ph/0202108]

[229] Peterson J. R., Kahn S. M., Paerels F. B. S., Kaastra J. S., Tamura T., Bleeker J. A. M., Ferrigno C., & Jernigan J. G. 2002b, [astro-ph/0210662]

[230] Petrosian, V. 2001, *Ap.J.,* 557, 560

[231] Pistinner S., & Shaviv G. 1996, *Ap.J.,* 459, 147

[232] Raymond J. C., & Smith B. W. 1977, *Ap.J.Suppl.*, 35, 419

[233] Rengelink R. B., Tang Y., de Bruyn A. G., Miley G. K., Bremer M. N., Roettgering H. J. A., & Bremer, M. A. R. 1997, *A.&A. Suppl.*, 124, 259

[234] Rephaeli Y. 1979, *Ap.J.,* 227, 364

[235] Rephaeli Y., Gruber D., & Blanco P. 1999, *Ap.J.,* 511, L21

[236] Rephaeli Y., & Gruber D. 2002, *Ap.J.,* 579, 587

[237] Rizza E., Loken C., Bliton M., Roettiger K., & Burns J.O. 2000, *A.J.*, 119, 21

[238] Roettiger K., Stone J. M., & Burns J. O. 1999, *Ap.J.,* 518, 594

[239] Roettiger K., Burns J. O., & Stone J. M. 1999, *Ap.J.,* 518, 603

[240] Roland J. 1981, *A.&A.,* 93, 407

[241] Roland J., Hanish R. J., Véron P., & Fomalont E. 1985, *A.&A.,* 148, 323

[242] Rosner R., & Tucker W. H. 1989, *Ap.J.,* 338, 761

[243] Rudnick L., & Blundell K. 2003, *Ap.J.* in press, [astro-ph/0301260]

[244] Ruzmaikin A., Sokolov D, & Shukurov A. 1989, *M.N.R.A.S.,* 241, 1

[245] Ruszkowski, M. & Begelman, M. C. 2002, *Ap.J.,* 581, 223

[246] Rybicki G. B., & Lightman A. P. 1979, *Radiative Processes in Astrophysics*, Wiley-Interscience Pub.

[247] Rosner R. & Tucker W. 1989, *Ap.J.,* 338, 761

[248] Sakelliou I., Peterson J. R., Tamura T., Paerels F. B. S., Kaastra J. S., et al. 2002, *A.&A.,* 391, 903

[249] Sánchez-Salcedo F. J., Brandenburg A., & Shukurov A. 1998, *Ap&SS*, 263, 87

[250] Sarazin C. L. 1986, *Rev. Mod. Phys.*, 58, 1

[251] Sarazin C. L. 1988, *X–ray Emission from Clusters of Galaxies*, Cambridge Univ. Press

[252] Sarazin C. L. 1997, in *Galactic and cluster cooling flows*, ed. N. Soker, ASP Conf. Series vol. 115, pag. 172

[253] Sarazin C. L. 1999, *Ap.J.,* 520, 529

[254] Sarazin C. L. 2002, in *Merging Processes in Clusters of Galaxies*, eds. L. Feretti, I. M. Gioia, G. Giovannini (Dordrecht: Kluwer)

[255] Sarazin C. L., & Bachall J. N. 1977, *Ap.J.Suppl.,* 34, 451

[256] Sarazin C. L., Baum S. A., & O'Dea C. P. 1995, *Ap.J.,* 451, 125

[257] Sarazin C. L., & Lieu R. 1998, *Ap.J.,* 494, L177

[258] Sarazin C. L., & Kempner J. C. 2000, *Ap.J.,* 533, 73

[259] Sasaki S., & Yamasaki Y. 2002, *PASJ*, 54, 1

[260] Schlickeiser R., Sievers A., & Thiemann H. 1987, *A.&A.,* 182, 21

[261] Schmidt R. W., Allen S. W., & Fabian A. C. 2001, *M.N.R.A.S.,* 327, 1057

[262] Schwarz R. A., Edge A. C., Voges W., Böhringer H., Ebeling H., & Briel U. G. 1992, *A.&A.,* 256, L11

[263] Sijbring D. 1993, *A Radio Continuum and HI Line Study of the Perseus Cluster*, PhD Thesis, Groningen

[264] Slee O. B., Roy A. L., Murgia M., Andernach H., & Ehle M. 2001, *A.J.*, 122, 1172

[265] Soker N., & Sarazin C.L. 1990, *Ap.J.*, 348, 73

[266] Spitzer, L. Jr. 1956 *Physics of Fully Ionized Gases.* New York: Interscience

[267] Spitzer L. Jr. 1978, *Physical Processes in the Interstellar Medium*, New York: Wiley

[268] Stewart G. C., Fabian A. C., Jones C., & Forman W. 1984, *Ap.J.,* 285, 1

[269] Strüder L., Briel U., Dennerl K., Hartmann R., Kendziorra E., et al. 2001, *A.&A.,* 365, L18

[270] Swann W. F. G. 1933, *Phys. Rev.* 43, 217

[271] Tabor G. & Binney J. 1993, *M.N.R.A.S.,* 263, 123

[272] Takizawa M., & Naito T. 2000, *Ap.J.,* 535, 586

[273] Tamura T., Kaastra J. S., Peterson J. R., Paerels F. B. S., Mittaz, J. P. D., et al. 2001a, *A.&A.,* 365, L87

[274] Tamura T., Bleeker J. A. M., Kaastra J. S., Ferrigno C., & Molendi S. 2001b, *A.&A.,* 379, 101

[275] Taylor G. B., & Perley R. A. 1993, *Ap.J.,* 416, 554

[276] Taylor G. B., Barton E. J., & Ge J. 1994, *AJ* 107, 1942

[277] Thomas P. A., Fabian A. C., & Nulsen P. E. J. 1987, *M.N.R.A.S.,* 228, 973

[278] Tribble P. C. 1989, *M.N.R.A.S.,* 238, 1247

[279] Tribble P. C. 1991, *M.N.R.A.S.,* 248, 741

[280] Tribble P. C. 1993, *M.N.R.A.S.,* 263, 31

[281] Tsytovich V. N. 1972, *An introduction to the Theory of Plasma Turbulence* (Pergamon Press)

[282] Tsytovich V. N. 1977, *Theory of Turbulent Plasma*, Consultants Bureau, New York

[283] Tucker W. H., & Rosner R. 1983, *Ap.J.,* 267, 547

[284] Turner M. J. L., Abbey A., Arnaud M., Balasini M., Barbera M., et al. 2001, *A.&A.,* 365, L27

[285] Vikhlinin A., Markevitch M., & Murray S. S. 2001, *Ap.J.,* 551, 160

[286] Voigt L. M., Schmidt R. W., Fabian A. C., Allen S. W. & Johnstone R. M. 2002, *M.N.R.A.S.,* 355, 7

[287] Völk H. J., & Atoyan A. M. 1999, *Astrop. Phys.*, 11, 73

[288] Webb G. M., Axford W. I., & Terasawa, T. 1983, *Ap.J.,* 270, 537

[289] Wentzel D. G. 1964, *Ap.J.,* 140, 1013

[290] White D. A., Fabian A. C., Johnstone R. M., Mushotzky R. F., & Arnaud K. A. 1991, *M.N.R.A.S.,* 252, 72

[291] White D. A., Jones C., & Forman W. 1997, *M.N.R.A.S.,* 292, 419

[292] Willson M. A. G. 1970, *M.N.R.A.S.*, 151, 1

[293] Wilman R. J., Edge A. C., Johnstone R. M., Crawford C. S., & Fabian A. C. 2000, *M.N.R.A.S.,* 318, 1232

[294] Xu H., Kahn S. M., Peterson J. R., Behar E., Paerels F. B. S., Mushotzky R. F., Jernigan J. G., Brinkman A. C., & Makishima, K. 2002, *Ap.J.,* 579, 600

[295] Zakamska N., & Narayan R. 2003, *Ap.J.,* 582, 162

[296] Zwicky F. 1933, *Helv. Phys. Acta*, 6, 110

[297] Zwicky F. 1957, *Morphological Astronomy*, Berlin, Springer p. 139

[298] Zwicky F., Herzog E., Wild P., Karpowicz M., & Korwal C. 1961-1968, Catalog of Galaxies and Clusters of Galaxies, Vol. 1-6 (Pasadena: Caltech)

Related Publications

Papers in refereed journals:

1. **Gitti M.**, Brunetti G., & Setti G. 2002, "*Modeling the interaction between ICM and relativistic plasma in cooling flows: the case of the Perseus Cluster*", *A.&A.,* 386, 456

2. **Gitti M.**, Brunetti G., Feretti L., & Setti G. 2003 "*On the physical connection between cooling flows and radio mini-halos in clusters of galaxies*", submitted to *A.&A.*

Proceedings:

1. **Gitti M.**, Brunetti G., & Setti G. 2001, "*Interaction between ICM and relativistic plasma in cooling flows*", in "XIIImes Rencontres de Blois: Frontiers of the Universe", in press

2. **Gitti M.**, Brunetti G., & Setti G. 2001, "*Reacceleration of relativistic electrons in cooling flows: the case of Perseus Cluster*", in "Tracing Cosmic Evolution with Galaxy Clusters", eds. S. Borgani, M. Mezzetti & R. Valdarini, ASP Conf. Series. 268, p. 373

3. **Gitti M.**, Brunetti G., Setti G., & Feretti L. 2002 "*Modeling radio mini–halos in cooling flow clusters*", in "Matter and Energy in Clusters of Galaxies", eds. S. Bowyer & C.-Y. Hwang, ASP Conf. Series, in press [astro–ph/0207145]

Acknowledgments

It is really a plasure to thank Prof. Giancarlo Setti, my supervisor, for the great experience and opportunity of working with him.

I am indebted to Dr. Gianfranco Brunetti, my co–supervisor, for his constant assistance during my PhD and his patience in answering all my questions: his help has been very important for my work.

I would like to thank Dr. Luigina Feretti for many useful comments, suggestions and discussions, and for the help with radio data analysis.

All my PhD thesis (and also my Degree thesis) was carried out at the Institute of Radioastronomy: I really want to thank all the staff and the Institute for their hospitality. I am grateful to many people in the Institute who often helped me: Prof. Gabriele Giovannini (for supporting my research, also financially..!), Dr. Marco Bondi, Dr. Federica Govoni, and in particular the system managers who saved me so many times!

I would like to thank all the people who supported me and standed my stress (especially in the last period!). At first the other PhD students: in particular Enrico Piconcelli, my lunch–mate in these three years, Carlo Nipoti, always relaxed even in this stressful situation, and Giuseppe Pupillo, continuously worried for everything. Then all my friends, with a special thought to Serena and Miriam.

I want to thank my family (including also my cousins and my uncle and aunt ... too many to be all mentioned!) for always believing in me and supporting me, even when I've decided to leave Bologna for a post–doc of three years abroad...

Last but not least, I want to particularly thank Simone Dall'Osso: thank you for all the stimulating discussions which helped me in getting more insights into my work, thank you for careful reading the whole thesis, thank you for always encouraging me and convincing to never give up, thank you for your constant support and patient understanding... in a word... thank you for everything! I could never have come through my PhD without you, you know!!

E quindi uscimmo a riveder le stelle.

[Dante, Inferno XXXIV]